Lab on a Chip

CRITICAL REVIEW

View Article Online
View Journal

Cite this: DOI: 10.1039/d5lc00428d

Lab-on-a-chip insights: advancing subsurface flow applications in carbon management and hydrogen storage

Junyi Yang,† Nikoo Moradpour,† Lap Au-Yeung and Peichun Amy Tsai *

The transition to sustainable energy is crucial for mitigating climate change impacts, with hydrogen and carbon storage and utilization technologies playing pivotal roles. This review highlights the integral and useful role of microfluidic technologies in advancing subsurface fluid dynamics for carbon capture, utilization, and storage (CCUS), enhanced oil recovery (EOR), and underground hydrogen storage (UHS). In particular, microfluidic platforms provide clear and insightful visualization of fluid–fluid and fluid–solid interactions at the pore scale, crucial for understanding and further optimizing processes for CO_2 sequestration, hydrogen storage, and oil displacement in various geological formations. We first discuss the development of lab-on-a-chip devices that accurately mimic subsurface conditions, allowing detailed studies of complex phenomena including viscous fingering, capillary trapping, phase behavior during CCUS and EOR processes, and the hysteresis effects unique to hydrogen storage cycles. We also discuss the dynamics of CO_2 gas and foam in enhancing oil recovery and the innovative use of hydrogen foam to mitigate issues associated with pure hydrogen gas storage. The integration of advanced imaging, spectroscopic techniques, and machine learning (ML) with microfluidic experiments has enriched our understanding and opened new pathways for predictive capabilities and operational optimization in CCUS, EOR, and UHS applications. We further emphasize the critical need for continued research into microfluidic applications, *e.g.*, incorporating state-of-the-art ML to optimize microfluidic experiments and parameters, and UHS enhancement through favorable microbial activities and suppression of reactions in H_2 foam, aiming at refining storage strategies and exploiting the full potential of these technologies towards a sustainable energy future.

Received 2nd May 2025,
Accepted 23rd October 2025

DOI: 10.1039/d5lc00428d

rsc.li/loc

1 Introduction

As global warming accelerates, with temperatures reaching 1.36 °C above the late 19th-century levels in 2023,[1] the urgency to mitigate greenhouse gas emissions intensifies. Strategies to combat this issue include improving fossil fuel extraction through enhanced oil recovery (EOR), implementing carbon capture, utilization, and storage (CCUS) technologies, and expanding renewable energy sources such as solar, wind, hydropower, geothermal, and biomass.[2] Subsurface porous media play a vital role in carbon management and energy storage. Geological formations, such as deep saline aquifers and depleted petroleum reservoirs, serve as primary reservoirs for carbon capture and storage (CCS), offering substantial CO_2 storage capacity and potential for EOR applications.[3,4] For example, the Weyburn–Midale Carbon Dioxide Project in Saskatchewan, Canada, one of the world's largest CO_2-EOR projects, has achieved over 20 Mt of CO_2 injection to date.[5] Similarly, underground porous structures, including depleted oil and gas reservoirs, saline aquifers, and salt caverns, have emerged as vital sites for large-scale hydrogen storage.[6] Underground hydrogen storage (UHS) facilitates the injection, withdrawal, and reuse of hydrogen to balance the intermittency of renewable energy.[6] Together, these subsurface technologies are crucial for reducing greenhouse gas emissions and supporting the transition to a sustainable energy future.

The macro-scale processes of oil recovery, CO_2, and H_2 storage are fundamentally governed by fluid interactions and dynamics within porous rocks, fractures, shale formations, and other subsurface geological structures.[7,8] Traditional studies of subsurface porous media flow have commonly employed core flooding techniques, involving cylindrical sandstone and carbonate core samples as the test medium.[7] These samples are made of optically opaque materials, which poses limitations and makes direct visualization challenging.[7] Although advanced micro-computed tomography (micro-CT) and nuclear magnetic resonance

Department of Mechanical Engineering, University of Alberta, Edmonton, Alberta T6G 2R3, Canada. E-mail: peichun.amy.tsai@ualberta.ca
† Equally-contributing first authors.

(NMR)[7] offer valuable insights into fluid flow within three-dimensional (3D) pore structures, their high costs and complex setups restrict routine laboratory analysis.[7] Microfluidics, in contrast, has emerged as a versatile platform for studying multiphase flow processes in subsurface applications.[7–12] Microfluidic lab-on-a-chip systems, with fluid channels ranging from 100 nm–100 μm,[13,14] enable precise fluid manipulation, rapid testing, and clear optical access, making them powerful for investigating flow and transport phenomena in subsurface systems.[7]

This review highlights the critical role of microfluidic visualization in optimizing parameters and advancing the understanding of flow and transport mechanisms in subsurface porous media. Early microfluidic studies in the energy sector primarily focused on visualizing fluid–fluid displacement.[12,15–18] However, recent advancements in lab-on-a-chip technology have expanded their capabilities significantly. Developments in high-pressure and high-temperature platforms,[19,20] complex surface modifications,[21–24] and nano-scale pore structures[10,25] have allowed researchers to replicate realistic reservoir conditions. These advancements have enhanced our understanding of fluid–fluid interactions under reservoir pressure and temperature conditions, as well as fluid–solid interactions influenced by engineered surface properties.[12] The forthcoming section 2 reviews microfabrication techniques focusing on soft lithography and high-pressure microfabrication, as well as applications of machine learning coupled with microfluidic systems.

The microfluidics community has contributed comprehensive literature reviews on topics including enhanced oil recovery (EOR) applications,[7,11] CO_2 sequestration in saline aquifers,[26] fluid analysis,[12] phase behavior characterization,[10] liquid foam studies,[27] sustainable technologies,[2] and chemical reactions,[28,29] among others. Building on this foundation, this review concentrates specifically on the application of microfluidics in CO_2-EOR (section 3), CCS in saline aquifers (section 4), and hydrogen storage (section 5). We explore in depth CO_2-EOR processes, including immiscible and miscible displacement, huff-and-puff cycles, and foam-assisted CO_2-EOR, as well as key mechanisms involved in CCS and hydrogen storage in subsurface porous media. We critically assess how microfluidics, combined with advanced optical and spectroscopic techniques, has improved the understanding of fluid properties, flow dynamics, and pore-scale interactions. Through this review, we aim to highlight the significant role of microfluidics in resolving challenges in subsurface flow research and inspire future innovations.

2 Microfluidics overview

The advent of microfabrication has enabled precise fluid manipulation and transport at the microscale ($O(10^{-2}$ μL)),[30] making advancements across various applications, including biomedical sciences,[31] food and agriculture,[32] analytical devices (lab-on-a-chip),[33] and fluid flow in porous media,[8] such as EOR.[34] Microfluidic devices offer several advantages, including reduced material consumption, accelerated processing times (*e.g.*, reaction, detection, displacement), lower costs, and real-time visualization of phenomena occurring in opaque or inaccessible media.[30,35] The pore-scale phenomena in subsurface porous formations can be mimicked on microfluidic chips using various microfabrication methods and materials.[8,36,37] In the following, we discuss the most commonly used fabrication techniques in two main subcategories: soft lithography and high-pressure microfluidics. We then introduce different types of porous media designs used in microfluidic chips, followed by a comparison and discussion of pore-scale visualization methods in conventional core flooding *versus* microfluidics. Finally, in section 2.5, we briefly discuss recent utilization of machine learning approaches in the field of microfluidics.

2.1 Microfabrication technique: soft lithography

The development of micro electro mechanical systems (MEMS) and associated microfabrication techniques, namely lithography and etching, led to the exploration of fluid dynamics at microscales, on the order of magnitude of $O(10^{-6}–10^{-3})$ m, establishing the field of microfluidics.[37,47,48] A pivotal moment was the invention of micro-droplets in 1964, revolutionizing the ink-jet printer industry. The first microfluidic lab-on-chip device for miniaturized gas chromatography (Fig. 1A) was created in 1979.[47,49,50] Initially, hard materials like silicon, glass, and polymethyl methacrylate (PMMA) dominated MEMS device fabrication. However, the demand for cost-effective, high-throughput alternatives led to the development of soft lithography using PDMS (polydimethylsiloxane) microchips by Whitesides in 1998.[50–53]

To date, multiple variants of soft lithography have been introduced, including hot embossing,[54] micro-molding in capillaries (Fig. 1B), micro-contact printing (Fig. 1C), micro-transfer molding, solvent assisted micro-molding, and replica molding (Fig. 1D),[55–58] with the latter being widely used to fabricate microfluidic devices. Replica molding includes two principal steps: 1) fabrication of the hard master mold by well-established techniques of photolithography and etching. In photolithography, the target structures are patterned on a hard substrate, such as silicon, using photomasks[59,60] or newer maskless techniques[61] such as digital micromirror device (DMD),[62] direct writing,[63] and 3D printing.[64] 2) Fabrication of the primary chips by replicating these master patterns on soft materials, primarily polymers, like PDMS, which have a silicon–oxygen backbone. Commercial PDMS kits, containing a linear pre-polymer (elastomer) with siloxane oligomers and vinyl terminated groups and a cross-linker with the same oligomers and silicon hydride groups,[65,66] facilitate curing at moderately low temperatures to solidify the liquid PDMS into flexible solid stamps.[48,53,67] Before PDMS casting, the surface of the master mold is typically hydrophobized with silane-based chemicals to ensure smooth demolding of cured PDMS.[68,69]

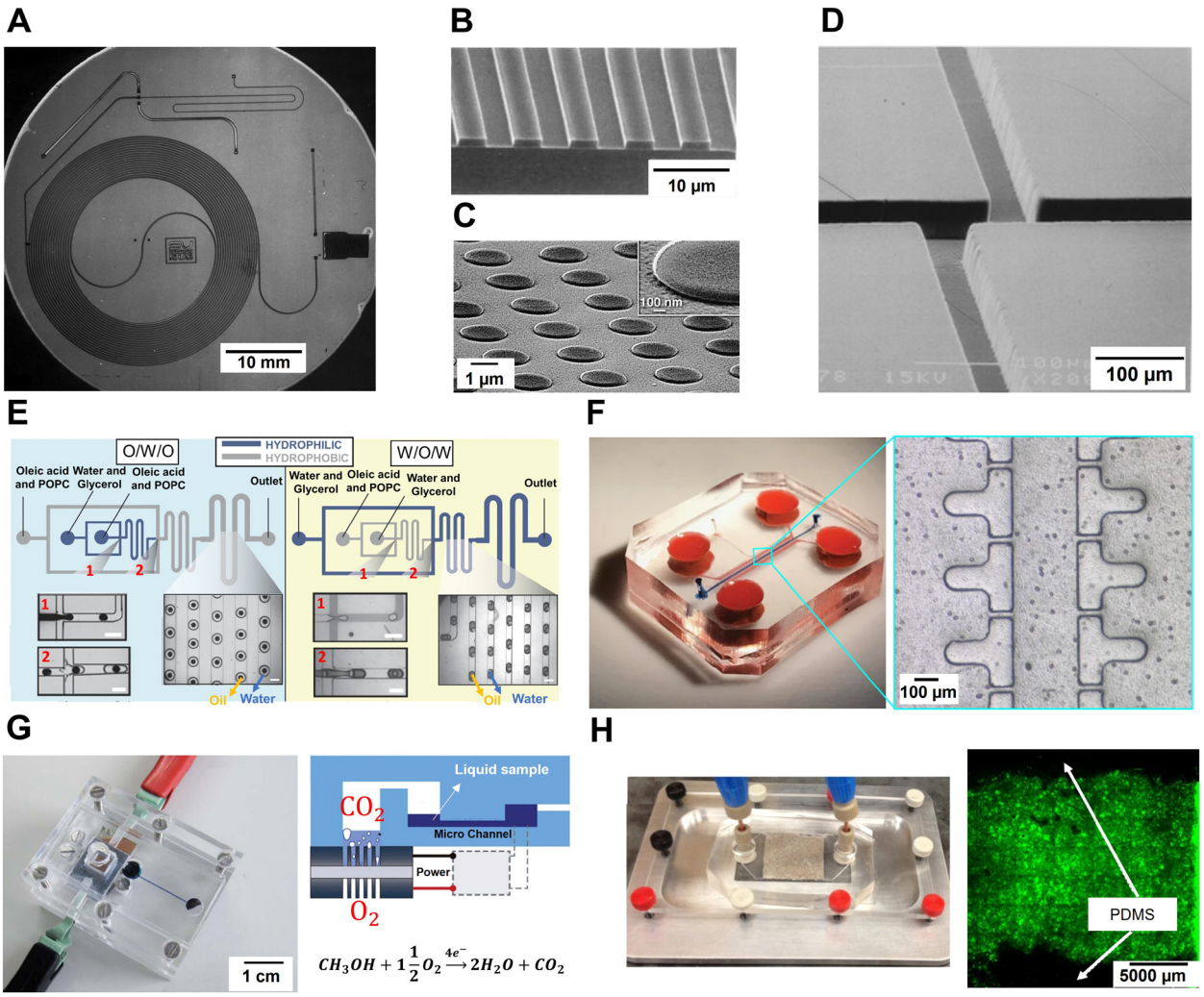

Fig. 1 Microfabricated chips for fluidic applications: (A) the first miniaturized gas chromatographer fabricated on silicon wafer fabricated by Terry *et al.*,[38] 1979 (adapted with permission from de Mello.[39] Copyright © 2002 the Royal Society of Chemistry). (B) Rectangular pattern of PDMS slabs fabricated by micro-molding in capillaries on a gold film (adapted with permission from Kim *et al.*[40] Copyright © 1995 Nature Publishing Group). (C) SEM image of circular patterns on silicon wafer fabricated by microcontact printing (adapted with permission from Marzolin *et al.*[41] Copyright © 1998 Elsevier). (D) SEM image of a double T-section pattern on PDMS fabricated by replica molding (adapted with permission from Duffy *et al.*[42] Copyright © 1998 American Chemical Society). (E) Surface modification (plasma treatment and polyvinyl alcohol (PVA) deposition) of PDMS microfluidic channels to apply varied wettability to generate oil in water in oil (O/W/O) and water in oil in water (W/O/W) double emulsions. All scale bars are 300 μm (adapted from Trantidou *et al.*[43] under CC-BY License). (F) PDMS cartilage-on-a-chip with T-shaped pillars fabricated to predict the efficacy of disease-modifying osteoarthritis (DMOA) drugs (adapted with permission from Occhetta *et al.*[44] Copyright © 2019 Nature Publishing Group). (G) PDMS micro direct methanol fuel cell (μDMFC)-micropump where methanol oxidation produces CO_2 to pressurize the liquid sample toward the analysis (adapted with permission from Esquivel *et al.*[45] Copyright © 2012 the Royal Society of Chemistry). (H) Real rock-microfluidic flow cell (RR-MFC) configuration where a thin section (500 μm thickness) of the sandstone sample is assembled with a PDMS channel to involve geochemical reactions in visualizing fluid flow in subsurface porous rocks. On the right, displacement of fluorescein-carrying fluid with dye-free fluid in the RR-MFC chip (adapted with permission from Singh *et al.*[46] Copyright © 2017 Elsevier).

Although other polymers, such as polyimide (PI), polycarbonate (PC), and polystyrene (PS), are available,[48,55] PDMS remains preferred for several advantages. 1) It allows precise and straightforward replication of micro-sized structures.[50,70,71] 2) Its optical transparency and non-toxicity facilitate real-time visualization of fluidic phenomena. 3) PDMS can form strong, permanent (van der Waals) bonds with various substrates, particularly itself and glass, creating a sealed fluid-flow environment in microfluidic devices.[72] 4) The prototyping process is fast and affordable, often outside cleanroom facilities, which is a significant advantage for research applications.[51] 5) It is suitable for low-pressure conditions with a Young's modulus of ≈0.1–1.2 MPa.[47,73] 6) The surface properties of PDMS can be modified to adjust wettability (Fig. 1E).[74,75] PDMS's diverse applications span drug delivery (Fig. 1F), medical diagnosis, biosensors,[76,77] environmental contamination detection and analysis,[78] fuel cells (Fig. 1G),[79] oil and gas production (Fig. 1H),[34,59,80,81] and carbon capture, sequestration, and utilization.[82–84]

2.2 Microfabrication technique: high-pressure microfluidics

Accurately simulating reservoir conditions in the laboratory requires microfluidic chips that can operate under high-pressure and high-temperature conditions to realistically capture fluid interactions. Subsurface energy-related applications require materials that can withstand the high pressures (P) and temperatures (T) of geological formations ($P \approx$ O(10) MPa and $T \approx$ 30–100 °C (ref. 88 and 89)). Recent research has therefore focused on developing lab-on-chips capable of operating at elevated pressures and temperatures,[19,84,90–100] effectively simulating subsurface processes under reservoir conditions.

Silicon–glass and glass–glass are the most commonly used materials for high-pressure microfluidic applications,[8] with their microfabrication techniques summarized in Fig. 2A and B. Fabrication of silicon or glass microfluidic devices typically requires a cleanroom facility to minimize contamination and ensure precision. More recently, thermoplastic polymers[101–103] and rigid epoxies[87,95] have also been developed for high-pressure applications, with their fabrication methods shown in Fig. 2C and D. While these materials tolerate relatively lower pressures compared to silicon and glass, they offer advantages such as reduced costs and scalability, since most fabrication processes do not require a cleanroom environment. The following sections discuss these high-pressure microfluidic fabrication techniques in detail.

Silicon was the first material used for microfluidic chips, inspired by MEMS technologies.[14,38] The fabrication process (Fig. 2A) starts in a cleanroom with the application of a photoresist layer to a clean silicon wafer, followed by photolithography. In more detail, a clean silicon wafer is first primed with bis(trimethylsilyl)amine (HMDS) vapor to improve photoresist adhesion. A photoresist layer is then applied, and targeted (micrometer-sized) channels are patterned using UV light with a photomask or direct laser

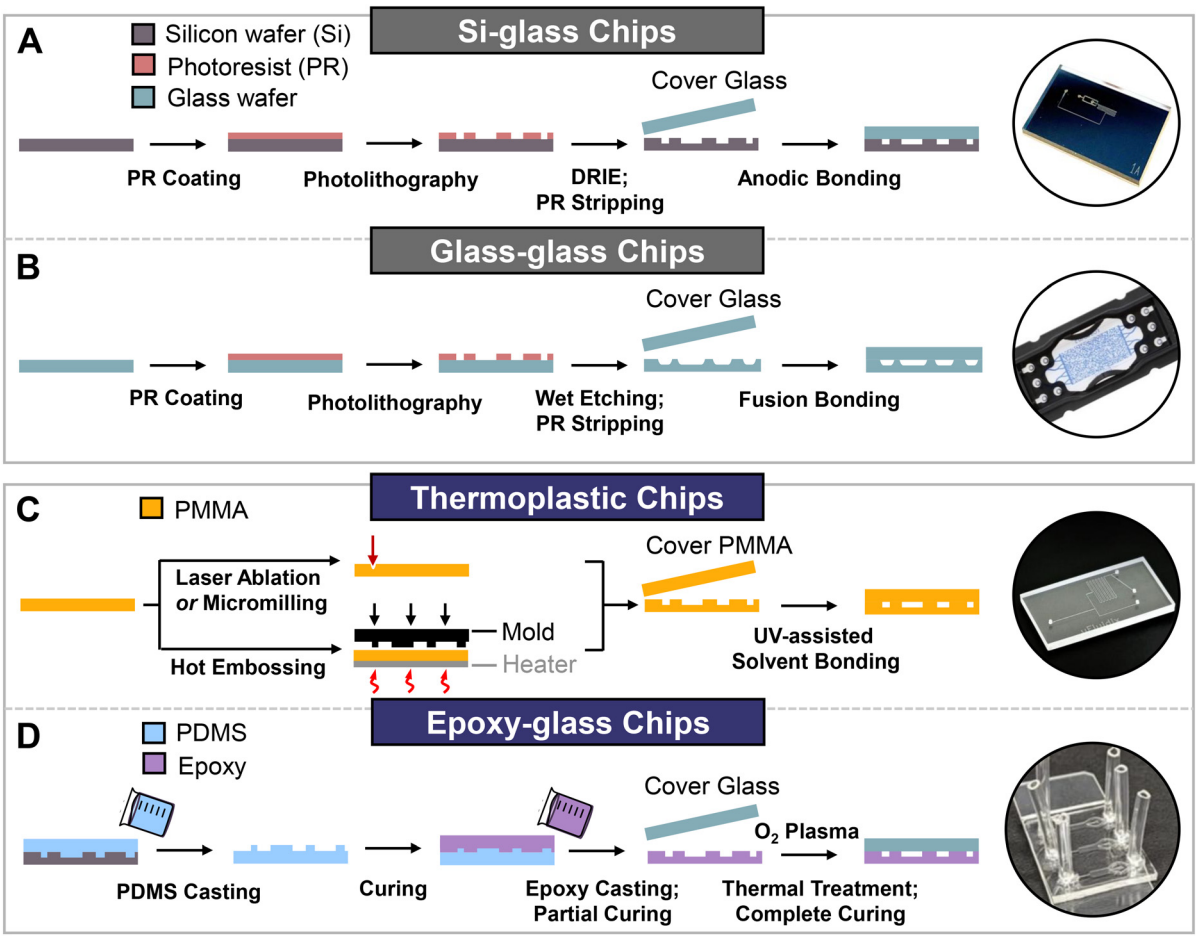

Fig. 2 Summary of microfabrication methods for high-pressure microfluidic applications: (A) silicon–glass chips are fabricated through a standard process involving photolithography, deep reactive ion etching (DRIE), and anodic bonding. The images on the right show their representative chips. (B) Glass–glass microfluidic chips are typically produced using photolithography, wet etching, and fusion bonding (adapted with permission from Micronit.[85] Copyright © 2020-present Micronit B.V.). (C) Thermoplastic chips, such as polymethyl methacrylate (PMMA) chips, can be fabricated *via* laser ablation, micromilling, or hot embossing, followed by solvent bonding (adapted with permission from uFluidix.[86] Copyright © 2022 uFluidix). (D) Epoxy–glass chips are a recently developed approach for high-pressure microfluidics. This process involves casting epoxy on a PDMS mold, partially cured, followed by bonding to a cover glass after further curing (adapted from Rein *et al.*[87] under CC-BY License).

writing. After exposure, unprotected substrate areas are removed through etching. Silicon microfabrication commonly utilizes deep reactive ion etching (DRIE),[104] which can produce deep features with a high aspect ratio. Silicon and glass are then sealed through anodic bonding,[105–107] employing high voltage and elevated temperatures (typically 100–1500 V and 300–500 °C (ref. 107)) to generate an electrostatic field for a permanent bond. Once bonded, the wafers can be diced into individual microfluidic chips if needed.

Glass–glass microfluidics has become another widely used alternative for high-pressure applications. The fabrication process, illustrated in Fig. 2B, involves etching (borosilicate or soda-lime) glass using hydrofluoric acid under controlled etch rates.[108] Although wet etching is more cost-effective than plasma etching, it offers lower selectivity and hydrofluoric acid poses significant safety risks, requiring strict handling protocols. Laser engraving is another method used for fabricating glass microfluidic devices, but its resolution is approximately an order of magnitude lower than that of photolithography.[8] Glass substrates are joined using fusion bonding, where surfaces are plasma-treated and annealed at temperatures up to 1000 °C, higher than those used for anodic bonding.[109] This method creates a strong and permanent bond suitable for high-pressure applications.

Beyond glass and silicon, other materials and fabrication techniques have been explored for high-pressure microfluidics. One example is the transparent thermoplastic polymer, such as PMMA.[102] Common ways for fabricating PMMA microfluidics, illustrated in Fig. 2C, include hot embossing,[110] laser engraving,[83,101] and micromilling.[93,103] These techniques offer the advantages of low cost and scalability, enabling the potential mass production of PMMA chips.[101,102] Although PMMA microfluidics has a lower pressure tolerance than glass or silicon, it can still withstand pressures as high as 11.75 MPa, when the bonding is assisted by acetic acid solvent, UV treatment, and clamping force.[103]

Rigid epoxies have recently offered an affordable alternative to traditional materials such as glass and silicon. Soft lithography techniques have been adapted to fabricate high-pressure microfluidic devices using rigid epoxies, as shown in Fig. 2D. For instance, Martin *et al.*[95] introduced a UV-curable off-stoichiometry thiol-enes (OSTE) epoxy cast in a PDMS mold.[95] The resulting microfluidic device, supported by an internal glass structure, demonstrated exceptional pressure resistance of up to 20 MPa.[95] Similarly, Rein *et al.*[87] fabricated microfluidic devices using rigid epoxy (EpoxAcast™ 690) bonded with glass, also cast in a PDMS mold, achieving a pressure tolerance of around 5 MPa.[87] Once a PDMS mold is prepared, this fabrication process becomes more accessible, requiring no cleanroom facilities or specialized equipment. These advances highlight the ongoing evolution of high-pressure microfluidic technology, which is essential for simulating complex subsurface processes. Further research is encouraged to develop faster and more cost-effective fabrication routes (beyond standard lithography techniques) for rapid prototyping in high-pressure microfluidic applications.

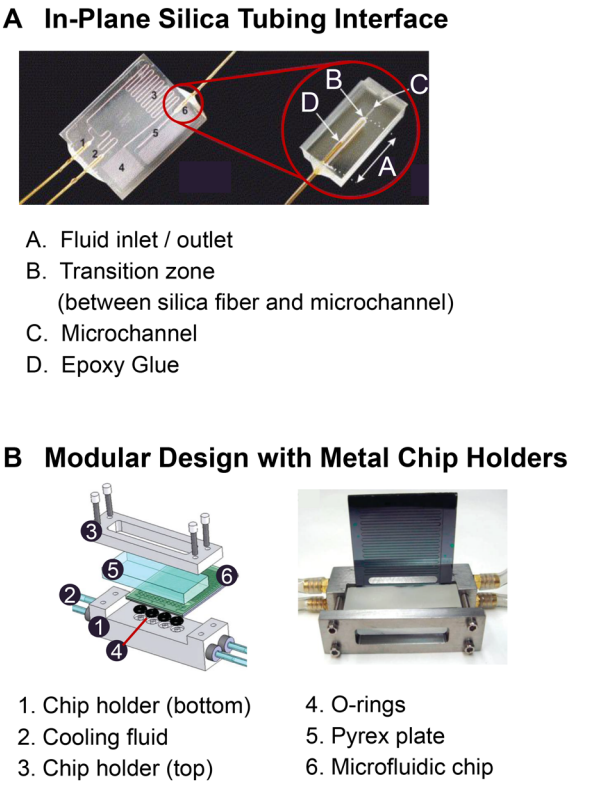

Fig. 3 Two representative packaging techniques for high-pressure microfluidic applications: (A) in-plane connection method: microfluidic chips interfaced with external silica tubing using an in-plane connection. The junction between the silica fiber and the microchannel is secured with epoxy glue to ensure robust sealing (adapted with permission from Tiggelaar *et al.*[92] Copyright © 2007 Elsevier). (B) Modular chip design: the microfluidic chip is encased between metal holders and sealed with O-rings to prevent leaks. The lower chip holder contains internal fluid channels that connect to external stainless steel adaptors and tubing, facilitating fluid flow (adapted with permission from Marre *et al.*[19] Copyright © 2010 American Chemical Society).

In addition to material selection and microfabrication, proper interconnection and packaging techniques are crucial for ensuring reliable sealing of the microfluidic systems under elevated pressures.[19,20] Fig. 3 illustrates two widely used packaging methods for high-pressure microfluidics, highlighting their differences in design and functionality. One approach is to have the entire microfluidic platform as a single integrated piece (see Fig. 3A), featuring in-plane inlet and outlet ports that simplify fluidic connections.[91,92] In this configuration, silica fibers are interfaced directly with the microchannels and secured to the side of the chip using epoxy, creating a connection capable of withstanding pressures up to 30 MPa.[92] However, while this in-plane method requires fewer components, it offers limited flexibility because the chip cannot be easily detached or modified once assembled. By contrast, the second approach, depicted in Fig. 3B, employs

a modular design that offers greater flexibility for assembly, reuse, and adaptation.[19] In this method, the microfluidic chip is housed within a stainless steel or aluminum chip holder, providing added structural support and protection.[19] O-rings and a compression block ensure a secure seal around the internal fluid channels. This modular configuration is well suited for applications requiring frequent modifications or iterations, as it allows easier assembly and disassembly.

2.3 Pore network designs on microfluidic chips

The geometrical pattern of microfluidic porous media is a critical factor in visualizing fluid flow, ranging from simple regular arrangements to complex irregular structures. These designs are generally classified into two main categories: homogeneous and heterogeneous geometries.

2.3.1 Homogeneous pore structure. Microfluidic porous media initially featured simple designs where all pillars (obstacles) followed identical shapes, such as circular, square, or rectangular geometries (Fig. 4A).[111–114] In these configurations, both the pore spacing (pillar separation) and the etched chip depth are uniform across the entire porous region. Homogeneous designs remain widely used when the study focuses on experimental parameters other than geometry—such as fluid injection conditions or fluid type—because they simplify interpretation of interfacial dynamics and subsequent analytical or numerical modeling (Fig. 4B and C).[115–117] While straightforward and highly informative, homogeneous designs do not capture the heterogeneity of real rock formations, which strongly influences pressure, saturation, and velocity distributions.[80,118–120]

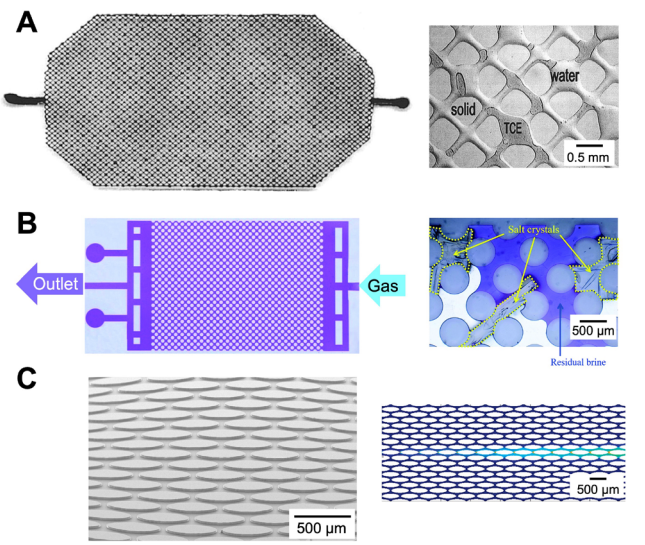

Fig. 4 Homogeneous microfluidic pore networks. (A) Displacement of trichloroethylene (TCE) by surfactant foam in a glass chip with diamond-shaped pores (pillar size 0.43 mm, porosity 0.27, permeability 17 D. Open spaces appear black, pillars white; right image shows solid, water, and TCE phases (adapted with permission from Jeong *et al.*[113] Copyright © 2000 American Chemical Society). (B) Salt precipitation during CO_2 storage in a PDMS medium with circular pillars (diameter 550 μm, porosity 0.52, depth 25 μm). Open spaces are purple, pillars white; right image shows salt crystals (adapted with permission from Ho and Tsai.[116] Copyright © 2020 Royal Society of Chemistry). (C) Visualization and modeling of transverse mixing and reaction (Oregon Green 488 Bapta-5N with Ca^{2+}) in a homogeneous chip with elliptic pillars (porosity 0.33, depth 25.9 μm). Right: Lattice-Boltzmann model of product concentration (adapted with permission from Willingham *et al.*[115] Copyright © 2008 American Chemical Society).

2.3.2 Heterogeneous pore structure. To better represent natural porous media, researchers have developed a variety of heterogeneous microfluidic designs. In some cases, the lattice (pillar arrangement) is kept constant, but pore and pillar sizes are varied to introduce permeability changes (Fig. 5A). Within each permeability layer, pore sizes may remain constant[80,121,125] or follow a defined size distribution (compare Fig. 5A and B).[122] Fractures—characterized by 100% porosity and high permeability—are another important feature in natural rock structures and have been incorporated into microfluidic designs (Fig. 5C).[59,81,122,125] Such permeability contrasts promote preferential flow paths, where high-permeability regions with lower resistance are invaded earlier.[59,121,122]

Another approach involves 2.5-D microfluidic chips, in which channel depth varies locally to create layered permeability contrasts (Fig. 5D). This form of heterogeneity is particularly useful for investigating multiphase flow phenomena such as capillary snap-off and stratified fluid distributions.[123,124,126,127]

To replicate the anisotropic and heterogeneous structure of natural rocks, early studies patterned microfluidic chips using 2D thin-section images derived from rock samples. Thin sections (Fig. 6A and B) were prepared and imaged by micro-CT,[128,129] petrographic microscopy,[130,131] scanning electron microscopy (SEM),[132] or epoxy impregnation.[133] In more advanced work, 3D micro-CT scans of rock samples were used to extract multiple 2D slices, which were then stacked to generate an averaged representation (Fig. 6C).[128,134,135] Pore and throat network statistics[128,135] or artificial random networks[136] were integrated to restore connectivity lost during slicing, yielding designs more representative of the original core structure. In other approaches, 3D pore networks reconstructed from SEM and micro-CT scans were analyzed for pore statistics and then converted into 2D designs that preserved size distributions and selected 3D features (Fig. 6C and D).[137]

A recent development in realistic microfluidic porous media is the creation of geo-material micromodels.[134,138,139] In this method, thin slices of actual rock are either polished or laser-etched and sealed between glass slides for direct visualization (Fig. 6E). This method incorporates natural mineralogy, surface roughness, and wettability, enabling the study of geochemical interactions that strongly influence pore-scale flow.[46,139–141] Alternatively, mineral coatings have been applied to PDMS[142] or glass[123] devices to capture rock–fluid interactions.

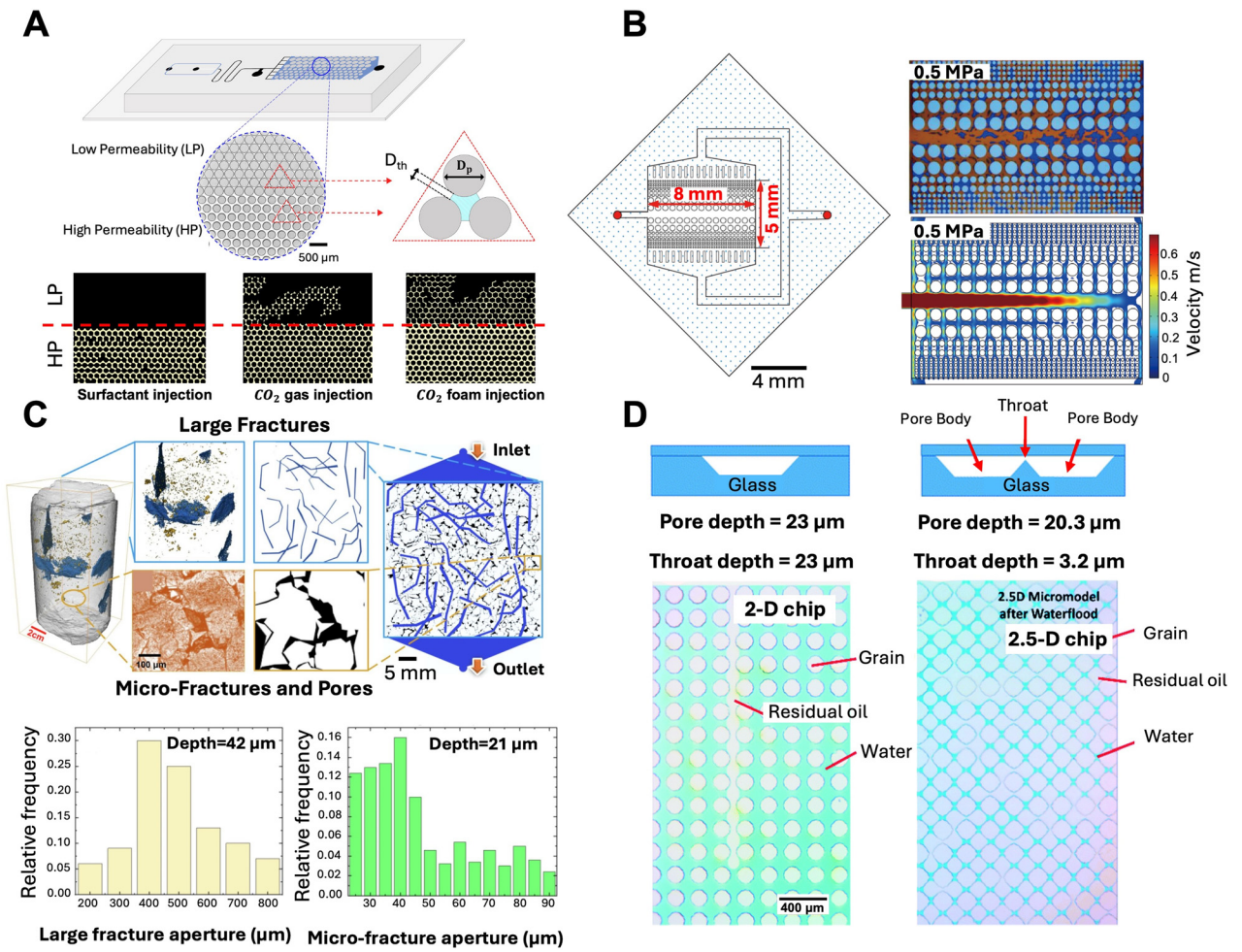

Fig. 5 Heterogeneous microfluidic pore networks. (A) Fluid displacement in a dual-permeability PDMS chip with circular pillars (210 μm, 250 μm) and throats (60 μm, 21 μm); depth 100 μm. Oil and pillars are black, displacing fluids yellow (adapted with permission from Moradpour and Tsai.[121] Copyright © 2025 Royal Society of Chemistry). (B) Fracturing fluid propagation in a multi-permeability chip simulating fracture-matrix zones. Pillars: 200, 100, 50 μm; throats: 125, 80, 70 μm; central fracture: 500 μm; depth 30 μm. Right: Guar gum fluid (blue), oil (brown), and velocity map at ΔP = 0.5 MPa (adapted with permission from Da *et al.*[122] Copyright © 2022 KeAi Elsevier). (C) Oil displacement by CO_2 in a fractured micromodel replicated from carbonate rock micro-CT. Glass chip patterned and etched to include large and micro fractures; mean depths 42 μm and 21 μm (adapted with permission from Lv *et al.*[123] Copyright © 2022 Elsevier). (D) Oil displacement by water in 2D and 2.5D hydrophilic micromodels. *N*-Octane (gray) displaced by dyed water (blue); capillary snap-off observed only in 2.5D chip (adapted with permission from Xu *et al.*[124] Copyright © 2017 Royal Society of Chemistry).

A major limitation of standard simplified microfluidic models is dimensionality: most are quasi-2D, whereas rocks are inherently 3D. Structural complexities such as anisotropic vertical permeability and tortuosity,[143] as well as flow phenomena such as cross-flow,[144] are difficult to reproduce in 2D but can be captured with 3D micromodels. In this regard, several fabrication strategies have been explored, including multilayered polymers,[126,145] packed particles,[146–148] and 3D printing.[149,150] For example, thermoplastics such as PMMA can be stamped with 3D molds at high temperature and pressure (172 °C, 24 kN) to replicate pore structures.[126] Similarly, packing micron-sized glass beads between plates produces disordered 3D porous media, which can be imaged by refractive index matching between beads and fluorescent fluids (Fig. 7E).[148,151] Bead size can be uniform or varied to represent homogeneous or heterogeneous media.[143] Finally, additive manufacturing approaches such as stereolithography[152] and material jetting[150] allow direct 3D printing of porous media based on real rock scans.

2.4 Pore-scale visualization methods

Conventional coreflooding involves injecting fluids through opaque, oil-saturated rock cores and requires *in situ* 3D imaging to monitor fluid displacement. Common methods include X-ray micro-computed tomography (micro-CT), nuclear magnetic resonance (NMR), and magnetic resonance imaging (MRI). In contrast, microfluidic platforms are typically quasi-2D and transparent, enabling real-time visualization with optical microscopy. The following subsections and Table 1 compare these methods, outlining their advantages and limitations for pore-scale flow studies.

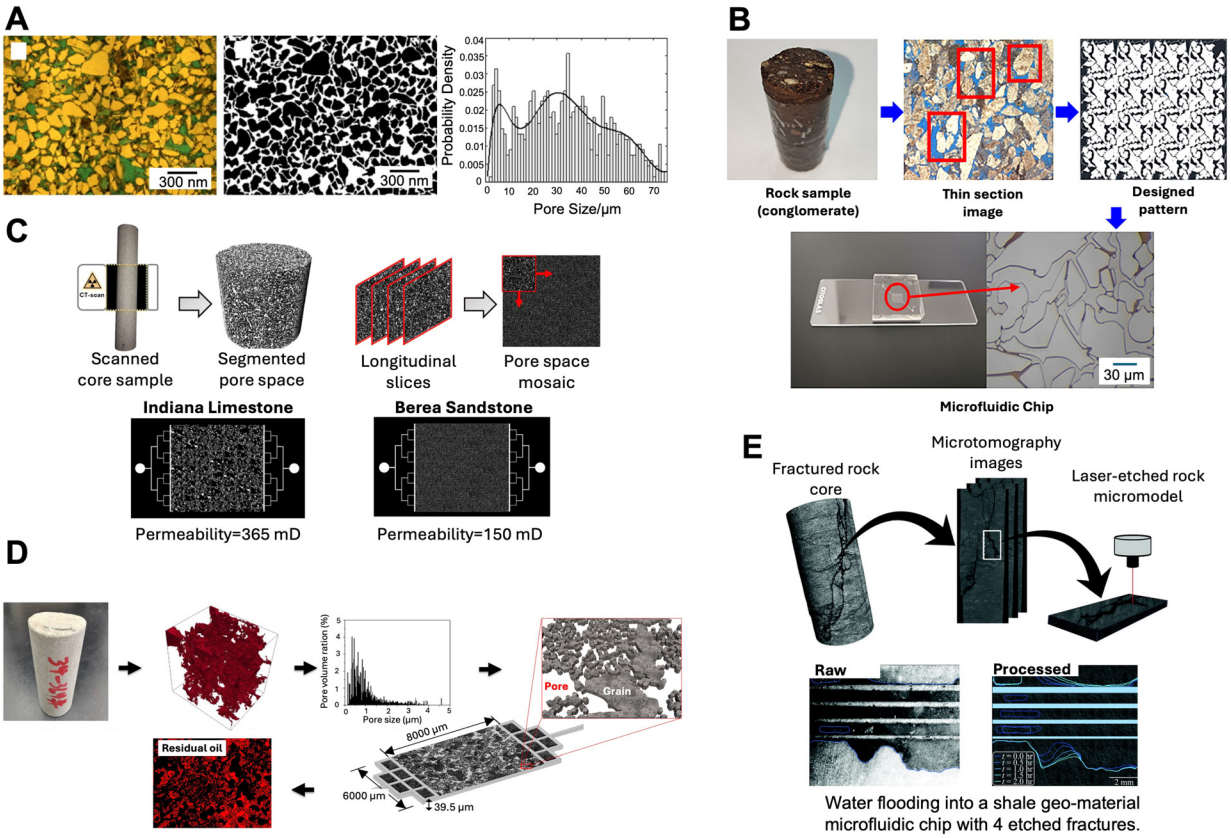

Fig. 6 Rock-on-chip heterogeneous networks. (A) CO_2 exsolution from carbonated water in a microfluidic chip based on a thresholded thin-section image of low-permeability sandstone; pore sizes ranged from 2–74 μm (adapted with permission from Zuo *et al.*[130] Copyright © 2013 Elsevier). (B) Oil recovery visualization using alkaline-surfactant-polymer (ASP) with SiO_2 nanoparticles in a PDMS chip patterned from a sliced conglomerate rock; mean pore size: 30 μm, depth: 10 μm (adapted with permission from Wang *et al.*[131] Copyright © 2022 American Society of Chemistry). (C) Multi-step reconstruction of sandstone and limestone pore morphology: 3D micro-CT scans segmented and mosaicked into 2D designs with controlled throat sizes and permeability (adapted with permission from Godoy *et al.*[135] Copyright © 2025 Royal Society of Chemistry). (D) Micro-gel-assisted oil recovery in a chip designed from CT, SEM, and FIB-SEM scans of tight sandstone samples; chip depth: 39.5 μm; red fluorescence shows displaced residual oil (adapted with permission from Lei *et al.*[137] Copyright © 2020 Wiley). (E) Matrix–fracture fluid interaction during water displacement by supercritical CO_2. 2D fracture geometries laser-etched onto shale from micro-CT scans; fracture apertures: 100–400 μm, depth: 100 μm (adapted with permission from Porter *et al.*[134] Copyright © 2015 Royal Society of Chemistry).

2.4.1 Coreflooding: X-ray micro-computed tomography (micro-CT). Micro-CT reconstructs 3D internal pore structures by rotating a sample while collecting 2D X-ray projections.[156] Synchrotron-based micro-CT, which uses a much higher-intensity X-ray source, offers improved spatial (≈3–10 μm) and temporal (0.5–5 min) resolution, but requires access to costly, specialized facilities.[157,158]

Using time-resolved 3D imaging, Andrew *et al.*[157] employed synchrotron-based micro-CT to capture snap-off events during supercritical CO_2 drainage, allowing estimation of local capillary pressure from interfacial curvature.[157] This technique has also been used to study gas trapping[153] and CO_2 cluster distributions in porous media.[159,160] Fig. 7A shows an example of gas, oil, and water 3D distribution during waterflooding.[153] Micro-CT imaging resolves pore-scale interface dynamics within a millimeter-scale field of view, capturing features such as interface curvature, snap-off events, and CO_2 cluster connectivity in centimeter-scale core plugs during coreflooding experiments.[158]

2.4.2 Coreflooding: nuclear magnetic resonance (NMR) and magnetic resonance imaging (MRI). NMR and MRI detect signals from hydrogen nuclei (^1H) in fluids using a magnetic field and radiofrequency pulses.[141,161] MRI reconstructs these signals into images of ^1H-containing fluids —mainly oil and water—within the rock core. CO_2 is not detected because it lacks hydrogen atoms.

Fig. 7B shows an MRI image where intensity reflects oil saturation. MRI provides spatial resolution of O(10–100 μm),[141] lower than micro-CT and insufficient to resolve individual pores or interfacial features.[161] Nonetheless, MRI remains useful for tracking saturation and displacement in heterogeneous reservoirs. For example, in Fig. 7B, Zhao *et al.*[154] observed gas channeling under immiscible CO_2 injection, whereas miscible supercritical CO_2 produced a more uniform, piston-like displacement and higher oil recovery.[154]

Overall, coreflooding visualization methods capture native porous media and fluid–solid interactions but are limited by

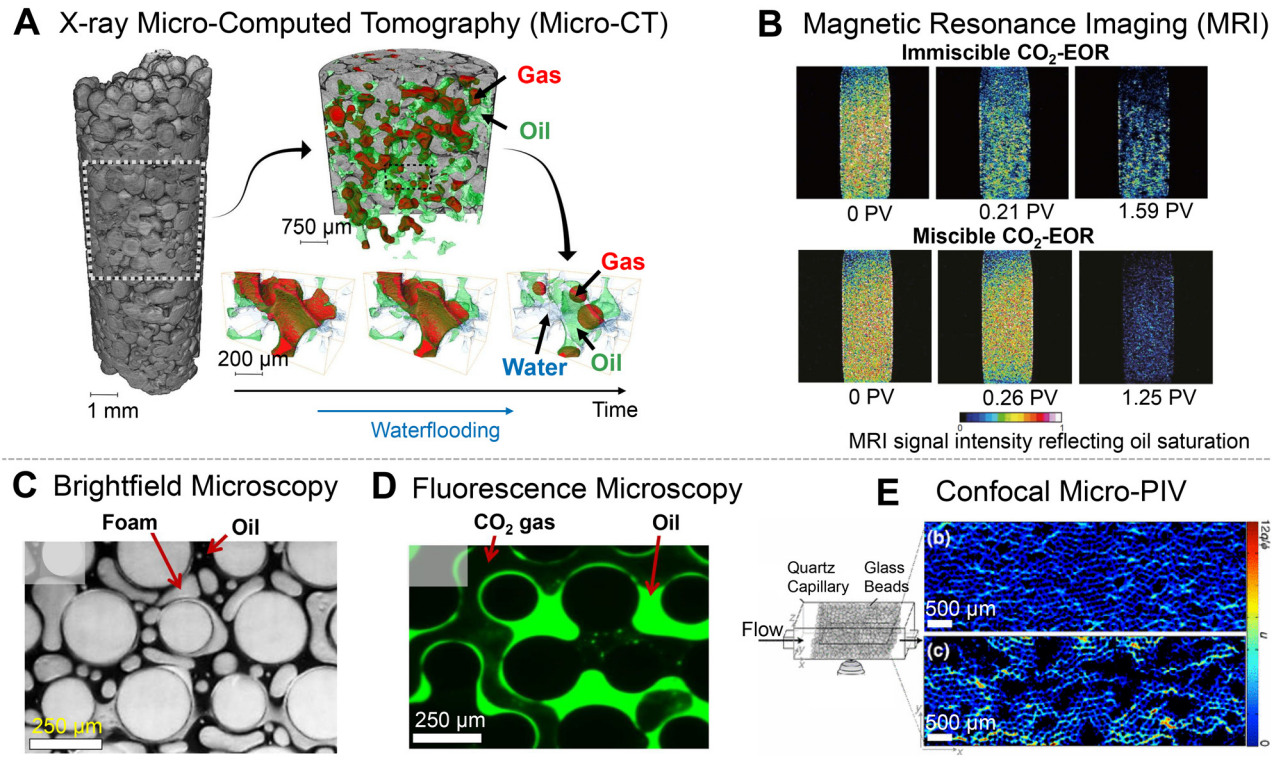

Fig. 7 Pore-scale visualization techniques for subsurface flow. (A) Synchrotron-based X-ray micro-computed tomography (micro-CT) imaging of a CO_2–oil–water system during waterflooding in a carbonate core, showing gas (red), oil (green), and water (blue) distributions in 3D (adapted with permission from Scanziani *et al.*[153] Copyright © 2019 Elsevier). (B) Magnetic resonance imaging (MRI) of oil saturation distribution in a core following waterflooding and supercritical CO_2 injection (adapted with permission from Zhao *et al.*[154] Copyright © 2011 China University of Petroleum (Beijing) and Springer-Verlag Berlin Heidelberg). (C) Brightfield microscopy visualization of gas–liquid interfaces in a microfluidic pore network. (D) Laser-induced fluorescence (LIF) imaging of CO_2 dissolution in oil within a micromodel (C and D adapted with permission from Nguyen *et al.*[155] Copyright © 2014 American Chemical Society). (E) Confocal microscopy combined with particle image velocimetry (PIV) to quantify velocity fields in a glass bead-packed microchannel (adapted with permission from Datta *et al.*[151] Copyright © 2013 American Physical Society).

Table 1 Summary of pore-scale visualization methods for coreflooding and microfluidics

Visualization method	Typical field of view	Spatial & temporal resolution	Advantages	Limitations
Coreflooding micro-CT	mm-scale	≈3–10 μm (synchrotron); ≈10–20 μm (lab) ≈0.5–5 min (synchrotron); slower for lab CT	(1) True 3D pore-scale imaging in native rock (2) Captures interfacial morphology and snap-off	(1) Limited FOV (mm in cm plugs) (2) Synchrotron access costly (3) Computationally intensive
Coreflooding – NMR/MRI	cm-scale	O(10–100) μm O(1–10) min	(1) Captures bulk fluid distribution (2) Sensitive to saturation and transport	(1) CO_2 not visible (no ^1H) (2) Insufficient spatial resolution for individual pores (3) Expensive instrumentation
Microfluidic – optical imaging	mm–cm scale	Sub-μm (optical limit) Sub-ms with high-speed cameras	(1) Transparent, real-time visualization (2) Versatile optical techniques (brightfield, fluorescence, confocal, PIV, *etc.*)	(1) Limited depth of field (2) Difficult to reproduce fully 3D fluid interfaces and pore events

the opacity of rock cores, reliance on specialized equipment, and restricted availability of advanced tools such as synchrotron-based micro-CT. Real-time imaging is further constrained by temporal resolution, and the resulting data often require intensive computational processing.

2.4.3 Microfluidics: optical imaging techniques. Microfluidic platforms offer distinct advantages in pore-scale visualization compared to coreflooding methods. Their intrinsic transparency allows direct optical access and real-time monitoring of multiphase flow with high spatial and temporal resolutions. When combined with microscope systems and high-speed cameras, these setups can resolve dynamic processes at sub-millisecond timescales and sub-micron length scales.[141,162]

A range of optical techniques is used in microfluidics. Brightfield microscopy is the most common, providing clear

visualization of droplet interfaces and flow patterns (Fig. 7C, Nguyen *et al.*[155]). Laser-induced fluorescence (LIF) enhances phase contrast by tagging one fluid with a fluorescent dye, leaving the background dark (Fig. 7D, Nguyen *et al.*[155]). Fluorescence intensity can also be used to quantify CO_2 dissolution into surrounding oil or water to study diffusion, miscibility, and interfacial transport, as discussed in sections 3.2 and 4.2.

Confocal microscopy offers better resolution by rejecting out-of-focus light with a pinhole aperture. Scanning vertically across the channel depth allows the reconstruction of optical slices that approximate 3D features. For example, Datta *et al.*[151] combined confocal microscopy with particle image velocimetry (PIV) to map flow fields in bead-packed micromodels (Fig. 7E, Datta *et al.*[151]). Refractive index matching between the fluids and beads allowed clear visualization of flow, while PIV quantified velocity fields using tracer particles in fluids.[151] However, a limitation is speed: a standard laser scanning confocal microscope is relatively slow, operating at only ≈10 slices per second,[151] which limits its ability to capture rapid multiphase flow dynamics.

Despite their predominantly quasi-2D design, microfluidic devices provide high-resolution visualization of multiphase flow and can be extended to 3D geometries, enabling more complete capture of the fluid interface similar to volumetric methods such as micro-CT.

2.5 Machine learning coupled with microfluidic systems

In the rise of the artificial intelligence (AI) era, incorporation of machine learning (ML) in research is undoubtedly common in many disciplines. In microfluidic experiments, performance prediction and control/optimization of operational parameters *via* intelligent microfluidics is one of the main applications.[163–170] Intelligent microfluidics refers to the integration of automation, AI, and real-time sensing into microfluidic systems to enhance the control, optimization, and adaptability of fluid flow and chemical/biological processes at the microscale. These systems leverage ML, smart sensors, and computational models to make real-time decisions, adjust operational parameters, and improve efficiency without human intervention.[165,166] For instance, in two-phase flow within micropores, Song *et al.*[171] developed an intelligent microfluidics platform combining image recognition and deep learning to predict relative permeability. Their model showed relative contributions of 38.22% from saturation, 34.84% from wettability, and 26.94% from pore geometry.[171] Future studies can expand this technique to complex rheology injection fluids (*e.g.*, surfactant, foam), and adapt toward real-time monitoring, where live microscopy images are used to optimize injection parameters.

In predicting capillary pressure, ML models offer data-driven alternatives to traditional empirical fits. Qi *et al.*[172] used ensemble methods to estimate capillary pressure curves from particle size distributions, while Liu *et al.*[173] and Kasha *et al.*[174] applied neural networks and other supervised models (*e.g.*, clustering) to predict both capillary pressure and relative permeability from pore structure data. Similarly, Khosravi *et al.*[175] used a hybrid of particle swarm optimization and ML to estimate relative permeability and capillary pressure under low-salinity flooding. Because relative permeability and capillary pressure govern phase mobility and distribution, such ML frameworks are especially relevant for multiphase systems. Capillary pressure, in particular, is critical in systems where phase separation, drainage/imbibition hysteresis, or capillary trapping occurs, such as carbon storage and oil recovery (discussed in sections 3 and 4).

Furthermore, Manikonda *et al.*[176] used *K*-nearest neighbors and multi-class support vector machine to classify gas–liquid flow regimes with up to 98% accuracy, demonstrating ML's value for automated displacement regime identification.[8] Zhao *et al.*[177] implemented a U-Net deep learning structure combined with orthogonal design for data generation, expediting prediction of displacement front under different permeability contrasts, Ca numbers, and viscosity ratios.[9] Accurate prediction of displacement front morphology in heterogeneous porous media is particularly critical for understanding channeling and improving recovery efficiency.

Meanwhile, at the micromodel design stage, ML can also generate synthetic pore geometries from statistics of real rock structures, supporting more realistic benchmarking and simulation workflows.[163] In pore-scale modeling, image enhancement using ML is implemented to maintain a wider field-of-view without sacrificing the resolution of the images.[163,165] However, it is well known that obtaining data to train a ML model is often costly and time-consuming, particularly with microfabrication of microfluidic chips to cover a wide range of experimental parameters. Transfer learning allows the majority of the data to be collected from modeled chips—such as 3D printing, micromilling, laser cutting—then combined with a small portion of data on devices made with photolithography and micropatterned electrodes. The refinement of transfer learning opens the possibility of rapid prototyping for data generation.[164]

Future research should aim to combine ML with experimental microfluidic data to bridge the gap between 2D and 3D,[178] and between lab-scale and reservoir-scale—specifically in terms of predicting accuracy in a more complex natural environment—for underground storage applications.[165] Furthermore, the integration of time-evolution algorithms (*e.g.*, transformer neural networks) can significantly shorten experimental processes by using initial time series data to make future predictions. This ML tool may be useful in processes, such as bacteria growth, gas distribution/movement in long-term underground storage, *etc.*

3 Microfluidic investigations on CO_2-EOR

CO_2-EOR is a mature and widely used method where CO_2 is injected into oil-bearing subsurface formations to increase oil recovery. Statistics show that 34% of global CO_2 demand is consumed by EOR projects,[179] with over 200 projects[180] of miscible and immiscible CO_2 injections. This number may rise as oil production from CO_2-EOR is expected to increase to 1.6 barrel per day by 2040.[181] Besides, CO_2 accounts for 64% of the greenhouse gasses,[182] making the injection of emitted CO_2 into sealed underground formations a recognized technique for contributing to CO_2 geological storage and reducing the carbon footprint of hydrocarbon extraction.[5] The significance of underground CO_2 storage is indicated by the current (50) and future (578) storage facilities, with capacities of 51 million and 563 million tonnes per year, respectively.[183]

CO_2 injection has been examined across different scales—pore,[123,184,185] core (lab),[186–188] and field.[189] When CO_2 is injected below the minimum miscibility pressure (MMP) with the oil phase, it cannot fully mix in the oil phase and fails to form a single homogeneous phase, resulting in an immiscible displacement process.[190–192]

Microfluidic investigations have provided valuable insights into immiscible CO_2-EOR[118,193–196] (section 3.1). Unlike CCS in saline aquifers, where CO_2 slightly dissolves in brine, in oil reservoirs, CO_2 exhibits higher solubility in oil and can become miscible under pressures greater than MMP,[197] which can lead to nearly complete oil recovery. This complex CO_2–oil phase behavior has motivated many microfluidic studies on minimum miscibility pressure[198–207] and miscible CO_2-EOR mechanisms[208–212] (section 3.2). Microfluidics has also been instrumental in exploring CO_2 huff-n-puff techniques[25,212–217] (section 3.3), where gas exsolution (*i.e.*, CO_2 separates from the formerly homogeneous oil phase[214]) enhances oil recovery. Foam-assisted CO_2-EOR, another widely studied approach, improves sweep efficiency by increasing apparent viscosity.[59,218–220] Further discussions on CO_2 bubble dynamics and oil displacement mechanisms are presented in section 3.4.

3.1 Immiscible CO_2-EOR

The first field-scale immiscible CO_2 injection for EOR application was conducted in Arkansas, USA, in 1968.[189] The primary mechanisms underlying oil displacement by immiscible CO_2 gas injection are oil swelling and oil-viscosity reduction due to CO_2 dissolution and interfacial tension (IFT, σ) reduction.[191,221–223] Under immiscible conditions, higher oil–CO_2 interfacial contact area enhances gas dissolution, crucial for triggering oil mobilization mechanisms.[224–226] The spreading coefficient of oil over water ($S_{o/w}$) serves as an indicator of CO_2 injection efficiency, defined as:[227–229]

$$S_{o/w} = \sigma_{wg} - \sigma_{og} - \sigma_{ow}, \quad (1)$$

where σ_{wg}, σ_{og}, and σ_{ow} are the water–gas, oil–gas, and oil–water interfacial tensions, respectively. In hydrophilic porous media, a positive spreading coefficient ($S_{o/w} > 0$) contributes to the spreading of oil films between the water and gas phases. However, in hydrophobic media, a negative spreading coefficient ($S_{o/w} < 0$) causes gas bubbles and liquid droplets to disperse and enter in the oil phase. Hence, the contact area between oil–CO_2 and consequently the performance of immiscible CO_2 injection is maximized.[229–231]

However, if these criteria of positive (or negative) $S_{o/w}$ values for hydrophilic (or hydrophobic) surfaces are not met, other scenarios, such as CO_2 saturated (*i.e.*, carbonated) water injection, can provide better fluid distribution.[232] In hydrophilic porous media with a negative spreading coefficient, water prevents CO_2 from reaching oil ganglia. Injecting carbonated water allows CO_2 to partition from the water and dissolve in the oil, causing oil swelling that disrupts the water barriers and increases the contact area of oil with free CO_2 gas.[193,229] Microfluidic visualization has contributed to a better understanding of the mechanism behind improved oil recovery by carbonated water injection observed in opaque core-flooding experiments. Carbonated water injection outperforms traditional waterflooding as well,[193,233,234] due to CO_2 diffusion from water into the oil phase, reducing oil viscosity and decreasing water–oil IFT.

A second approach to increase the performance of immiscible CO_2 injection is water alternating gas (WAG) flooding, where sequential slugs of water and CO_2 are injected to increase the sweep efficiency.[194,210] Hao *et al.*[210] compared immiscible CO_2 and WAG injection into a vertical heterogeneous glass microfluidic chip. Their observations indicated that when injecting immiscible CO_2, gravity override caused CO_2 to flow preferentially toward the top part of the chip with only 39.2% sweep efficiency. The analysis of buoyancy, capillary, and hydrodynamic forces indicated the greatest total magnitude in the upward direction (2.06×10^{-5} N). In contrast, injecting alternating slugs of water causes pore throat blockage, which increases capillary resistance and allows CO_2 flow in other directions. Therefore, WAG increased the sweep efficiency to 97.9%.[210] However, Riazi *et al.*[235] found that a two-step injection sequence of water followed by supercritical CO_2 accelerated breakthrough, as the presence of water–oil interfaces impeded lateral CO_2 propagation.[235] If immiscible WAG injection into a hydrophilic medium begins with CO_2 as the first slug, the process is more effective. This is because gas, as the non-wetting phase, is less likely to trap and shield the oil phase compared to the wetting water phase.[194]

Another strategy to enhance the efficiency of immiscible CO_2 injection is to replace CO_2 gas with supercritical CO_2, which increases the CO_2 solubility in oil[236] and reduces oil–CO_2 IFT.[237] Riazi *et al.*[235] observed that supercritical CO_2 significantly delayed breakthrough time, (about 75% slower) due to the increased viscosity of CO_2.[235] With improved CO_2

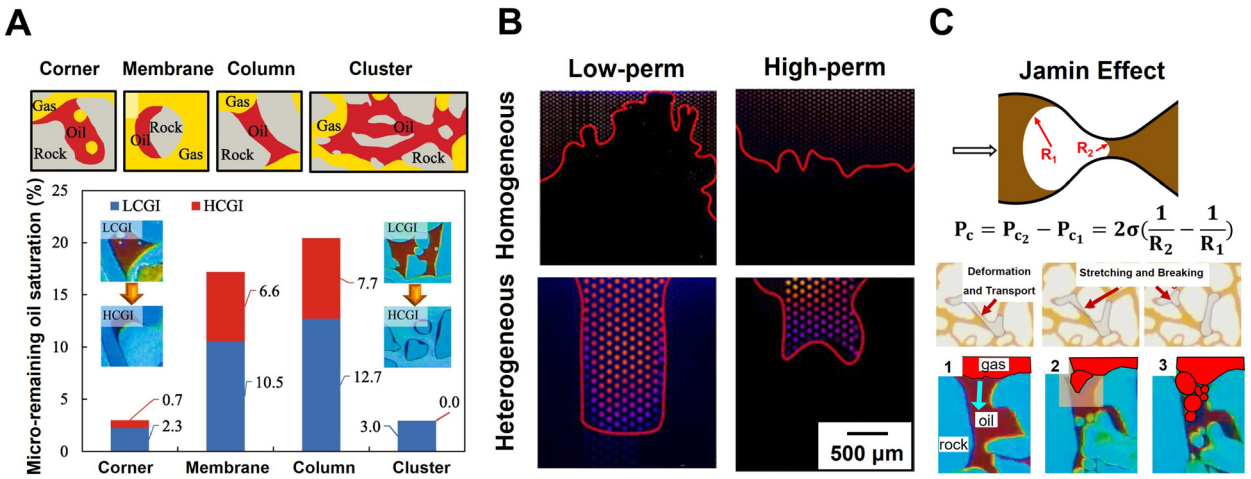

Fig. 8 Microfluidic results for oil displacement by immiscible CO_2 injection: (A) different residual oil configurations (red) remained in a heterogeneous porous medium after low-flow gas (yellow) injection (top). Their respective contributions for the remaining residual oil after low (LCGI, blue) followed by high (HCGI, red) continuous gas injection to displace oil in the heterogeneous microfluidics (adapted with permission from Chen *et al.*[195] Copyright © 2024 Elsevier). (B) Displacement of *n*-octane (dyed) by immiscible CO_2 injection in homogeneous microfluidic porous media with low (left) and high (right) permeability (top). Similar displacement into a heterogeneous one including a matrix with low (left) and high (right) permeability plus lateral fractures (bottom). CO_2 injected from bottom to top, oil–gas interface shown as a red line (adapted with permission from Pan *et al.*[118] Copyright © 2025 the Royal Society of Chemistry). (C) Jamin effect: gas (white) travels from a large pore (R_1) to a smaller one (R_2), it undergoes deformation resulting in additional capillary resistance (P_s) and bubble pinch-off (top). σ is the IFT of the residing fluid (brown) and the gas phase (idea adapted from Chen *et al.*[195]). Bubble pinch-off phenomenon due to the Jamin effect observed in microfluidic visualizations during oil (brownish) displacement by immiscible CO_2 injection (adapted with permission from Qian *et al.*[196] Copyright © 2025 Elsevier and Chen *et al.*[195] Copyright © 2024 Elsevier).

solubility, mass transfer of light to intermediate oil components into the CO_2 gas, known as vaporizing extraction, occurs. These components subsequently recondense under ambient pressure–temperature conditions, contributing to improved oil recovery.[235,236,238] This mechanism has been found effective even when CO_2 remains in the gas phase, but injected at higher pressure[196,212] or flow rate.[194,195] By increasing the hydrodynamic driving force, CO_2 can overcome the opposing capillary force to enter smaller pores and interact (dissolution and extraction) with unswept oil saturation. In this regard, Chen *et al.*[195] investigated the effect of increasing the CO_2 injection rate by 25-fold in a heterogeneous glass microfluidic chip. Their results revealed that a higher flow rate mobilized 'columnar' and 'membrane' trapped oils in both high (see Fig. 8A) and low permeable areas, but left cluster-shaped oils in the low permeability zones largely unaffected. Overall, the oil recovery factor improved by 14.2% at the higher injection rate.[195] Furthermore, they suggested that replacing continuous injection with asynchronous gas injection and production cycles increased the oil recovery by 20%. This improvement was attributed to pressure buildup and increased CO_2 dissolution and extraction during shut-in periods, which primarily liberated cluster-shaped trapped oils. In another study, pore-scale visualizations by Guo *et al.*[212] revealed a shift from capillary-dominated to viscosity-dominated flow as the pressure difference across the chip increased from 0.01 MPa to 0.03 MPa. Despite the positive impacts, increasing the velocity of the non-wetting CO_2 phase shortens the breakthrough time, which is a critical concern that must be addressed.[80,194]

Heterogeneity in porous media considerably affects CO_2 distribution, and accordingly sweep efficiency and oil recovery factor.[118,195,212,239] Tang *et al.*[239] designed four different hydrophobic glass micromodels patterned by laser etching and wet-etched with hydrofluoric acid.[239] Their results of water flooding followed by immiscible CO_2 injection showed that fractures improve fluid distribution (for both water and CO_2) and increase sweep efficiency, although a higher permeability contrast between fractures and the matrix can lead to early breakthrough and reduced oil recovery. Moreover, they observed that CO_2 injection improved oil recovery up to 20% by mobilizing the residual oils after water flooding that were entrapped in cluster shapes and dead corners, consistent with observations by Qian *et al.*[196]

Displacing *n*-octane by immiscible CO_2 at 70 °C and 6.5 MPa, Pan *et al.*[118] demonstrated that shale-like nano-scale heterogeneity influences transport phenomena.[118] Regardless of permeability, homogeneous porous media resulted in 100% oil recovery despite gas fingering (see Fig. 8B-top). In contrast, heterogeneous fractured porous media facilitate gas channeling through the fractures, which are the preferential low resistive flow paths (see Fig. 8B-bottom). Therefore, driven by pressure drop, oil displacement initiated from the side channels. Gradually CO_2 entered the porous matrix and mobilized the oil by both pressure drop and CO_2 diffusion and dissolution in oil. The intensity of CO_2 diffusion was greater in matrix pores adjacent to the fractures. In addition, the permeability of the

matrix is a key parameter affecting the resisting capillary force, a critical point in fluid–fluid displacement. Pan *et al.*[118] achieved 100% oil recovery in the high permeability chip, while the low permeability design recovered only 30% of the oil. In heterogeneous porous media, CO_2 can become isolated due to bubble pinch-off and immobilization at low permeability pore throats, a phenomenon known as the Jamin effect (see Fig. 8C).[195,196,235] This limitation can be mitigated by increasing the injection pressure, which not only enhances sweep efficiency but also improves CO_2 storage.[196]

3.2 Miscible CO_2-EOR

3.2.1 Minimum miscibility pressure (MMP). Miscibility in the context of CO_2-EOR refers to the ability of two fluids to mix and form a homogeneous mixture without forming separate phases. It is categorized into first-contact miscibility (FCM) and multiple-contact miscibility (MCM) in petroleum applications.[240,241] FCM occurs when fluids mix immediately upon contact in any proportion, exemplified by a binary system, such as normal pentane (*n*-pentane, C_5) and normal decane (*n*-decane, C_{10}).[241] In real-world CO_2-EOR applications involving complex multicomponent systems, crude oil typically comprises light (C_1), intermediate (C_2–C_6), and heavy fractions (C_{7+}).[242,243] When CO_2 interacts with these crude oil components, MCM develops as mass transfer and component exchange occur between CO_2 and oil,[206,241] with miscibility gradually achieved through continued fluid interaction and flow.[206,241]

The minimum miscibility pressure (MMP) is the critical pressure at which two fluids become miscible, influenced by both temperature and fluid composition.[242,243] For CO_2 and oil systems, MMP values typically range from 7 to 34 MPa.[242] Accurate determination of MMP is crucial for selecting reservoirs suitable for CO_2-EOR.[242,243] When reservoir pressure exceeds the MMP, miscible flooding occurs and enables near-complete oil recovery.

Standard lab-scale experimental methods for determining MMP include the vanishing interfacial tension (VIT) method,[244,245] the rising-bubble apparatus (RBA),[246] and slim tube tests (STT).[242,247] These conventional methods, while reliable, are often time-consuming and require significant

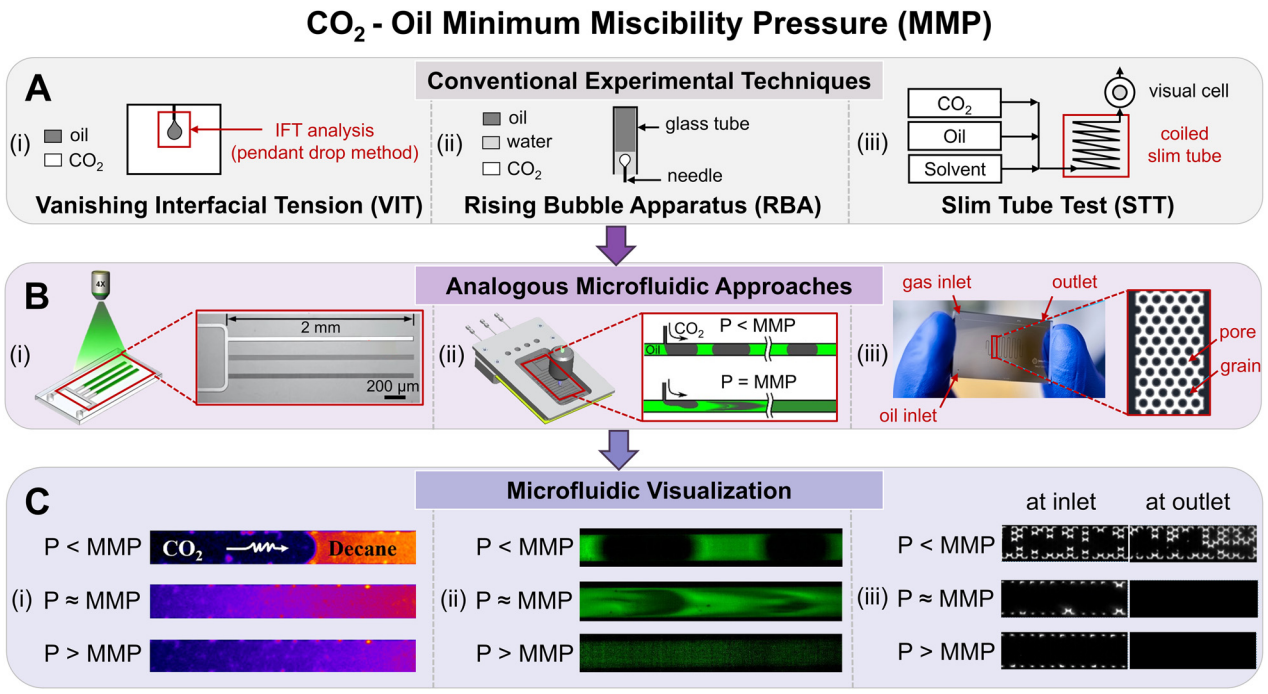

Fig. 9 Summary of microfluidic experiments for determining CO_2–oil minimum miscibility pressure (MMP). (A) Schematic illustrations of three commonly used conventional techniques: (i) vanishing interfacial tension (VIT): the pendant drop method measures the interfacial tension (IFT) between the oil drop and surrounding CO_2, with the MMP determined when the IFT approaches zero; (ii) rising bubble apparatus (RBA): a CO_2 bubble rises through oil in a glass tube, and the MMP is identified by observing bubble interfacial disturbance. (iii) Slim-tube testing (STT): CO_2 is injected into an oil-filled coiled tube, and MMP is determined at the plateau of oil recovery. (B) Microfluidic designs inspired by the conventional techniques in part (A), showing their analogous setups for MMP determination. (i) A microfluidic chip with dead-end pores visualizes a static CO_2–oil interface (adapted with permission from Shi *et al.*[200] Copyright © 2024 Elsevier). (ii) Microfluidic fast fluorescence imaging captures CO_2 bubble flow in oil (adapted with permission from Nguyen *et al.*[203] Copyright © 2015 American Chemical Society). (iii) A "slim-tube on a chip" simulates oil recovery by injecting CO_2 into a serpentine channel with embedded solid grains (adapted with permission from Ungar *et al.*[204] Copyright © 2021 Elsevier). (C) Microfluidic visualization of CO_2–oil interactions at pressures below, near, and above MMP for the corresponding approaches in part (B). For $P <$ MMP, the CO_2–oil interface appears sharp, and incomplete oil recovery is observed in the slim-tube chip. For $P \geq$ MMP, the CO_2–oil interface becomes blurred, with nearly complete oil recovery in the slim-tube chip (adapted with permission from Shi *et al.*,[200] Nguyen *et al.*,[203] Ungar *et al.*[204]).

fluid volumes. In response, microfluidic devices inspired by traditional techniques have emerged as efficient alternatives, reducing testing time and fluid volume while offering clear optical access for real-time observations. Fig. 9 summarizes the conventional experimental approaches (Fig. 9A) and their microfluidic adaptations for MMP determination (Fig. 9B and C).

Vanishing interfacial tension (VIT). The vanishing interfacial tension (VIT) technique measures IFT by observing a pendant drop of CO_2 in oil under varying pressures.[244,245] In microfluidic adaptations, oil is confined in dead-end microchannels, allowing incremental pressurization of CO_2 to study CO_2–oil phase behavior.[198–202] Sharbatian *et al.*[198] observed pressure-dependent oil swelling and extraction, indicating mass transfer before achieving MMP.[198] When MMP was reached, the oil–CO_2 interface disappeared, with fluorescence intensity reaching its minimum (MMP = 7.4 MPa for T = 23 °C and MMP = 10.6 MPa for T = 50 °C).[198] Other studies have shown that MMP increases with temperature due to lower CO_2 solubility.[248] MMP also increases with higher proportions of heavy hydrocarbons in oil.[200] In nanoconfined systems, as channel depth was reduced from 1 μm to 10 nm, MMP of CO_2–octane at 160 °C dropped remarkably from 15.1 MPa to 10.1 MPa.[202] MMP decreases in nanoconfinement, providing insights into CO_2–oil behavior in tight shale reservoirs, where molecular interactions and capillary forces can affect miscibility.[199,202,249]

Rising bubble apparatus (RBA). Rising bubble apparatus (RBA) determines MMP by observing gas bubbles rising in oil.[246] Nguyen *et al.*[203] developed a microfluidic system featuring a T-junction for simultaneous CO_2 and oil injection.[203] Below MMP, a distinct fluorescence gradient marks the CO_2–oil interface; above MMP, this interface disappears, indicating miscibility as fluorescence becomes uniform. This microfluidic method was validated using synthetic oil and used to determine MMP for three field-sourced crude oils, showing MMP ranges of 5.5–8.3 MPa at 25 °C and 8.3–10.7 MPa at 40 °C.[203]

Slim tube test (STT). Compared with VIT and RBA, slim tube tests are more effective for capturing multi-contact miscibility.[241,247] Conventional STT uses a long coiled tube packed with sand or glass beads, with MMP identified at the pressure where oil recovery reaches a high value and starts to plateau.[242,247] Recent microfluidic adaptations, such as slim-tube-on-a-chip systems, use serpentine microchannels filled with circular grains to mimic porous media.[204,206] Ungar *et al.*[204] performed CO_2 flooding in silicon–glass microfluidics,[204] showing 100% oil displacement when the pressure reached MMP.[204] These slim-tube-on-a-chip systems replicate multi-contact miscibility under controlled temperature and pressure with minimal fluid volumes.[204,205]

Microfluidic platforms provide rapid testing and require significantly less fluid volume compared to conventional MMP testing methods. Among various microfluidic approaches, slim-tube-on-a-chip systems are particularly promising for investigating multi-contact miscibility and condensing/vaporizing gas drives. Future studies should focus on comparing MMP results across different microfluidic techniques to standardize and validate these approaches. Beyond MMP determination, microfluidics has proven versatile in studying dew point conditions,[250] wax appearance temperature,[251] solubility, and diffusivity,[198] further demonstrating its diverse applications in analyzing fluid phase behavior in subsurface energy applications.

3.2.2 Miscible CO_2-EOR. Unlike immiscible oil displacement, miscible CO_2–oil displacement eliminates interfacial tension, suppressing viscous fingering[212] and gravity override,[210,211] which significantly improves oil recovery. Miscible CO_2-EOR involves complex multiphase flow and component exchange at the fluid–fluid interface, influenced by factors such as pressure, temperature, fluid composition, and porous media heterogeneity. Multiple mechanisms simultaneously affect the oil recovery efficiency, including CO_2–oil interfacial tension reduction, oil swelling and extraction by CO_2, the formation of a miscibility zone, and asphaltene precipitation.[208,209] Microfluidics has emerged as a valuable tool for visualizing and analyzing these complex miscible displacement processes.

Miscible front. When CO_2 displaces oil above the MMP, a miscibility zone forms at the displacement front through vaporizing and condensing mechanisms.[253,254] In this zone, CO_2 extracts light and medium hydrocarbon components from the oil while also condensing into oil, creating a miscible front.[253,254] To investigate this process, Zhang *et al.*[208] used a glass micromodel to visualize miscible CO_2–oil flooding under high-temperature and high-pressure conditions (up to 115 °C and 55 MPa), with an MMP of 20.37 MPa.[208] Unlike the sharp CO_2–oil interface observed in immiscible CO_2-EOR (Fig. 10A), their study revealed noticeable color gradients across the displacement front (Fig. 10D), indicative of the condensing and vaporizing phase behavior characteristic of a miscible front.[208] In this process, CO_2 dissolves into the oil and condenses at the leading edge of the miscible front, while simultaneously, oil evaporates into CO_2 and is extracted at the trailing edge.[208] Further supporting this mechanism, Zhang *et al.*[201] demonstrated CO_2-induced oil swelling in a dead-end microfluidic channel, confirming CO_2 entry into the oil phase. Together, these processes drive the formation of a condensing–vaporizing miscible front, enhancing CO_2-EOR efficiency.[208]

Moreover, miscible CO_2 injection added 35.4% oil recovery after waterflooding, while carbonated water formed by CO_2 dissolution recovered an additional 11.2% in low-permeability regions.[208] The study also noted asphaltene precipitation[208,209] after lighter crude components were extracted by CO_2, causing microchannel blockages predominantly in low-flow regions like dead-end pores.[208,209] COMSOL simulations further confirmed that blockages were more severe in low-permeability zones, which could lead to potential issues in field applications.[209]

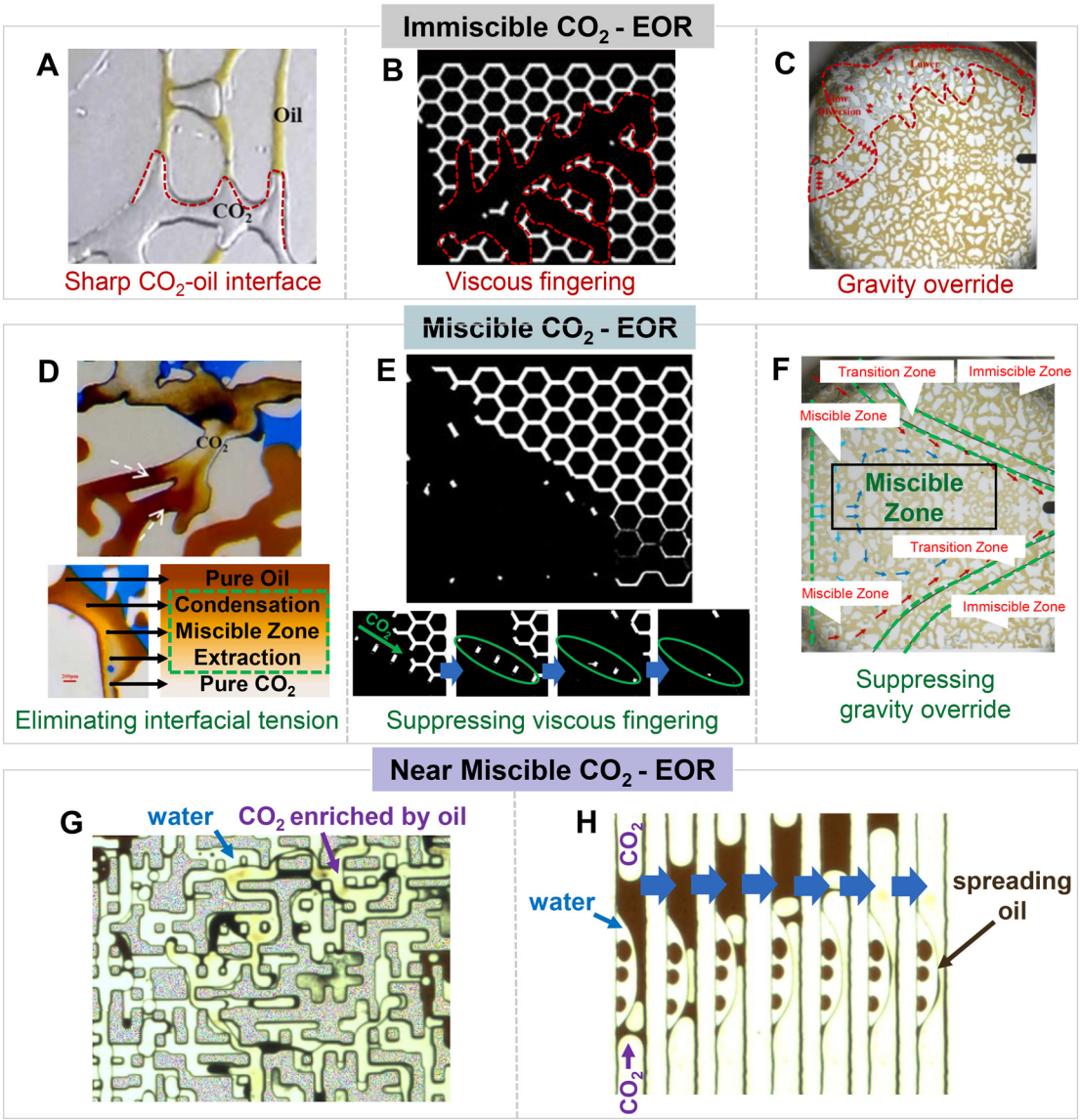

Fig. 10 Comparison of immiscible, miscible, and near miscible CO_2-EOR processes and mechanisms observed in microfluidic experiments. Immiscible CO_2-EOR: (A) immiscible CO_2–oil interface showing sharp phase boundaries (adapted with permission from Zhang *et al.*[208] Copyright © 2022 Elsevier). (B) Viscous fingering leading to unstable displacement front (adapted with permission from Guo *et al.*[212] Copyright © 2022 Elsevier). (C) Gravity override where CO_2 migrates to the top due to buoyancy (adapted with permission from Hao *et al.*[210] Copyright © 2022 Elsevier). Miscible CO_2-EOR: (D) miscible CO_2–oil interface eliminates interfacial tension and promotes mixing (adapted with permission from Zhang *et al.*[208] Copyright © 2022 Elsevier). (E) Viscous fingering is suppressed, leading to efficient oil recovery (adapted with permission from Guo *et al.*[212] Copyright © 2022 Elsevier). (F) Suppression of gravity override and formation of a miscible zone (adapted with permission from Hao *et al.*[210] Copyright © 2022 Elsevier). Near miscible CO_2-EOR: (G) microfluidic visualization showing CO_2 enriched by oil, visible as a darker color within the CO_2 phase (adapted with permission from Seyyedi and Sohrabi.[252] Copyright © 2020 Springer Nature). (H) Near miscible conditions promote oil spreading between CO_2 and water, improving the contact and interaction between CO_2 and oil (adapted with permission from Seyyedi and Sohrabi.[252] Copyright © 2020 Springer Nature).

Viscous fingering. Viscous fingering initially destabilizes the displacement front in miscible CO_2-EOR due to the oil–CO_2 viscosity contrast.[212] However, as CO_2 mixes with oil, the sharp two-phase interface vanishes, and oil viscosity is reduced, stabilizing the displacement.[212] Guo *et al.*[212] demonstrated this effect using a silicon–glass micromodel with CO_2 displacing *n*-decane.[212] For immiscible CO_2-EOR, they observed an unstable displacement front caused by viscous fingering (Fig. 10B). Under miscible conditions, viscous fingering was suppressed, resulting in nearly complete oil recovery (Fig. 10E).[212] A brief soaking period further improved oil recovery by allowing CO_2 diffusion into the oil, promoting mixing and CO_2 penetration.[212]

Gravitational effects. In addition to suppressing viscous fingering, miscible CO_2-EOR also mitigates gravity override. Recent microfluidic experiments studied the gravitational effect during miscible CO_2-EOR by placing the chip

vertically.[210,211] By comparing the displacement patterns of CO_2 in oil at pressures below and above the MMP (Fig. 10C and F), miscible displacement eliminates the gravitational effect, leading to an improvement in oil recovery from 64.3% to 88%.[211] During miscible CO_2-EOR, the formation of distinct zones has been identified, including a miscible zone, a transition zone, and an immiscible zone, as seen in Fig. 10F.[210] Miscible CO_2 flooding also allows CO_2 to penetrate smaller pores, enhancing oil sweep efficiency.[210,211]

3.2.3 Near miscible CO_2-EOR. Even when the reservoir pressure is slightly below the MMP, near miscible CO_2 flooding can still enhance oil recovery.[252,255] Under these conditions, CO_2 dissolves into the oil phase, leading to oil swelling and extraction.[252,255] Seyyedi and Sohrabi used a glass micromodel to investigate this phenomenon of near miscible CO_2-EOR (at 17.2 MPa and 37.8 °C), slightly below the MMP of 19.3 MPa.[252] Although miscibility does not fully develop (shown by a clear interface between CO_2 and oil), lighter oil components diffuse into the CO_2 stream, enriching it, as shown by a visible color gradient in Fig. 10G.[252]

Near miscible conditions also enhance oil recovery by creating a favorable spreading coefficient, which promotes better contact between oil and CO_2.[252,255] A positive spreading coefficient $S_{o/w}$ value (see eqn (1)) indicates that oil spreads on the gas–water interface.[227,228,252] Under near miscible conditions, σ_{og} is sufficiently low to allow $S_{o/w} > 0$.[252] Microfluidic experiments (Fig. 10H) show crude oil spreading between water and CO_2, improving oil extraction and swelling through direct CO_2 contact.[252]

Overall, microfluidic approaches have recently been adopted for determining MMP and investigating key mechanisms in miscible CO_2 oil recovery. Inspired by conventional techniques, such as VIT, RBA, and STT, the microfluidic platform offers direct phase-behavior visualization and rapid MMP analyses, with the potential to be further expanded for broader fluid analyses. Recent microfluidic studies on oil displacement during miscible CO_2-EOR have revealed several important recovery mechanisms, including the condensing–vaporizing gas drive,[208,209] suppression of viscous fingering,[212] and elimination of gravity override.[210,211] Moreover, microfluidic studies demonstrate that near miscible CO_2-EOR is particularly advantageous in reservoirs where achieving full miscibility is challenging due to operational constraints.[252] This technique enhances oil recovery by targeting trapped oil in dead-end pores and improving contact between CO_2 and oil.

3.3 CO_2 huff-n-puff

CO_2 huff-n-puff is an effective EOR technique consisting of three stages: 1) the injection stage ("huff"), where CO_2 is injected into the reservoir; 2) the soaking stage, during which the well is shut in to allow CO_2 to dissolve into the oil; and 3) the production stage ("puff"), where the system is depressurized to produce oil.[256,257] The process can operate under immiscible or miscible conditions depending on reservoir pressure after injection, with miscible or near miscible states significantly enhancing oil recovery.[257–259] Key mechanisms include CO_2 exsolution, oil swelling, viscosity reduction, and decreased interfacial tension.[259,260] During depressurization, supersaturated CO_2 separates from the oil phase, forming bubbles that expand and migrate, thereby displacing oil and improving recovery efficiency.

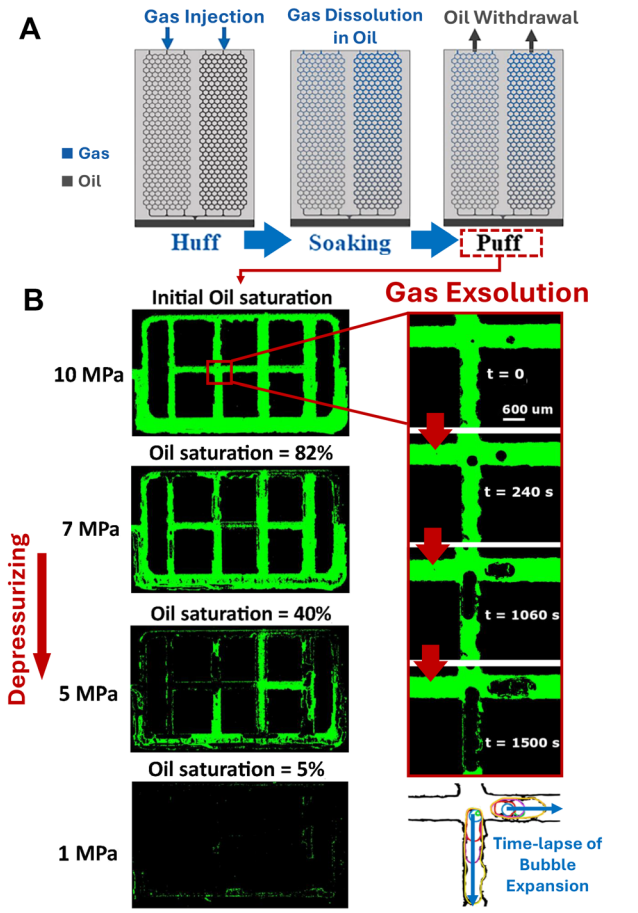

Fig. 11 Microfluidic investigations of the CO_2 huff-n-puff process. (A) A schematic illustration of the huff-n-puff process in a microfluidic device (adapted with permission from Guo *et al.*[212] Copyright © 2022 Elsevier). (B) Left: Fluorescent imaging showing 95% oil recovery after depressurization. Right: Gas exsolution during depressurization, including CO_2 bubble nucleation and growth (adapted with permission from Nguyen *et al.*[213] Copyright © 2018 Elsevier).

3.3.1 Gas exsolution. During the production stage, depressurization triggers gas exsolution, where previously dissolved CO_2 separates from the oil phase. As pressure decreases, CO_2 becomes supersaturated in the oil, separating, expanding, and migrating to displace the oil, further enhancing recovery efficiency.[259,260] Microfluidic experiments have provided valuable insights into the gas exsolution phenomena, as shown in Fig. 11A, replicating the huff-n-puff process in three stages: 1) high-pressure injection, 2) a

soaking period for gas dissolution, and 3) depressurization.[212,213] Nguyen *et al.*[213] compared CO_2 and N_2 huff-n-puff in glass micromodels at 10 MPa and 50 °C, demonstrating that miscible CO_2 achieved over 90% oil recovery, compared to 40% for immiscible N_2.[213] Miscibility and solubility are hence critical to the huff-n-puff efficiency.[213] Microfluidic fluorescent imaging revealed CO_2 bubble nucleation, growth, coalescence, and expansion as the primary recovery mechanisms (Fig. 11B). Even in immiscible CO_2 huff-n-puff, exsolution and bubble expansion remained the driving forces, achieving 73% oil recovery at 6 MPa and 110 °C.[215]

3.3.2 Effect of depressurizing rate and temperature. Rapid depressurization enhances miscible CO_2 huff-n-puff efficiency by maintaining higher levels of CO_2 supersaturation, which promotes bubble nucleation and growth.[212,215] Additionally, microfluidic studies on CO_2 exsolution suggest that lower temperatures can further enhance bubble nucleation.[214] At lower temperatures, reduced diffusion leads to higher CO_2 supersaturation, resulting in more effective gas exsolution.[214] Xu *et al.*[214] observed nucleation occurring preferentially at fluid–solid interfaces, where the energy barrier is lower.[214] Although the exsolved bubble nuclei form at random locations within the microfluidics, CO_2 bubbles preferentially grow in the pore bodies rather than in the throats due to capillary pressure constraints.[214] This differential distribution of exsolved CO_2 bubbles within the pore space (bodies *vs.* throats) may contribute to capillary trapping for CO_2 geological storage during the huff-n-puff process.

3.3.3 Presence of water. The presence of water in the reservoir, often due to previous waterflooding, also plays a critical role in the huff-n-puff process.[216] Microfluidic studies by Huang *et al.*[216] revealed that water trapped between CO_2 and oil phases increases capillary pressure, which can hinder bubble coalescence and migration.[216] This, in turn, increases residual CO_2 saturation, improving both oil recovery and CO_2 storage efficiency.[216]

3.3.4 Effect of nanoconfinement. Micro- and nanofluidics have also shed light on the effects of nanoconfinement during the huff-n-puff process.[25,217] In nanometer-scale channels, high capillary pressures between CO_2 and oil result in lower oil-phase pressure under the same CO_2 injection conditions.[25,217] This reduced oil pressure decreases CO_2 solubility in the oil, leading to lower CO_2 saturation levels.[25,217] To compensate, a higher depressurization rate is required to overcome diffusion limitations and achieve effective oil recovery.[25,217] These findings highlight the importance of carefully considering nanoconfinement effects when applying the huff-n-puff technique in fractured tight reservoirs.

Future research could leverage microfluidics to investigate key factors influencing CO_2 huff-n-puff performance, such as cycle number, soaking time, oil composition, and injection strategy.[256] Further integration of microfluidics with techniques like particle image velocimetry (PIV) and spectroscopy could provide deeper insights into CO_2 dissolution, multiphase flow, and oil displacement, offering advancements beyond the traditional core flooding methods.

Moreover, challenges such as asphaltene precipitation during CO_2 huff-n-puff require further investigation using microfluidic visualization. Addressing these challenges is essential for optimizing CO_2-EOR and ensuring long-term reservoir performance.

3.4 Foam-assisted CO_2-EOR

Foam is injected into subsurface porous media for various applications, including EOR,[7,59,80,155,261,262] soil or aquifer contamination remediation (*e.g.*, nonaqueous phase liquid removal),[113,263–266] carbon capture, storage and sequestration,[2,218,267,268] and hydraulic fracturing.[269–271] Driven by EOR performance, the traditional and most prevalent method for studying CO_2 foam flooding at the laboratory scale involves core flooding, where fluid is flooded through natural rock samples.[272–276] This approach has provided insights into various EOR processes.[272,274,277,278] Alternative visual experiments were conducted in Hele-Shaw cells, either empty,[219,279,280] filled with glass beads,[281,282] or patterned,[119,283] simulating the porous media environment. These cells facilitate the visualization of foam–oil interactions and displacement dynamics. Moreover, some researchers have turned to advanced imaging techniques, such as computed tomography (CT)[284–287] and nuclear magnetic resonance (NMR),[288,289] to trace fluid flow and saturation distributions within rock samples.

Foam substitutes conventional flooding fluids such as water,[290,291] chemicals (*e.g.*, surfactants and nanoparticles),[292,293] and gas[218] to mitigate the challenges of early breakthrough and low sweep efficiency originating from the low viscosity and density of these conventional fluids. Moreover, foam injection can improve the preferential flow challenge caused by heterogeneity—primarily permeability contrast—of underground porous formations. In general, foam, with increased viscosity and density, is a beneficial option as it controls the mobility of the injected fluids to suppress viscous fingering, gravity override, and preferential flow (Fig. 12A).[27,272,279] The mobility ratio (M_R) is crucial in reflecting the importance of mobility control in EOR, expressed as:

$$M_R = \frac{\text{Mobility of the injected fluid}}{\text{Mobility of the residing fluid}} = \frac{K_{r,I}/\mu_I}{K_{r,R}/\mu_R}, \quad (2)$$

where $K_{r,I}$ and $K_{r,R}$ are the relative permeabilities of the injected and residing fluids, respectively; μ_I and μ_R represent the viscosities of the injected and residing fluids, respectively.

A desirable injection process provides M_R values smaller than unity, indicating that the mobility of the injected fluid is sufficiently reduced and lower than that of the residing one, either through smaller $K_{r,I}$ or higher

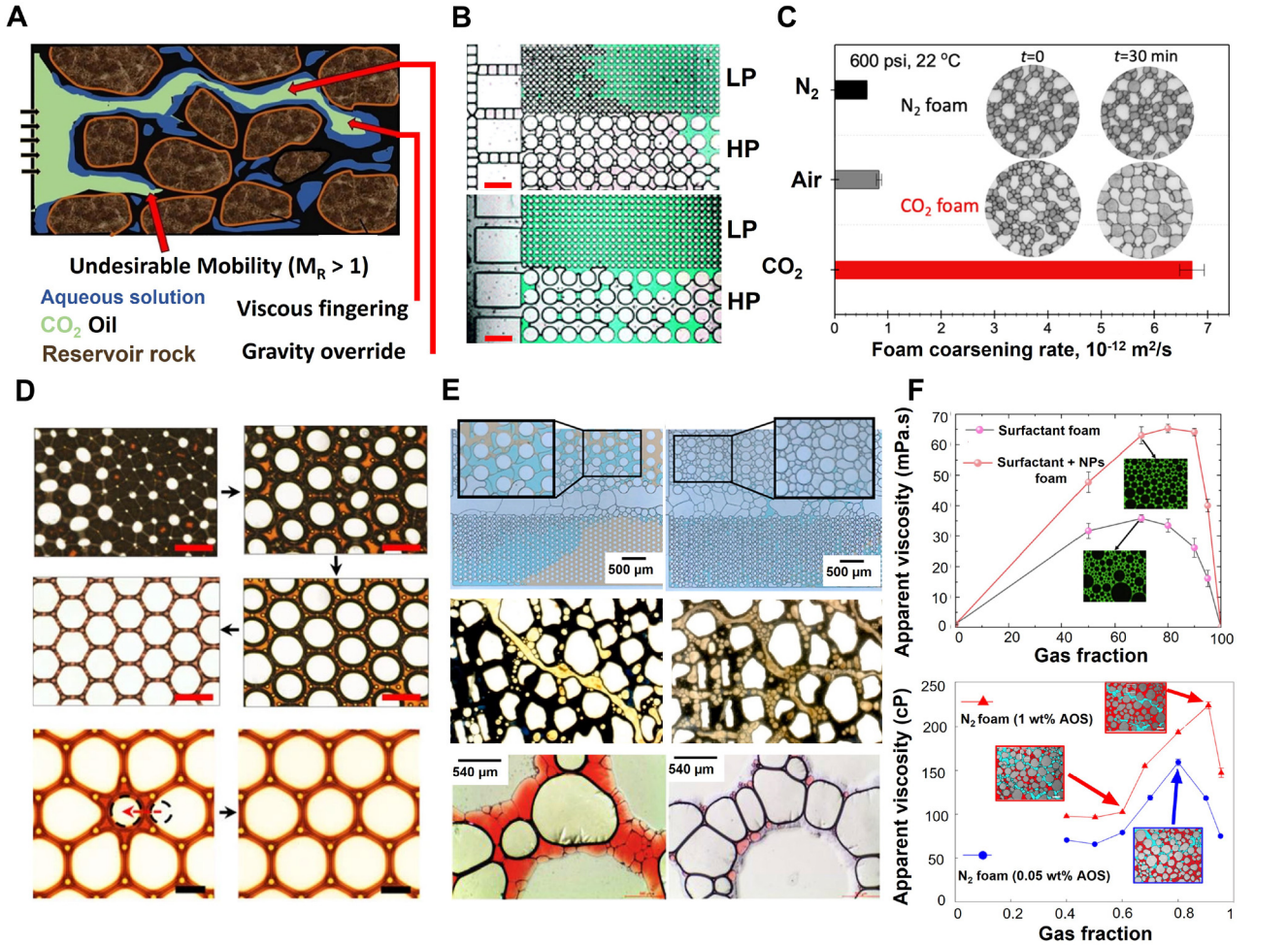

Fig. 12 Microfluidic results for foam flow and stability in porous media: (A) challenges with CO_2 gas injection into subsurface porous media include gas override due to buoyancy and viscous fingering due to its low viscosity, *i.e.*, higher mobility compared to the residing oil phase (M_R > 1) (adapted from Pal *et al.*[294] under CC-BY License). (B) Fluid–fluid displacement in heterogeneous PDMS porous media, comparing (top) foam and (bottom) gas injection effects on water (shown in green) displacement in high and low permeability zones. Foam lamellae block the (lower layer) high-permeability zone, allowing fluid displacement to the (upper layer) low-permeability zone. However, gas injection leads to viscous fingering in the high-permeability zone and early breakthrough (the scale bars are 500 μm; adapted with permission from Ma *et al.*[80] Copyright © 2012 the Royal Society of Chemistry). (C) Effect of gas solubility and diffusivity on the foam coarsening rates of air, N_2, and CO_2 foams at 600 psi and 22 °C (adapted from Yu *et al.*[295] under CC-BY-NC-ND License). (D) Foam coarsening dynamics by Ostwald ripening (top 4 images), where gas diffuses from smaller to larger bubbles, and reverse Ostwald ripening (bottom 2 images), where the opposite occurs (with top and bottom scale bars of 100 μm and 50 μm, respectively; adapted from Huang *et al.*[296] under CC-BY License). (E) Displacement of crude oil (brown) by foam in a heterogeneous porous medium. Foam coalescence and surfactant adsorption on the surface altered the wettability from hydrophobic to hydrophilic. Foam bubbles exhibited greater stability in the absence of oil (top; adapted with permission from Xiao *et al.*[81] Copyright © 2018 American Chemical Society). Displacement of crude oil (black) by foam in a glass microfluidic chip. The addition of silica nanoparticles improved foam stability by reducing bubble coarsening (right), compared to the formation of large gas slugs when using only a surfactant (left) (middle; adapted with permission from Zhao *et al.*[297] Copyright © 2021 Elsevier). The interaction of foam bubbles with paraffin oil (red) in a glass-etched microfluidic chip, shown without (left) and with (right) the use of silica nanoparticles (bottom; adapted with permission from Yekeen *et al.*[298] Copyright © 2017 Elsevier). (F) Effects of gas ratio (or foam quality) and additives (nanoparticles and surfactants) on foam's apparent viscosity, highlighting the stabilization by nanoparticles and the influence of surfactant concentration (top figure adapted with permission from Lv *et al.*[123] Copyright © 2022 Elsevier and bottom figure adapted with permission from Wang *et al.*[299] Copyright © 2025 American Chemical Society).

μ_I. Strictly speaking in EOR, the feasibility of using a well-established method of CO_2 gas injection is limited to the production of light hydrocarbons, which contribute to only 30% of the global reserves.[300] In addition, CO_2 injection to recover heavy (unconventional) hydrocarbons results in M_R > 1 since the viscosity of CO_2 gas is considerably lower than the residing hydrocarbons in subsurface layers.[301–303] Foam plays a crucial role in EOR and provides an effective solution for the latter scenario by increasing the viscosity of the displacing fluid. This increase is achieved by trapping gas within the liquid lamellae, forming a foam structure that impedes fluid flow. The additional viscosity introduced by the foam may be conceptualized as:[304–306]

$$\mu_{\text{foam}} = \mu_{\text{gas}} + \frac{\alpha(\text{number density of lamellae})}{(\text{interstitial gas velocity})^{c}}, \quad (3)$$

where α and c are constants that characterize the contribution of the trapped gas to the overall viscosity of the foam. This mechanism is critical for enhancing EOR efficiency by reducing the mobility of the injected fluid, thereby better controlling the fluid flow in the reservoir.

The additional viscosity has been attributed to the interfacial viscosity between the foam bubbles[307,308] and the confinement of the bubbles moving through the capillary pores.[272,306] Some visual studies have reported local foam trapping in the high-permeable regions, effectively redirecting subsequent bubbles toward areas with lower permeability.[59,80,287,309–311] Local pore blockage redirects foam to less resistant pathways, leading to the formation of permanent or temporary preferential flow paths.[119,218,312–314]

Microfluidic devices have been utilized to investigate foam characterization and oil displacement by foam under diverse operational conditions.[59,212,218,295,313,315] Huh *et al.*[316]'s study was among the early attempts to visualize foam flow in a microfluidic device, showing increased bubble generation in heterogeneous structures.[316] Not until the last decade was soft lithography utilized to study foam-EOR in microfluidic porous media. Ma *et al.*[80] fabricated their mold with maskless photolithography and then bonded the PDMS stamps to PDMS-coated glass slabs to provide uniform wettability.[80] They noted that air foam could effectively block the highly-permeable areas, thus redirecting bubble flow towards less-permeable zones. In general, dry foams controlled the mobility and delayed the breakthrough time (up to 11.20 s), while pure air injection accelerated it (to 0.03 s) due to significant viscous fingering (Fig. 12B).

3.4.1 Foam stability. The ongoing developments in MEMS and soft lithography technologies have motivated more foam-assisted EOR investigations in both hard and soft microfluidic systems. A major area of focus is the characterization and screening of the operational conditions and foam components to improve the stability of the foam bubbles in the presence of oil. This includes selecting appropriate types and concentrations of foaming agents,[123,155,220,297,298,317–321] such as surfactants, nanoparticles, and polymers, beside the composition of oil,[297,298] the pressure and temperature of the porous media,[295,322] the gas type,[295,312] and the brine chemistry.[220,298]

Foam coarsening and stability. Yu *et al.*[295] explored the coarsening rate of static foam bubbles within a glass microfluidic chip, revealing that foam coarsens with reduced surfactant concentration, increased gas fraction, higher gas solubility in the liquid phase (Fig. 12C), elevated temperatures, and greater molar volume of the dispersed (gas) phase.[295] Huang *et al.*[296] utilized structured silicon substrates fabricated by direct laser writing and DRIE[296] to study bubble patterns affected by coarsening dynamics. They created various bubble patterns by adjusting the number and spacing of the microfluidic pillars. These patterns emerged as a result of regular coarsening, reverse coarsening at bubble-pillar contact edges, and bubble aggregation in larger domains (Fig. 12D). They found that the gas volume fraction played a critical role in bubble patterning, with higher gas availability enhancing bubble stability during the coarsening process. Benali *et al.*[314] etched a heterogeneous design of a porous medium on a silicon wafer (down to 30 μm by the DRIE technique). Their temporal image analysis revealed that although bubble regeneration and refinement in porous media can increase their number density, foam decay mechanisms through coarsening may dominate the generation rate and lower the foam density. Adding silica nanoparticles did not significantly influence the foam generation and decay rates.

Guo and Aryana, using a wet-etched glass micro-model, found that while some surfactants can generate greater foam volumes favorable for EOR, formulations with better stability and lower chemical usage are often more desirable.[323] They also proposed mixing CO_2 with N_2 to reduce gas diffusion through foam lamella,[324] thus improving the foam stability and enabling foam propagation into a larger area of the medium with more gas trapping, as a desirable scenario for CCUS purposes. Moreover, foam injection is increasingly being combined with other EOR methods, such as steam assisted gravity drainage (SAGD)[317] or surfactant flooding,[292] to improve fluid propagation in porous media. This integration requires careful screening and optimization of foam formulations to achieve stable bubbles under the desired conditions.

Effect of oil. A persistent challenge in using foam for oil displacement is the destabilizing effect of oil on foam lamellae.[81,155,281,298,325,326] Xiao *et al.*[81] observed N_2 bubble coalescence at the foam–oil interface, attributed to imbalanced interfacial capillary tensions resulting in positive entry and spreading coefficients, which explained the disruption of foam lamellae by oil.[81] This coalescence released surfactant, which subsequently adsorbed onto the surface of the microfluidic porous medium, altering wettability and ultimately enhancing foam stability. The authors reported that oil recovery using N_2 foam was significantly higher compared to displacement processes with single-phase fluids (Fig. 12E-top). Nanoparticles, primarily silica nanoparticles, were found to markedly enhance the stability of foam bubbles in the presence of oil (-Fig. 12E-middle and bottom and F-top).[155,297,323,327–329] By adsorbing at the gas–liquid interface, nanoparticles help mitigate foam decay mechanisms, such as liquid drainage, film rupture, and gas diffusion (coarsening).[330–332]

3.4.2 Entrapment and viscosity. Gas trapping and foam viscosity play a crucial role in sweep efficiency and oil displacement, both of which are strongly influenced by morphology of foams. The bubbles' morphology, in turn, is influenced by various factors, with pore size distribution, gas fraction, foaming agents, and decay rate being the most significant contributors.[27,333–336]

The relationship between bubble size (gas fraction) and apparent viscosity has yielded inconsistent findings in the literature. Several studies have reported a direct correlation, where larger bubbles are associated with increased viscosity, resulting in improved fluid diversion and expanded foam propagation in porous media.[80,219,220,318,336,337] However, other studies have revealed contrasting findings, observing a decrease in foam viscosity at higher gas fractions.[338,339]

The apparent viscosity of foams is typically estimated using pressure gradient measurements combined with fluid flow equations for porous media, such as the Hagen–Poiseuille or Darcy's equations.[280,281,336,340] Experimental results show that the pressure gradient generated by foam in porous media is influenced by various parameters, in addition to gas type, such as lamella density,[312,340] and foam total velocity.[280,336,341] For instance, some studies have reported that depending on the foam's gas fraction, the

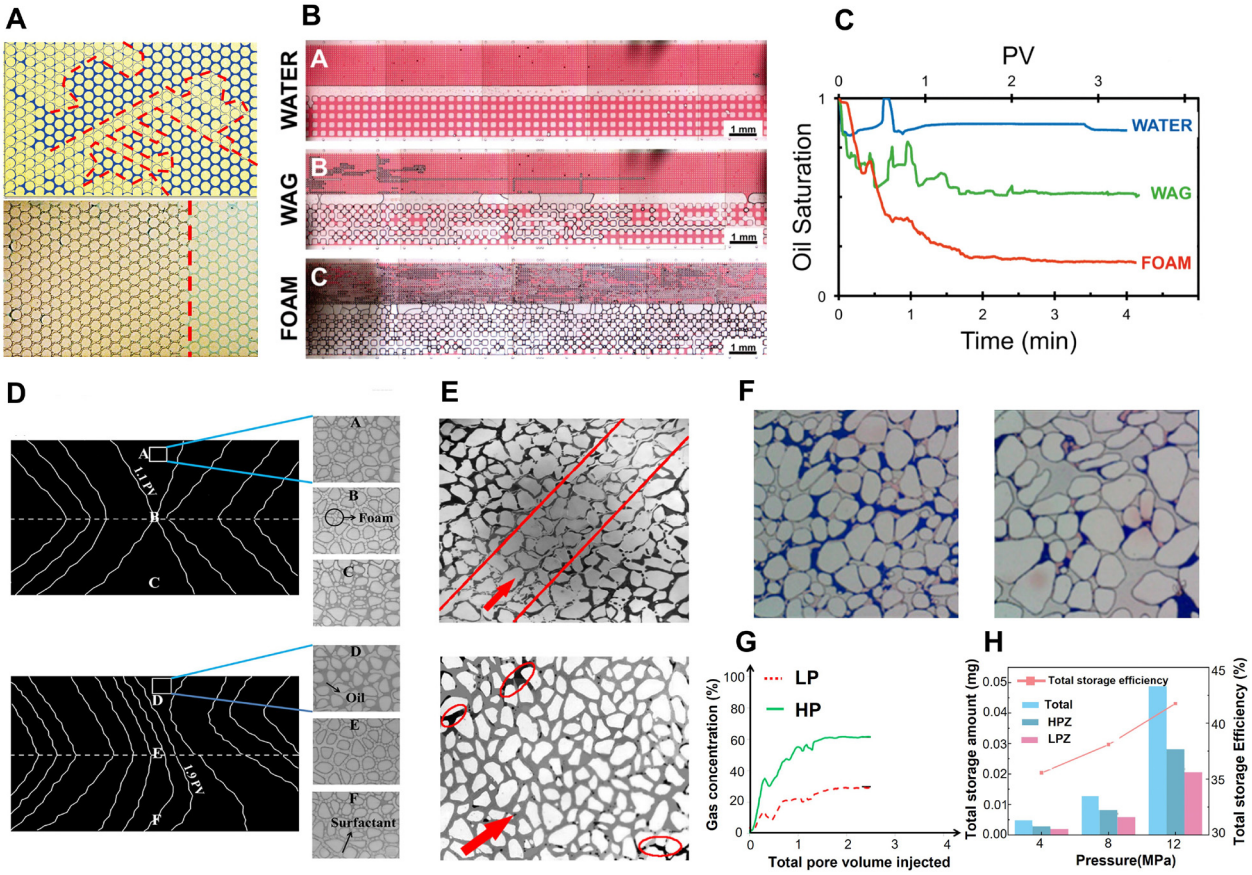

Fig. 13 Summary of displacement dynamics by foam in microfluidic models: (A) saline water displacement by CO_2 gas (yellow) showing viscous fingering (top) and by CO_2 foam with a stabilized front (bottom) at the flow rate of 100 μL min^{-1} in a quartz-etched porous medium (adapted with permission from Zheng *et al.*[218] Copyright © 2017 John Wiley & Sons). (B) Paraffin oil displacement by water, water alternating gas (WAG), and foam in a heterogeneous multi-layer microfluidic (PDMS) porous medium, demonstrating foam's superior oil recovery efficiency in all regions compared to water and WAG shown in (C) (adapted from Conn *et al.*[59] under CC-BY License). (D) Isopar V oil displacement by foam in 3D printed porous media placed horizontally (top) and vertically (bottom) to examine gravity effects on displacement patterns, highlighting gravity's impact on front propagation. In horizontal mode, gravity's impact is minimal, creating symmetrical fronts. In vertical mode, gravity override speeds up propagation in the lower region, leading to S-shaped fronts due to higher liquid saturation (adapted from Shojaei *et al.*[349] under CC-BY License). (E) Oil (black) displacement by water (top) and foam (bottom) in heterogeneous (glass-etched) media, showing foam's ability to mitigate fluid channeling and improve oil sweep efficiency (adapted with permission from Sun *et al.*[350] Copyright © 2014 American Chemical Society). (F) Residual oil (pink) after water then foam injection into heterogeneous porous media with (left) low and (right) high permeability that were laser-etched on glass substrates. Foam displaced the residual oil remaining after water flooding and reached over 90% oil recovery in both cases. Larger pore and throat sizes of the high permeable structure allowed higher gas saturation (adapted with permission from Wang *et al.*[311] Copyright © 2021 American Chemical Society). (G) Gas saturation *vs.* time (injected pore volume) during oil displacement by foam in a heterogeneous porous medium with two high and low permeable layers fabricated on a UV curable epoxy (NOA 81). Gas saturation is higher in the more permeable region due to greater opposing capillary pressures that prevent non-wetting gas from entering less permeable areas (adapted with permission from Xiao *et al.*[81] Copyright © 2018 American Chemical Society). (H) Gas storage *vs.* gas-injection pressure during oil displacement by gas in a heterogeneous (glass-etched) porous medium with high (HPZ) and low (LPZ) permeable zones. Higher pressures improved gas storage by overcoming capillary resistance, allowing greater gas saturation in more permeable areas (adapted with permission from Qian *et al.*[196] Copyright © 2025 Elsevier).

pressure gradient increases under gas-rate-independent or liquid-rate-independent flow regimes.[341,342] In the gas-rate-independent flow regime, the foam reaches a critical capillary pressure beyond which foam coalescence reduces lamella density, leading to a decrease in foam viscosity (Fig. 12F).

Overall, the understanding and prediction of foam transport properties, particularly foam viscosity in porous media, are complicated and constrained by a wide range of interconnected variables. A recent study by Wang *et al.*[299] using a soft microfluidic chip (Norland Optical Adhesives 81) explored how variations in foam's gas fraction influenced key parameters, such as gas fraction, lamella density, bubble size, and apparent viscosity.[299] Their findings indicated that these parameters typically increase with the foam's gas fraction until reaching a threshold, beyond which they decline due to insufficient surfactant concentration leading to unstable liquid lamellae (Fig. 12F-bottom). They also observed that the mobility of smaller bubbles in the range of pore size distribution is the key to predicting the foam viscosity variation.

3.4.3 Fluid displacement. Microfluidic experiments on fluid–fluid displacement (*e.g.*, water displaced by foam/oil/CO_2 gas, oil displaced by water) have been performed to identify the required conditions to achieve stable and favorable displacement fronts, while minimizing the formation of viscous and capillary fingering.[80,343–345] However, the pore-scale dynamics of aqueous or oil-based fluids displaced by foam remain less explored due to the complexity of foam behavior in multiphase porous media. Foam flow in porous media differs significantly from bulk foam flow because the bubbles are confined by micro- or nano-scale pore structures, which are influenced by factors, such as permeability, heterogeneity, connectivity, and wettability[346,347] and controlled by viscous, capillary, and gravity forces.[348]

In a comprehensive study, Zheng *et al.*[218] utilized a high pressure-high temperature microfluidic chip to visualize the displacement of brine by CO_2 in various phases: gas, liquid, supercritical, and foam. They mapped different displacement-pattern regimes on a phase diagram depending on the corresponding capillary number and viscosity ratio (discussed in section 4.1). Their results indicated that foam injection was the only method that consistently resulted in "stable displacement", while the other CO_2 fluids penetrated the residing brine and caused viscous fingering (Fig. 13A).[218] Similarly, Ma *et al.*[80] observed that air foam in a PDMS dual-layered chip with a permeability contrast of four enhanced water displacement more effectively than gas due to reduced breakthrough times in high permeability zones (Fig. 12B).

Shojaei *et al.*[349] investigated *in situ* generated foam for displacing oil in a 3D printed (acrylic oligomer) heterogeneous (vertically oriented) porous medium, showing effective oil recovery despite gravity-induced phase segregation (Fig. 13D). The efficiency of oil recovery and gas saturation in the porous medium depended on the fluids' injection flow rates. While elevated flow rates promoted foam generation and increased lamellae density, they also led to the inevitable consequence of viscous fingering.

Comparative analysis of foam and other fluids. Conn *et al.*[59] investigated the performance of water flooding, water alternating gas (WAG), and N_2 foam flooding in a hydrophobic heterogeneous PDMS microfluidic chip. Their findings revealed a significantly higher silicone oil recovery of 75% and improved sweep efficiency during foam injection, attributed to the ability of foam bubbles to control mobility within fractures and high permeability regions, enabling more effective oil displacement in low permeability zones (Fig. 13B and C). Sun *et al.*[350] compared crude oil displacement by different injection fluids in their glass micro model fabricated by photochemical etching. They reported that water failed to sweep oil effectively due to its high mobility relative to the oil phase (Fig. 13E-top). In contrast, oil recovery increased to 77% with the injection of surfactant foam owing to mobility reduction. Surfactant-nanoparticle foam achieved even higher oil recovery (94%, Fig. 13E-top) by enhancing the viscoelasticity and stability of foam lamellae. Their sand-pack experiments confirmed this trend, demonstrating similar recovery patterns for water and foam injections.

Additionally, Zheng *et al.*[218] demonstrated that the increased viscosity of CO_2 foam, in a homogeneous quartz device, significantly improved the stability of water displacement, leading to minimal residual water and 68% CO_2 storage. In contrast, using CO_2 gas gave rise to the formation of capillary and viscous fingering, higher residual water saturation, and a reduced CO_2 storage of 56%.[218] These results were consistent with the findings by Guo *et al.*[351] who used SEM images and photolithography to obtain and replicate a 2D heterogeneous structural network of a rock sample on a borosilicate substrate with a porosity of 45% and permeability of 15 mD. Foam injection outperformed gas and water injections to improve recovery factors for water and oil displacements by 34% and 33%, respectively.[351,352]

In certain cases, foam is injected as a complementary agent to address high residual oil saturation after water[155,292,327,328,350,352,353] or solvent[292,354] injection. Foam can penetrate previously unswept zones to mobilize trapped or bypassed oil and enhance recovery.

Effect of heterogeneity. In heterogeneous porous media, the non-wetting gas phase preferentially flows through high permeability pathways with minimal resistance, leaving low permeability regions unswept[59,315,353] (Fig. 12C-bottom). Foam application can mitigate this by reducing fluid mobility in the high permeability paths (by pore blocking) and diverting the flow toward low permeable regions, thereby enhancing the overall swept area and improved oil recovery outcomes (Fig. 12C-top).[59,288,313,353,355–357]

The dynamics of foam flow in porous media are influenced by the pore structure and surface properties. Preferential flow paths emerge during foam flow due to heterogeneity caused by permeability contrasts. Foam tends to flow more easily through high-permeability pathways,

while in the most resistant regions with maximum capillary pressure, foam trapping occurs.[314] However, pore blockage and the formation of preferential flow paths are not limited to heterogeneous media. Lv *et al.*[312] observed that in a homogeneous pore structure, pore blockage occurred due to gas trapping, causing foam to flow through unblocked pathways.[312]

In hydrophilic heterogeneous microfluidic chips, several fluid-displacement studies observed higher gas saturation in high permeability regions, while low permeability zones remained predominantly filled with aqueous liquid (Fig. 13F–H).[80,81,311,352,353,358] This is because capillary pressure is a driving force for the wetting liquid phase but an opposing force for the non-wetting gas phase. Thereby, when gas cannot overcome the limiting capillary force in the low permeability area, it is redirected toward the high permeability regions.[81]

3.5 Multiscale comparison of EOR efficacy

Geometry, wettability, and heterogeneity of chip models can significantly alter measured recovery factors (RF), often leading to substantial variation in reported efficacy.[359] As commonly reported in the literature, the recovery process of oil in reservoirs is often approximately 20%, 15%, and 15% during primary, secondary, and tertiary recoveries, respectively.[360–362] The field results suggest that proper selection of EOR methods is necessary for the success of oil production.

Taking advantage of the reproducibility of microfluidics technology, alterations in EOR methods from thermal (*e.g.*, hot water, cyclic vapor), gaseous (*e.g.*, miscible CO_2), chemical (*e.g.*, nanoparticles, surfactant), to others (*e.g.*, microbiological) has been conducted by researchers.[361–365] Behera *et al.*[363] developed a novel nanofluid (SMART LowSal), formulated in low salinity seawater containing anionic surfactant, polymer, and low concentration of silica nanoparticles, that was capable of increasing the recovery rate by an additional 20–30% during microfluidic experiments. Observations indicated that the injected nanofluids significantly lowered the fluid–fluid interfacial tension causing the oil droplets to be elongated, and modified the grain–fluid wettability. However, such nanofluids only demonstrated an increase of 5–6% after chemical flooding in the sand-pack reactor and Amott cell.[363] An alternative study with CuO + PVA + surfactant nanofluid by Tuok *et al.*[365] achieved a RF of 72% when conducting the experiment in a microfluidic matrix. Meanwhile, Zhu *et al.*[364] demonstrated that 12 hours of soaking of pre-injected CO_2 foam followed by foam flooding recovered, in general, almost 57% of crude oil originally in place. Although this foam flooding technique is considered a major improvement to water flooding (~30%),[364] the core flooding results are still far off from the ones observed in microfluidic studies and are still higher than the globally reported average RF of 20–40% in reservoirs,[360–362] as shown in Table 2.

Table 2 Ranges of recovery factor (RF) in enhanced oil recovery from pore-scale to Darcy-scale reported in the literature[278,359–369]

Microfluidics	Core flooding	Field reservoir
0.5–0.8	0.3–0.6	0.2–0.4

The reduction in recovery factor from microfluidic experiments, to the core flooding test, to the reservoir scale indicates the existence of a multi-scale discrepancy in EOR. Though microfluidics remains indispensable for high-resolution visualization of pore-scale phenomena at low environmental impact, direct translation of RF from chip to field without correction can lead to overly optimistic projections. The literature increasingly recommends a tiered approach, where microfluidic data informs chemical formulation and injection strategy, followed by upscaling through core flooding, and final validation in pilot tests to account for scale-dependent physics, reservoir heterogeneity, and operational limitations.[359,366,367]

4 Microfluidic investigations on CO_2 sequestration in saline aquifers

Carbon storage in deep saline aquifers involves multiple trapping mechanisms, as illustrated in Fig. 14A, which are important for long-term CO_2 sequestration.[370,371] Upon CO_2 injection, buoyancy drives the CO_2 plume upwards, where it becomes structurally trapped beneath impermeable cap rocks in the sedimentary basin.[370,371] Structural trapping plays an important role shortly after injection.[371] Subsequently, residual (capillary) trapping occurs when CO_2 is trapped in pore spaces due to capillary forces.[371] Over longer timescales, solubility and mineral trapping provide more secure storage.[371] In solubility trapping, CO_2 gradually dissolves into brine, a process initially driven by diffusion at the CO_2/brine interface and significantly enhanced by convective mixing.[370,371] In mineral trapping, CO_2-acidified brine may react with minerals, such as calcium, to form solid carbonates, effectively trapping CO_2 in mineral form.[371]

Among these trapping mechanisms, microfluidics has been primarily used to study capillary and solubility trapping due to its ability to visualize pore-scale fluid dynamics, with limited research on structural and mineral trapping. The micron-scale dimensions of microfluidic devices do not adequately replicate geological features, such as cap rocks or large fractures necessary for structural trapping. Additionally, microfluidic studies on mineral trapping are scarce,[372–374] as the silicon or glass substrates commonly used fail to capture the complexity of reservoir rock structures and mineral compositions.[375] Furthermore, the slow kinetics of mineralization, relevant on geological timescales, exceed the typical temporal scope of short-term microfluidic experiments.[371,376]

In contrast, microfluidics is particularly effective for studying pore-scale fluid dynamics relevant to capillary and

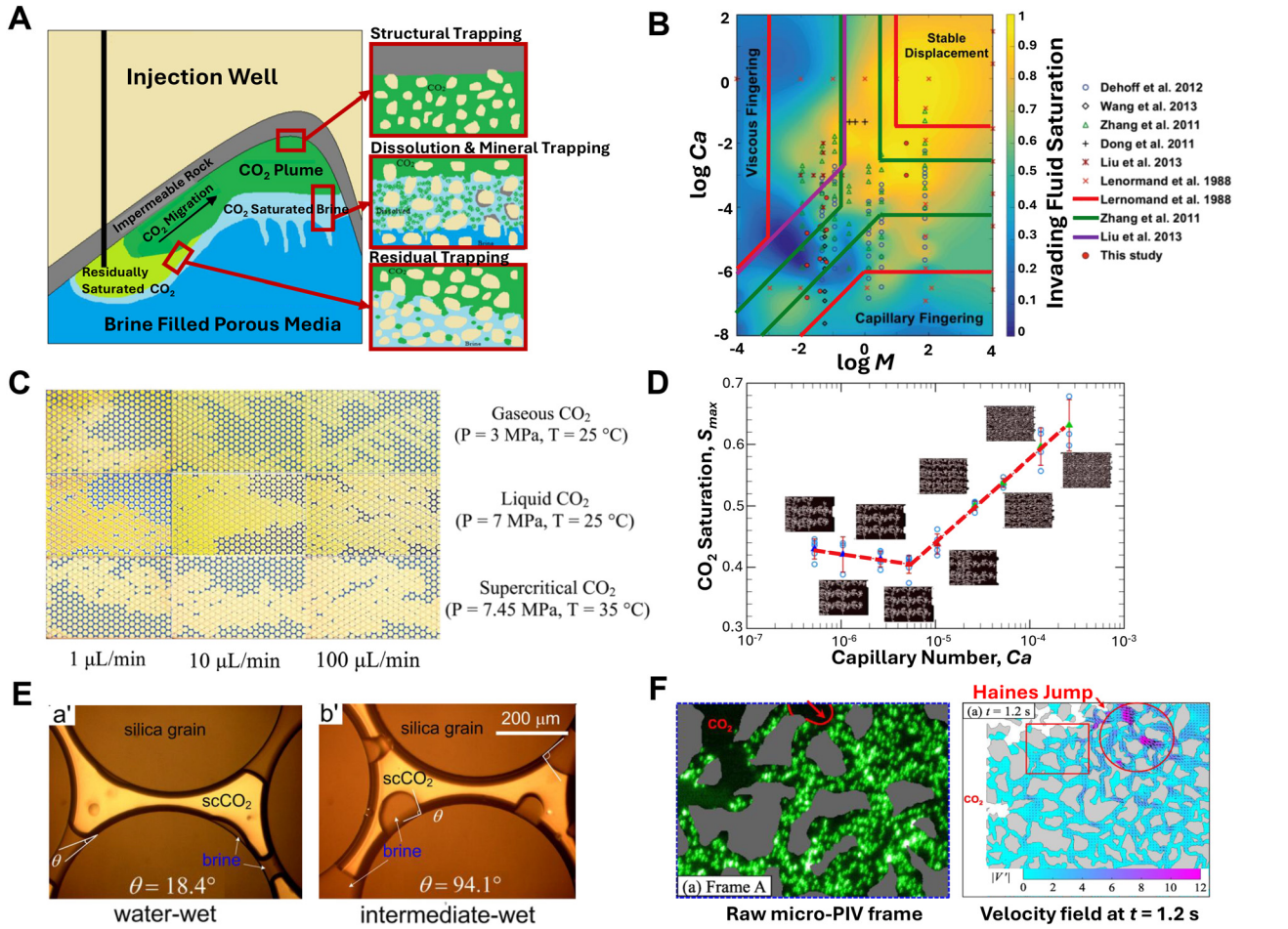

Fig. 14 Microfluidic investigations of CO_2 trapping mechanisms in saline aquifers for CCS applications. (A) Schematic representation of CO_2 trapping mechanisms in porous media, including structural, residual, and dissolution/mineral trapping (adapted with permission from Elryes *et al.*[396] Copyright © 2024 American Chemical Society). (B) Phase diagram of fluid displacement regimes (capillary fingering, viscous fingering, stable displacement) as a function of capillary number (Ca) and viscosity ratio (M) (adapted with permission from Zheng *et al.*[218] Copyright © 2017 American Geophysical Union). (C) Microfluidic visualization of CO_2 displacement in porous media under different flow rates (1, 10, 100 μL min^{-1}) and CO_2 phase states (gaseous, liquid, supercritical) (adapted with permission from Zheng *et al.*[218]). (D) Effect of Ca on maximum CO_2 saturation (S_{max}), highlighting the crossover regime where saturation is minimized (adapted with permission from Li *et al.*[395] Copyright © 2019 American Geophysical Union). (E) Wettability effect on CO_2 trapping in water-wet (a') and intermediate-wet (b') micromodels (adapted with permission from Hu *et al.*[378] Copyright © 2017 American Geophysical Union). (F) Micro-PIV analysis of CO_2 invasion dynamics in porous media, showing raw imaging data and velocity field measurements, with velocity bursts during "Haines jumps" indicated (adapted with permission from Li *et al.*[397] Copyright © 2017 American Geophysical Union).

solubility trapping. Recent microfluidic studies have provided critical insights into displacement patterns,[377–379] dissolution kinetics in quasi-2D porous media,[380–383] and key properties such as solubility,[384] diffusivity,[83] and mass transfer coefficients.[84,96,99,100,385–389] The following section reviews how microfluidic studies contribute to understanding CO_2 capillary (section 4.1) and solubility trapping mechanisms (section 4.2), as well as the associated salt precipitation processes (section 4.3), in CCS within deep saline aquifers. By offering a detailed understanding of the critical parameters affecting CO_2 underground trapping, microfluidic research contributes to optimizing CCS processes, maximizing CO_2 storage capacity while mitigating the adverse effects of salt precipitation in deep saline aquifers.

4.1 CO_2 capillary trapping

Capillary trapping, also termed residual trapping, is a critical mechanism in CO_2 sequestration where CO_2, injected into brine-saturated porous media, is trapped when capillary forces exceeding buoyancy forces, leading to high CO_2 saturation levels.[376] Capillary trapping strongly depends on the efficiency of CO_2–brine displacement in porous media, which controls the amount of CO_2 immobilized in the porous network through the interplay between capillary and viscous forces.[376] Similar to other two-phase immiscible flows in porous media, CO_2–brine displacement is strongly influenced by parameters such as the viscosity ratio ($M = \mu_{CO_2}/\mu_b$) between CO_2 and brine, capillary number ($Ca = \mu V/\sigma$), and surface wettability.[18,390–393] Depending on M and Ca, fluid

displacement follows distinct flow regimes, including viscous fingering (low M, high Ca), capillary fingering (low Ca), stable displacement (high M, high Ca), or transitions between these regimes.[23,218,377,378,383,394,395] These flow regimes are often visualized using phase diagrams, as seen in Fig. 14B.

Microfluidic techniques have been employed to systematically investigate CO_2 capillary trapping and displacement patterns under high-pressure conditions relevant to CCS operations.[23,218,378,383,394,395] Visualizations show that CO_2 injection into brine-filled porous media results in capillary or viscous fingering, depending on Ca.[23,218,378,383,394,395] Viscous fingering occurs when a low-viscosity fluid displaces a higher-viscosity fluid, leading to interfacial instability that generates finger-like patterns.[398] In contrast, capillary fingering occurs at low Ca, where the capillary force dominates over viscous force, forming narrow and irregular pathways.[18,390] Since CO_2 generally has a lower viscosity than water or brine (whether in gas, liquid, or supercritical state), achieving stable displacement is challenging due to the unfavorable viscosity ratio. Intermediate Ca often leads to a crossover between the two.[23,218,378,383,394,395] Zheng *et al.*[218] demonstrated that liquid CO_2, with its higher viscosity, achieves better displacement efficiency than gas or supercritical CO_2 under the same injection rates (seen in Fig. 14C).[218]

Studies by Li *et al.*[395] revealed a non-linear relationship between CO_2 saturation and the capillary number (Ca) across a broad range of Ca ($10^{-6.3}$–$10^{-3.6}$) (Fig. 14D).[395] CO_2 saturation decreases with increasing Ca in the capillary fingering regime but increases with Ca in the viscous fingering regime.[395] The lowest saturation occurs in the crossover region between these two regimes, indicating that avoiding this critical Ca range is essential for maximizing CO_2 trapping efficiency in CCS applications.[395]

To improve CO_2 trapping, researchers have proposed foam injection into saline aquifers.[218] Microfluidic experiments reveal that CO_2 foam stabilizes the displacement front by increasing the viscosity ratio (M), improving storage efficiency by 23–53% compared to pure CO_2 injection.[218] However, increasing brine salinity from 0 to 5 mol L^{-1} reduces displacement efficiency.[377] The adverse effect of brine salinity is attributed to higher brine viscosity and increased CO_2–brine interfacial tension, which decrease both the viscosity ratio (M) and the capillary number (Ca), ultimately lowering the trapping efficiency.[377]

The wettability of the porous media strongly affects capillary trapping.[378,399] Hu *et al.*[378] demonstrated that intermediate-wet micromodels (with an *in situ* contact angle, θ_{brine} = 94°) trapped 15% more CO_2 compared to water-wet micromodels (with θ_{brine} = 20°).[378] As shown in the pore-scale visualization in Fig. 14E, the lower CO_2 saturation in the water-wet micromodel was attributed to brine adhering to the solid surface, which reduced the pore space available for CO_2.[378] Image analysis revealed that the intermediate-wet micromodel exhibited a higher number of CO_2 clusters and a larger average cluster radius compared to the water-wet micromodel.[378] Wettability effects were found to be more pronounced at lower flow rates.[378] Moreover, pore-scale observations revealed that wettability can change during CO_2 injection due to CO_2 dissolution in brine, which lowers pH and increases the water contact angle on silica surfaces.[218,399]

Advanced optical methods, such as microscopic particle image velocimetry (micro-PIV), have improved the understanding of capillary trapping by providing detailed velocity fields in the aqueous phase near the CO_2 displacement front.[397,400,401] Experiments with homogeneous micromodels and porous rock replicas revealed "Haines jumps", which are rapid bursts of velocity during CO_2 finger formation, with speeds exceeding 20 times the bulk flow.[397,400] These sudden pore-filling events occur when a non-wetting fluid displaces a wetting fluid in porous media, causing abrupt changes in capillary pressure.[402] This dynamic promotes finger formation and enhances capillary trapping of the non-wetting phase.[402] The raw micro-PIV image and the corresponding velocity field are shown in Fig. 14F. After CO_2 breakthrough, micro-PIV visualizations revealed vorticity contours near the CO_2–brine interface, indicating water recirculation zones that may enhance CO_2 dissolution and improve solubility trapping.[397,400]

Microfluidic studies have demonstrated that capillary trapping efficiency depends strongly on the viscosity ratio (M), capillary number (Ca), and surface wettability. By optimizing CO_2 injection rates, viscosity, and interfacial properties, CO_2 underground storage in saline aquifers can be enhanced. Microfluidic studies have also shown that CO_2 foam injection, by increasing M, has potential for creating a stable displacement front. Future research involving advanced techniques, such as micro-PIV, could further elucidate pore-scale flow dynamics and inform strategies for efficient carbon storage.[397,400]

4.2 CO_2 solubility trapping

Solubility trapping involves CO_2 dissolving into reservoir brine.[371,376] At the CO_2–brine interface, CO_2 diffuses due to a concentration gradient, and the process of mass transfer is further enhanced by fluid recirculation and density-driven brine convection.[371,376] The combined mechanisms of diffusion and convection significantly accelerate the dissolution of CO_2. Solubility trapping is influenced by key parameters such as solubility, diffusion rate, and the mass transfer coefficient. These parameters are critical for estimating storage capacity under specific pressure, temperature, and brine composition. Microfluidic platforms, often integrated with optical and spectroscopic methods, have proven effective for quantifying CO_2 solubility,[384] diffusivity,[83] and mass transfer coefficients.[84,96,99,100,385–389,403]

4.2.1 Solubility measurements. Solubility is a crucial thermodynamic property used to estimate the theoretical CO_2

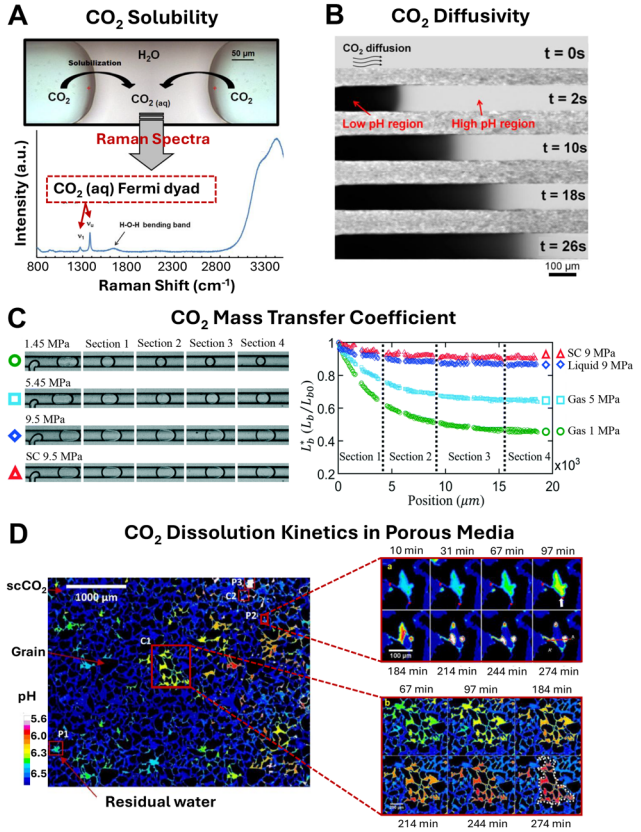

Fig. 15 Microfluidic investigations into CO_2 solubility, diffusivity, mass transfer coefficient, and dissolution kinetics in porous media. (A) CO_2 solubility: Raman spectroscopy combined with microfluidics quantifies CO_2 solubility in brine at various temperatures, pressures, and salinities, with characteristic Fermi dyad peaks for dissolved CO_2(aq) (adapted with permission from Liu *et al.*[384] Copyright © 2012 Elsevier). (B) CO_2 diffusivity: fluorescence microscopy visualizes CO_2 diffusion at the CO_2–brine interface, where low-pH regions correspond to higher CO_2 concentrations. Adapted with permission from Sell *et al.*[83] Copyright © 2013 American Chemical Society. (C) CO_2 mass transfer coefficient: microfluidic experiments with elongated CO_2 bubbles in serpentine microchannels measure bubble length reduction under varying pressures and CO_2 phases (gas, liquid, supercritical), showing spatial and phase-dependent mass transfer rates (adapted from Ho *et al.*[84] under CC-BY License). (D) CO_2 dissolution kinetics in porous media: high-resolution pH mapping visualizes the dissolution of supercritical CO_2 into residual water in porous micromodels over time, revealing spatially varying dissolution patterns and pH changes (adapted with permission from Chang *et al.*[382] Copyright © 2016 Elsevier).

storage capacity in saline aquifers.[371] Liu *et al.*[384] utilized Raman spectroscopy integrated in a microfluidic setup to investigate CO_2 solubility under varying conditions of temperature (T = 22–100 °C), pressure (P = 1.1–10 MPa), and salinity (S = 0–3 mol L^{-1}).[384] In their experiments, a segmented flow of CO_2 in brine was first stabilized before the flow was stopped.[384] As shown in Fig. 15A, Raman spectroscopy measured the intensity of the CO_2(aq) band in the aqueous phase to calculate the mole fraction of dissolved CO_2.[384] The band intensity stabilized within one minute, indicating that equilibrium had been reached.[384] Their study revealed that CO_2 solubility (0–0.025 mol mol^{-1} water) increases with CO_2 density, but decreases as salinity increases from 0 to 3 mol L^{-1}.[384]

4.2.2 Diffusivity studies. Diffusivity, or the diffusion coefficient, describes the rate at which CO_2 molecules move under a concentration gradient in brine. Sell *et al.*[83] used fluorescence microscopy to measure CO_2 diffusivity in brine with varying salinities at a static CO_2–brine interface.[83] They quantified the amount of CO_2 dissolution by monitoring pH changes, reflected in fluorescence intensity (see Fig. 15B).[83] Their results showed that CO_2 diffusivity decreases exponentially with increasing salinity (0–5 mol L^{-1}), while pressure (5–50 bar) had minimal impact.[83]

4.2.3 Mass transfer coefficient. Microfluidic platforms have also recently been used to study microbubble dissolution kinetics, motivated by the mechanisms of CO_2 solubility trapping.[84,96,99,100,385–389,403] The volumetric mass transfer coefficient, k_La, quantifies the rate of CO_2 mass transfer into the liquid, where k_L is the liquid-side mass transfer rate and a represents the interfacial area per unit liquid volume. Microfluidic measurements more accurately simulate processes occurring within micron-scale pores. The high surface-to-volume ratio in microchannels leads to k_La values that are 2–3 orders of magnitude greater than those in millimeter-scale systems.[84] Using hydrodynamic focusing or T-junction designs, elongated CO_2 bubbles are generated in serpentine channels, allowing researchers to monitor bubble length reduction and quantify k_La, as shown in Fig. 15C.[84,100,386,388] The shrinkage of CO_2 bubbles reflects interfacial mass transfer, typically showing a rapid dissolution rate initially, followed by a slower rate downstream.[84,100,386,388] In these experiments, convection played a dominant role over diffusion, significantly influencing mass transfer dynamics.[100,388] Ho *et al.*[84] studied CO_2 dissolution across varying pressure and temperature conditions for gaseous, liquid, and supercritical CO_2.[84,99] Gaseous CO_2 showed greater bubble size reduction due to its higher solubility, while supercritical CO_2 achieved the highest k_La, due to elevated temperatures enhancing molecular diffusion.[84,99] Yang and Tsai[100] investigated the effects of flow rate and brine salinity on supercritical CO_2 mass transfer in a microchannel.[100] Their findings revealed that the flow rate had a more pronounced impact on k_La compared to salinity.[100] A mass transfer rate correlation derived from microfluidic segmented flow experiments could provide valuable predictions of k_La under specific pressure, temperature, flow rate, and salinity.

4.2.4 Dissolution kinetics in porous media. Using microfluidic porous media, CO_2 dissolution kinetics in water have been investigated.[381,382,394] In Fig. 15D, Chang *et al.*[381] employed a fluorescent dye as a pH indicator to observe the transient dissolution of supercritical CO_2 in water over time.[381,382] By analyzing the pH change in water clusters, they concluded that the CO_2 dissolution rate primarily depends on the surface-to-volume ratio of the residual water clusters available for dissolution.[382] Additionally, the water flow path

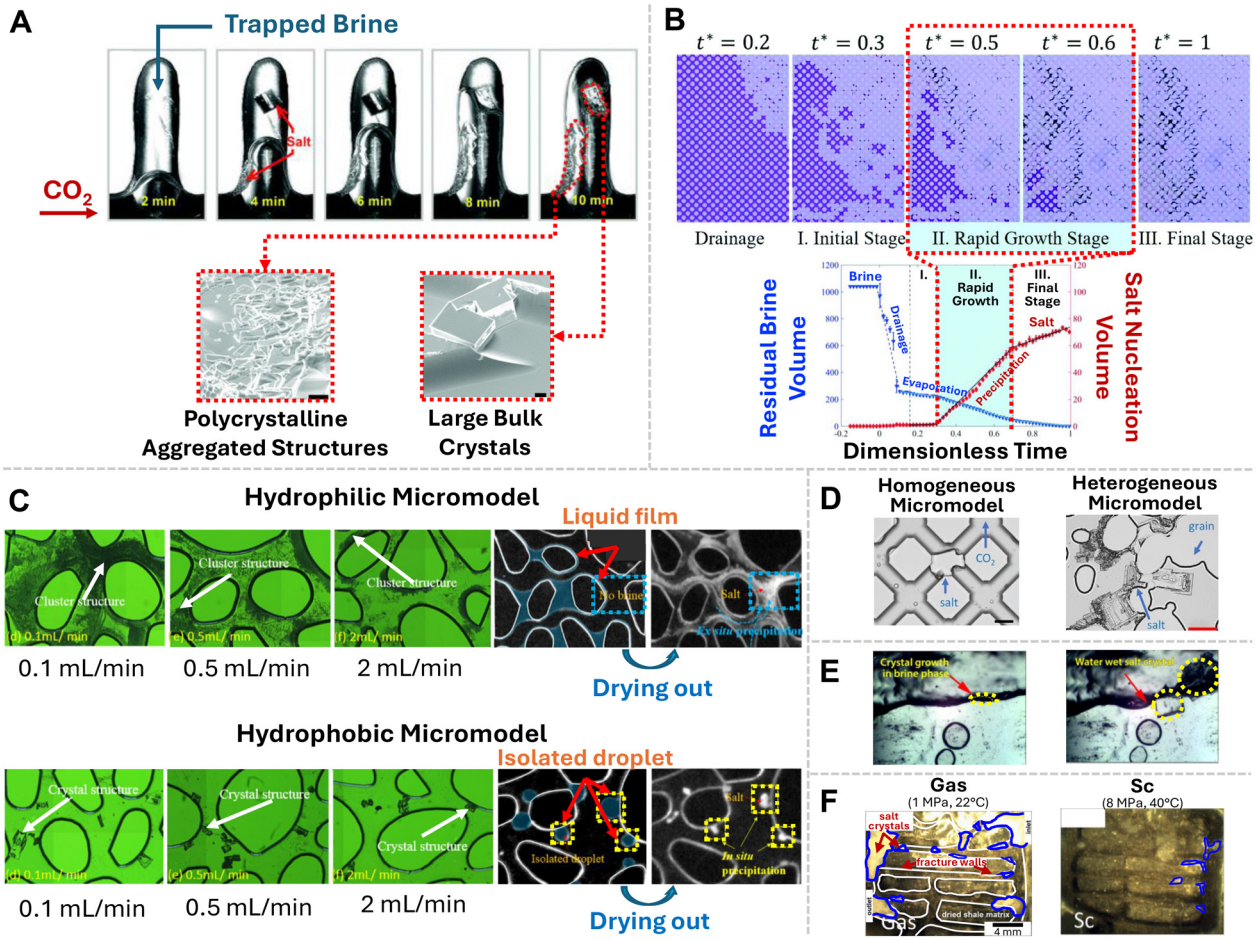

Fig. 16 Microfluidic investigations of salt precipitation during CCS in saline aquifers: (A) salt precipitation in microchannels with isolated brine-filled pores, showing two distinct types: polycrystalline aggregates and large bulk crystals (adapted with permission from Kim *et al.*[405] Copyright © 2013 the Royal Society of Chemistry). (B) Microfluidic experiment illustrating temporal evolution of salt precipitation, including the initial stage, rapid growth stage and final stage, with corresponding residual brine and salt nucleation volumes plotted below (adapted with permission from Ho and Tsai.[116] Copyright © 2020 the Royal Society of Chemistry). (C) Salt precipitation patterns in hydrophilic (top) and hydrophobic (bottom) micromodels at various flow rates, showing residual brine as liquid films in hydrophilic micromodels and as isolated droplets in hydrophobic micromodels (adapted with permission from He *et al.*[407] Copyright © 2019 American Chemical Society). (D) Comparison of salt precipitation in homogeneous (left) and heterogeneous (right) micromodels, highlighting the effect of pore structure and capillary pressure distribution (adapted from Yan *et al.*[408] under CC-BY License). (E) Close-up view of salt crystal growth near the CO_2–brine interface, illustrating crystal growth in the brine phase and water-wet regions (adapted with permission from Miri *et al.*[406] Copyright © 2015 Elsevier). (F) Salt precipitation during gas (left) and supercritical CO_2 (right) injection, observed in a micromodel fabricated from a real sandstone slice bonded with glass (adapted with permission from Nooraiepour *et al.*[24] Copyright © 2018 American Chemical Society).

and its velocity within the CO_2 cluster significantly influenced the mass transfer rate in microfluidic porous media.[381]

In summary, microfluidic platforms have proven to be effective tools for measuring key parameters of CO_2 solubility trapping, such as the solubility and diffusivity of CO_2 in brine under various pressure, temperature, and salinity conditions. Their high surface-to-volume ratio enables precise characterization of dissolution kinetics, providing valuable insights into mass transfer dynamics in subsurface porous media. Future research could explore the combined effects of CO_2 dissolution and salt precipitation, which are important for understanding and optimizing storage efficiency in CCS applications.

4.3 Salt precipitation

One major technical challenge during CCS operations is salt precipitation and clogging. Injection of dry CO_2 into saline aquifers causes brine evaporation, leading to excessive salt deposition, which reduces porosity, permeability, injectivity, and storage efficiency.[404] Recent microfluidic studies have provided direct visualization of salt precipitation processes in saline aquifers, shedding light on permeability loss and injectivity changes.[24,116,405,406] This pore-scale visualization has revealed salt morphology and precipitation dynamics, offering insights into mitigation strategies.

4.3.1 Salt morphology. Using microfluidic devices, Kim *et al.*[405] conducted one of the first pore-scale visualizations of

salt precipitation during CO_2 injection. They identified two distinct types of salt precipitation: as illustrated in Fig. 16A-top, large, semi-transparent cubic crystals formed within the brine phase away from the CO_2–brine interface, while smaller, darker polycrystalline aggregates formed along the interface.[405] In a separate experiment using a randomly connected glass microchannel network, Kim *et al.*[404] reported a final salt coverage of 18%. Scanning electron microscopy (SEM) images (Fig. 16A-bottom) revealed salt crystals spanning the entire width of a 70 μm channel and polycrystalline aggregates ranging from 1 to 10 μm.[405]

4.3.2 Temporal evolution of precipitation. Microfluidic studies have also been used to investigate the temporal evolution of salt precipitation.[116] Ho and Tsai[116] injected air into NaCl brine and identified three key stages, as shown in Fig. 16B:[116] (I) an initial stage with predominant brine evaporation and minimal precipitation, (II) a rapid growth stage characterized by a high linear precipitation rate that contributed to 75% of total precipitation, and (III) a final stage with slower crystal growth due to insufficient brine to supply salt ions.[116] Moreover, greater salt precipitation was observed near the outlet, attributed to the trapping of residual brine in that region, whereas brine near the inlet was displaced by the injected gas.[116]

4.3.3 Effect of surface wettability. Surface wettability significantly influences salt precipitation.[407,409,410] Recent microfluidic experiments under high-pressure (10 MPa) and high-temperature (50 °C) conditions highlight the pronounced differences between salt precipitation patterns in hydrophilic and hydrophobic micromodels, as shown in Fig. 16C.[407] Hydrophilic surfaces tend to promote more extensive salt formation in the form of polycrystalline clusters. Brine adhered strongly to the porous surface, forming residual pools, liquid bridges, and films that served as a continuous source of salt ions for precipitation.[407] Capillary-induced brine reflow further reinforced localized salt aggregation.[407,410] Increasing CO_2 injection rates in hydrophilic systems reduced capillary reflow and precipitation. By contrast, hydrophobic surfaces (water contact angle = 119°) exhibited isolated brine droplets and slower precipitation rates, forming large crystals only in brine pools.[407] Spatial variation in salt patterns was greater in hydrophobic systems, reflecting the probabilistic nature of crystallization.[410]

4.3.4 Effect of porous media heterogeneity. Porous media heterogeneity further affects salt precipitation by influencing capillary pressure distribution.[408] Yan *et al.*[408] compared homogeneous media with uniform pore sizes (90 μm) to heterogeneous media containing rock-shaped grains (Fig. 16D).[408] Heterogeneous media retained more brine (45% *vs.* 28%) due to non-uniform capillary pressure, resulting in higher salt saturation (9.5%, 1.9 times that of homogeneous media).[408]

4.3.5 Self-enhancing salt growth. In a hydrophilic glass micromodel, Miri *et al.*[406] visualized a salt precipitation mechanism referred to as self-enhancing growth.[406] Due to the hydrophilic nature of salt, once nucleation occurs within the CO_2 stream, a thin brine layer is attracted to the salt surface.[406] This layer continuously evaporates, resulting in the formation of larger salt aggregates and accelerating both the rate and amount of precipitation.[406] This process is illustrated in Fig. 16E, where the self-enhancing growth mechanism promotes localized salt accumulation at the CO_2–brine interface.[406]

4.3.6 Effect of CO_2 phase state. The phase state of CO_2 (gas, liquid, or supercritical) also has a significant impact on salt precipitation.[24] Nooraiepour *et al.*[24] developed a novel microfluidic system using geomaterials—a shale sample from the Norwegian North Sea, a proposed CO_2 storage site.[24] Fracture patterns were laser-etched into the shale specimen, and CO_2 was injected at varying pressures (1, 5, and 8 MPa) and temperatures (22, 40, and 60 °C) to compare salt precipitation under gaseous, liquid, and supercritical CO_2 conditions.[24] As shown in Fig. 16F, at a flow rate of 20 cm^3 min^{-1}, the average salt coverage was 11%, 3%, and 0.8% for gaseous, liquid, and supercritical CO_2, respectively.[24]

This trend is attributed to the higher density of liquid and supercritical CO_2, which displaces more residual brine from the pore spaces, thereby reducing the extent of salt precipitation. Additionally, water evaporation in CO_2 decreases significantly as pressure increases from 1 to 8 MPa, further limiting salt formation under supercritical conditions.[24] These combined factors explain the greater salt precipitation observed during gaseous CO_2 injection compared to liquid or supercritical phases.[24]

Findings from microfluidic studies suggest strategies to mitigate salt precipitation, such as altering surface wettability to hydrophobic or increasing CO_2 injection rates. While current microfluidic studies mostly use pure NaCl solutions, future research should explore synthetic brines containing mixed salts under high-pressure and high-temperature conditions. The development of advanced "reservoir-on-a-chip" systems could provide deeper insights into salt precipitation mechanisms under more realistic conditions. By incorporating clay minerals, calcite particles, or actual slices of reservoir rock, these systems could replicate authentic fluid–solid interactions that occur in geological formations.[21–24] Real geosamples in microfluidic platforms would allow for the investigation of how salt precipitation is influenced by natural mineral heterogeneity, geochemical interactions, and wetting behavior, offering field-relevant data for optimizing CCS operations. Such innovations would significantly enhance our understanding of salt precipitation dynamics and guide the development of effective mitigation strategies.

5 Microfluidic studies on underground hydrogen storage

In response to climate change, the transition to clean energy sources has been accelerating. Hydrogen (H_2), as a carbon-

free energy carrier, stands out as a promising alternative to traditional fossil fuels. Underground hydrogen storage (UHS) involves storing hydrogen gas in geological formations, such as salt caverns, depleted oil and gas reservoirs, or aquifers, for later use.[411–413] This method is critical for managing the supply and demand in hydrogen energy systems, enabling large-scale, cost-effective storage that supports renewable energy integration and enhances energy security. While salt caverns are known for their impermeability and structural stability, depleted reservoirs and aquifers offer greater capacities.[411] Beyond storage efficiency and recovery factors at the macroscale (*i.e.*, reservoir-scale) level, microscale fluid dynamics with these geological settings provides vital insights into pore-level visualization of fluid–fluid and fluid–solid interactions, providing a deeper understanding of the trapping mechanism and displacement efficiency.[411,414–416] Given the varying dynamics of fluid movements, geochemical interactions, and microbial activity across different geological sites, comprehensive feasibility studies are essential for a successful UHS project.

5.1 Hysteresis effect and trapping mechanism

Unlike CO_2 sequestration, hydrogen storage involves cyclical injection of hydrogen into a liquid-saturated system underground (drainage stage) and withdrawal of hydrogen from underground (imbibition stage) repeatedly.[417] This cyclic operation introduces a hysteresis effect within the system, where hydrogen is trapped and the distribution of hydrogen gas clusters within the pore space (*i.e.* gas connectivity) is varied with each loading cycle, affecting the storage efficiency each time.[415,417,418] Various trapping mechanisms, *e.g.*, capillary trapping, dissolution trapping, roof snap-off,[419] and hysteresis trapping, influence the extent to which hydrogen is retained in subsurface formations.[415,417,420] Microfluidic devices are instrumental in visualizing the complex pore-scale phenomenon.[2,178,414–418,421–424]

Recent studies by Gao *et al.*[418] and Bahrami *et al.*[417] have found that hydrogen saturation increases with the number of cycles,[417,418] and hydrogen storage capacity also increases with larger injection rates.[414–416,421] The increase in the number of cycles also intensifies the phenomenon of water block, where liquid phases at the corners and dead-ends of large pores are difficult to displace, reducing the overall porosity utilization.[418] The hydrogen-liquid phase permeability hysteresis in such a multi-cycle gas injection process lowers the H_2 storage efficiency over time.

Using pore-scale mechanisms—preferential-to-uniform flow transformation, floating flow, and dead-end pore invasion—Song *et al.*[421] demonstrated the effects of pore heterogeneity, injection flux, and oil/brine distribution on the efficiency and capacity of a hydrogen storage site.[421] Their study suggested that brine-saturated initial conditions, coupled with high injection flux and median pore heterogeneity, provide optimal storage performance. Although a high capillary number (*i.e.*, high injection rate) benefits storage capacity during the drainage stage, it compromises gas connectivity.[415,417,423] Roof snap-off,[419] driven by interfacial force, fragments large gas clusters into smaller ones.[414,415,417,423,424] Disconnected gas clusters are often trapped during imbibition (when extracting hydrogen) and may be reconnected in subsequent cycles, but the likelihood depends on the pore cluster morphology.[415,417,424] As shown in Fig. 17A, the large gas cluster (colored green) from the primary drainage cycle is separated into multiple small clusters (colored red, blue, brown, orange, *etc.*) after imbibition. Some of these disconnected gas clusters remain disconnected at the end of the secondary drainage cycle (pointed at by the red arrows), which result in the increase of the hydrogen–water interface and further promotion of hydrogen loss through dissolution into the liquid phase.[411] Although the loss of hydrogen due to dissolution, and the mixture of hydrogen with other pre-existing gases in the reservoir can be reversible by gas separation,[425,426] the separation process often is undesirable due to its energy/equipment requirement, introducing additional cost. Furthermore, the unchanged gas cluster in Fig. 17B suggests that preferential water flow bypassed some of the gas clusters,[417] leading to permanent trapping for gas clusters. Water encapsulation, film flow, and bypassing during multi-cycle injections exacerbate permeability losses for hydrogen, reducing efficiency in hydrogen extraction.[417,418]

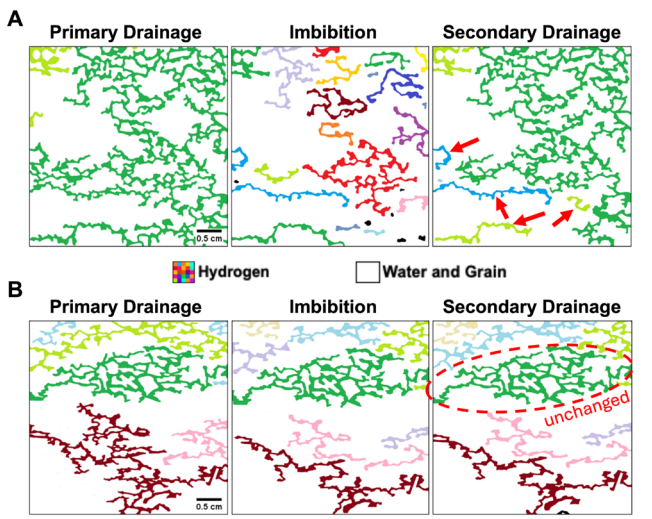

Fig. 17 Connectivity of hydrogen gas in a multi-cycle process. Clusters of hydrogen gas are represented in different colors, while water and grain are kept in white. (A) Disconnection of hydrogen gas clusters due to roof snap-off[419] during imbibition could remain disconnected upon the subsequent drainage cycle (pointed at by the red arrows). (B) Large cluster of hydrogen gas remains unchanged over different cycles, suggesting that a preferential flow path of water bypasses the gas clusters. This causes permanent trapping of hydrogen gas and reduction in recovery efficiency (adapted with permission from Bahrami *et al.*[417] Copyright © 2024 Elsevier).

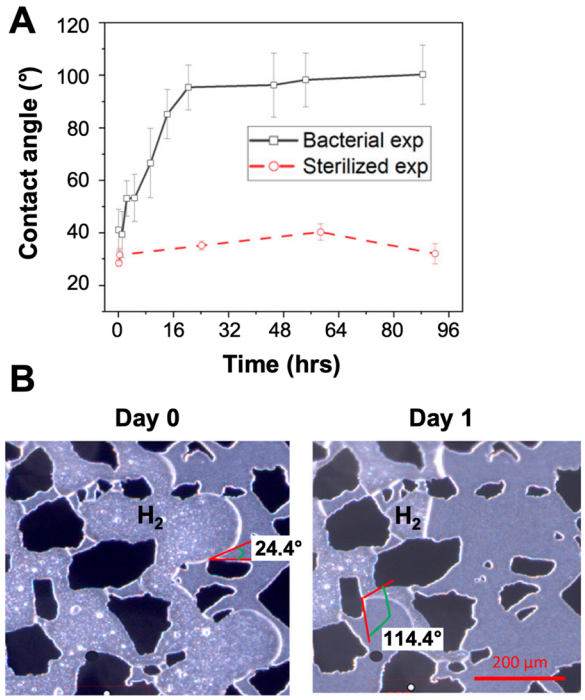

Fig. 18 Influence of microbial activity on wettability. (A) Average hydrogen contact angle (CA) changes over time between experiments with and without the presence of bacteria. (B) *In situ* CA measurement of hydrogen in the first two days. Bacteria induce average hydrogen CA to increase significantly, reducing the water wettability in the microfluidic chip (adapted from Liu *et al.*[429] under CC-BY License. Copyright © 2023 Liu, Kovscek, Fernø and Dopffel).

5.2 Wettability effect

Wettability significantly influences the displacement efficiency of hydrogen in porous media. Experimental results indicate that hydrogen–water systems are predominantly water-wet.[414,417,423,427] van Rooijen *et al.*[427] (2022) demonstrated that the hydrogen dynamic contact angles decrease with decreasing channel width in hydrogen–water–glass microfluidic systems.[427] The strongly water-wet nature leads to water preferentially coating solid surfaces, influencing displacement fronts and gas mobility.[417] Furthermore, contact angle measurement reveals that hydrogen saturation is highly sensitive to pressure changes; high pressure corresponds to higher hydrogen gas density and more hydrogen-wet conditions.

Aquifers with predominantly KCl (potassium chloride) promote water-wet nature—suggesting the role of ionic radius and strength—favoring better hydrogen storage due to optimal pore occupancy.[424] While increasing salinity leads to increased hydrogen contact angle (*i.e.* less water-wet), the dissolution of hydrogen gas in higher salinity brine is reduced. The results by Medina *et al.*[424] suggest three competing factors: diffusion capacity, average bubble size, and capillary pressure influencing the dissolution time.[424] The *in situ* contact angle measurement utilizing microfluidic studies suggests that optimizing injection strategies and modifying wettability conditions could alter the trapping mechanism of hydrogen, which significantly influences the hydrogen storage efficiency.

5.3 Microbial activity

Microbial activity, or the biotic process, plays a crucial role in the efficiency of UHS, impacting hydrogen retention, storage stability, and recovery rates.[411] A biofilm is a structured community of microorganisms that adheres to the rock surfaces and encases itself in a self-produced extracellular polymeric substance (EPS),[428] providing protection from external stresses. The presence of microbial communities in subsurface environments can lead to hydrogen consumption, biofilm formation, and pore-space clogging, all of which can reduce the long-term viability of hydrogen storage.[2,411,429,430] As shown in Fig. 18A and B, Liu *et al.*[429] (2023) demonstrated that microbial activity alters surface wettability by increasing the average hydrogen contact angle in hydrogen–water–silicon microfluidic systems, shifting from a water-wet (41°) to a neutral-wet (96°) state. Compared to the water contact angle (28°) in a sterilized experiment, the wettability change can lead to disconnected hydrogen gas clusters.

The increased surface area of hydrogen clusters also results in a greater consumption rate of hydrogen gas by microbial metabolism. Both of these effects induce a significant reduction in recovery efficiency.[429] The hydrogenotrophic sulfate reduction process:[429] $SO_4^{2-} + 4H_2 + H^+ \rightarrow HS^- + 4H_2O$, generates massive amounts of water, leading to the secondary loss of hydrogen gas by dissolution and reduced pore space for hydrogen gas.[411]

The presence of bacteria also introduces bio-induced clogging due to the formation of biofilms.[431] Biofilm development at the pore-scale is influenced by the flow velocity and nutrient concentrations. While high nutrient concentrations promote microbial growth, they also weaken biofilm adhesion, making it prone to detachment under high shear flow conditions.[431] Optimization of these key parameters can help to prevent biofilm accumulation, which directly impacts the storage efficiency of hydrogen gas. It is suggested that optimizing initial microbial population conditions could enhance hydrogen storage efficiency by minimizing clogging while maintaining long-term stability.[430] In contrast to the consumption of hydrogen (*e.g.*, methanogenesis, acetogenesis), the generation of hydrogen gas through the enzyme hydrogenase,[432] is rarely explored in the literature. Investigating microbial reactions that favor the generation of hydrogen in subsurface environments using microfluidics could provide insights. In the absence of sunlight, dark fermentation could be a potential pathway for biohydrogen production.[433] In this process, biogenic wastewater replaces water as the displacing fluid in the hydrogen system, where the wastewater also acts as a feedstock for the microorganisms and potentially could enhance hydrogen production. Given the diversity of microbial populations in nature,[432] comprehensive studies of

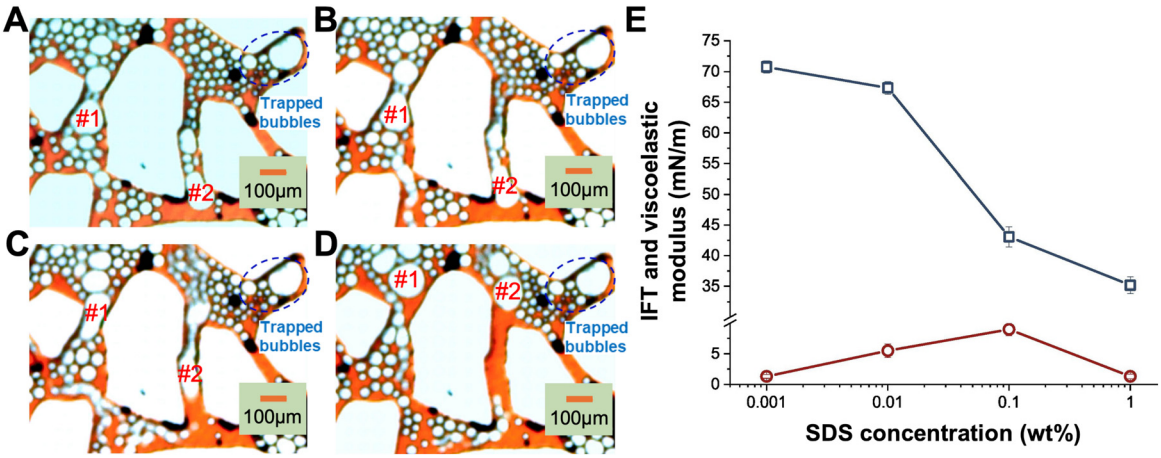

Fig. 19 Investigation of hydrogen foam. (A)–(D) Sequential images showing hydrogen foam dynamics at times ranging from 5.5 s to 6.4 s, capturing trapped hydrogen bubbles. Large bubbles (marked #1, #2) are obstructed in narrow pores, increasing flow resistance. (E) Graph of interfacial tension (IFT, blue □) and viscoelastic modulus (red ○) for H_2 and SDS solution at varying concentrations (adapted with permission from Lu *et al.*[422] Copyright © 2024 Elsevier).

bacterial interactions at potential geological sites are essential, beyond focusing on single strains of bacteria.[429]

5.4 Hydrogen foam

The use of foam-assisted approach in EOR has been widely studied over the past decades (as discussed in section 3.4), however, the investigation of hydrogen foam in UHS remains underexplored in the literature. The implementation of hydrogen foam compared to pure hydrogen gas has been shown to improve the oil recovery rate by 17.95% and storage efficiency to 36.2% (ref. 434) at the end of the drainage cycle. Analysis using microfluidic chips shows that a mechanism of foam trapping is introduced, where trapped bubbles in pore throats and corners prevent hydrogen gas from exiting during the imbibition cycle,[422] as shown in Fig. 19A–D. In addition, pore clogging induced by large-sized bubbles (marked as bubble #1 and #2 in Fig. 19A–D) was observed during the experiment. Deformation of these bubbles to pass through constricted pores causes a reduction in mobility and resistance of the flowing bubbles. Though, this foam-assisted approach—combined with amphiphilic surfactants like SDS—has shown potential in enhancing storage efficiency by catalyzing hydrogen adsorption *via* the hydrophobic side chain of SDS,[422] as shown by the interfacial tension (IFT) and viscoelastic modulus of hydrogen under various concentrations of SDS in Fig. 19E.

Furthermore, the use of hydrogen foam can act as a barrier to prevent microbial-induced hydrogen losses (discussed in section 5.3) by limiting the interaction between hydrogen and aqueous phases. The encapsulation of hydrogen gas in foam serves as a great potential solution for unideal storage sites, particularly in depleted oil reservoirs, where many aspects concerning geological, chemical, and biological reactions are present.[410,411] Besides, the diffusion of hydrogen gas due to its small molecular size and high diffusivity, compared to other gases such as CO_2, poses a major challenge. By acting as an additional sealing layer, hydrogen foam can also help to suppress the diffusion loss of hydrogen gas through caprock, wellbore seals, *etc.*

6 Conclusions and perspectives

Microfluidics has proven to be invaluable in addressing greenhouse gas emissions and advancing energy storage solutions by exploring subsurface flows in applications, such as CO_2-enhanced oil recovery (CO_2-EOR), carbon capture and storage (CCS), and underground hydrogen storage (UHS). This review discusses advancements in lab-on-a-chip (LOC) technologies and insights gained into relevant key subsurface-flow processes, including fluid–fluid displacement, interfacial phenomena, surface wettability effects, porous media heterogeneity, and microbial activity. Despite significant progress, considerable opportunities for further research and innovation remain.

6.1 Challenges and opportunities in LOC fabrication and visualization

Soft lithography has facilitated the fabrication of microfluidic chips for EOR studies. However, limitations such as PDMS deformation under high pressure and inadequate bonding strength[47,72,73] restrict its use to low-pressure experiments, which may not accurately capture fluid miscibility and phase behavior at higher pressures. Moreover, PDMS can swell upon contact with hydrocarbons, potentially altering the microfluidic structures and compromising experimental accuracy. To overcome these limitations, alternative materials with higher Young's modulus, such as polyethylene terephthalate (PET) or polyimide (PI), offer greater durability and are promising alternatives for PDMS-based microfluidics.[48,435,436]

For high-pressure, high-temperature (HPHT) applications, current lab-on-a-chip (LOC) models often employ silicon and glass microfabrication for enhanced pressure resistance. However, these materials are limited in scalability, cost-efficiency, and design flexibility. Promising alternatives include 3D printing with high-strength, HPHT-compatible materials,[437–440] *e.g.*, two-photon polymerization (TPP) and microstereolithography (SLA) being particularly promising for their high resolution. 3D-printed HPHT LOCs can eliminate the need for cleanroom microfabrication, enabling rapid prototyping and greater design versatility. In addition, hybrid fabrication techniques that combine laser cutting (for rapid material removal) with micromachining can optimize speed, precision, and scalability.[441] Leveraging these innovations could make HPHT LOC systems more robust, versatile, and commercially viable for broader scientific and industrial use.

In microfluidic investigations of subsurface flow processes, significant limitations remain in accurately replicating the structural and geochemical heterogeneity of natural rock formations. One fundamental limitation is the mismatch between materials commonly used in LOC systems—such as PDMS, glass, or silicon—and reservoir rocks. These materials lack the native mineral composition and reactive properties necessary to capture key geochemical interactions, such as mineral dissolution, precipitation, and wettability changes in CO_2 and hydrogen storage applications. A promising approach is the integration of thin-sectioned natural rock samples within microfluidic devices,[24] allowing for more representative mineral–fluid interactions. Additionally, functionalized surfaces engineered to mimic specific mineral compositions, such as kaolinite[21] and carbonate minerals,[276,374] offer a synthetic alternative for studying wettability and reactive processes.

Another major challenge is the reproduction of structural heterogeneity in microfluidic devices. Reservoirs exhibit intricate pore networks with variations in connectivity, tortuosity, and permeability,[442] which are often oversimplified in LOC models due to microfabrication constraints. While these small-scale structural features play a crucial role in fluid transport, existing microfluidic systems struggle to accurately reproduce sub-micron pore structures that govern multiphase flow behavior in ultra-tight formations. Emerging high-resolution fabrication techniques, such as focused ion beam,[443] two-photon polymerization 3D printing[444] and metal-assisted chemical etching,[445] can enable the creation of sub-micron features, significantly improving the representativeness of LOC models for tight reservoirs.

Furthermore, most current studies focus on 2D visualization for microfluidic applications, limiting the ability to fully capture 3D multiphase flow dynamics, wettability behavior, and pore-scale interactions in three-dimensional porous media. Future research can focus on improving the compatibility of real-time 3D optical imaging methods to achieve more realistic experimental conditions for subsurface flow investigations, allowing an extended view of interest. For instance, optical coherence tomography (OCT) could be integrated with microfluidics to provide depth-resolved cross-sectional images, enabling real-time visualization of fluid interfaces, phase distributions, and internal flow structures.[446]

Microfluidic studies of subsurface flow have produced diverse micromodel designs and provided detailed pore-scale visualizations. However, most research remains case-specific. Broader standardization in design, procedures, and data reporting is needed for reliable cross-laboratory benchmarking. Some efforts exist: ISO 22916 defines standard dimensions for microfluidic interconnection holes, improving device compatibility.[447,448] Chips & Tips,[449] hosted by *Lab on a Chip*, offers practical advice on chip fabrication and maintenance. However, these resources are fragmented, with few shared micromodel designs or standardized datasets for comparative studies.

A promising path forward lies in developing shared platforms for micromodel designs, imaging datasets, and experimental measurements. The Digital Porous Media Portal[450] serves as a strong example of a community-driven initiative that supports data sharing and international contributions.[451,452] Since its launch in 2015, the repository has hosted real rock microstructure datasets and experimental measurements from over a hundred projects, providing a valuable foundation for designing geologically realistic micromodels. Establishing a similar platform focused on microfluidic subsurface flow would greatly benefit the field by enabling meaningful cross-study comparisons and consistent validation.

Upscaling pore-scale microfluidic results to field-scale pilot tests and reservoir models remains a persistent challenge, primarily due to discrepancies in characteristic length and time scales, as well as differences in heterogeneity —particularly in porosity, permeability, and wettability— across a wide range of scales.[453,454] Despite recent advancements, there is still limited understanding of how to systematically incorporate key parameters, especially pore geometry and wettability distributions, into large-scale models for reliable prediction of fluid flow behavior.[11,359] The balance between viscous and capillary forces—typically expressed through the capillary number—along with associated flow dynamics and pressure gradients, can vary significantly from micro- to macro-scales.[453,455,456] Consequently, multiple formulations of the capillary number (microscopic, macroscopic, and hybrid) have been developed, each tailored to specific scales. At the reservoir scale, capillary numbers typically range from 10^{-8} to 10^{-2},[457–459] whereas in microfluidic systems they generally fall between 10^{-3} and 10^{-1}.[390]

Several frameworks have been proposed to bridge pore- and reservoir-scale behaviors by incorporating essential physical attributes such as capillary forces, porosity–

permeability relationships, and wettability variation. Classical models like the Leverett *J*-function[460] address capillary pressure scaling, while empirical correlations such as the Kozeny–Carman equation[461,462] relate porosity and permeability. Time scaling has been treated through transient pressure type-curve analysis,[463] and spatial wettability heterogeneity has been explored in recent micromodel studies.[464] These insights, combined with core-scale experiments and high-resolution imaging, inform reservoir-scale modeling approaches such as pore-network modeling,[465] direct numerical simulation,[466] and volume-averaging theory[467] to simulate multiphase flow in geologically complex porous media.[468–470]

While these upscaling methods are continuously refined to simulate large-scale anisotropic, heterogeneous subsurface formations and rigorously predict multiphase processes,[471] microfluidics—though powerful tools for visualizing pore-scale processes—introduces better simplifications than rock core samples. In addition to scale mismatches, microfluidic devices are generally quasi-2D with idealized pore networks and uniform wettability, and thus cannot capture the full 3D heterogeneity of reservoir rocks.[11,141,361] Furthermore, glass or silicon substrates do not reproduce the mineralogy of sandstones, shales, or carbonates, and therefore often neglect geochemical interactions.[138]

Such multi-component chemical interactions—*e.g.*, calcite ($CaCO_3$) dissolution in brine (eqn (4)–(6)) and the precipitation of various minerals depending on the available cations (eqn (7) and (8))[472,473]—between the fluids and the solid rock surface can strongly alter wettability, permeability, and displacement mechanisms.[140,474]

$$CaCO_3 + CO_2 + H_2O \rightleftharpoons Ca^{2+} + 2HCO_3^-, \quad (4)$$

$$CaCO_3 + H^+ \rightleftharpoons Ca^{2+} + HCO_3^-, \quad (5)$$

$$CaCO_3 + H_2CO_3^* \rightleftharpoons Ca^{2+} + 2HCO_3^-, \quad (6)$$

$$HCO_3^- + Ca^{2+} \rightleftharpoons CaCO_3 + H^+, \quad (7)$$

$$HCO_3^- + Mg^{2+} \rightleftharpoons MgCO_3 + H^+, \quad (8)$$

Although several "rock-on-chip" studies have incorporated geochemical reactions,[138,141,142] further development of simpler and more reliable fabrication methods that integrate geologically relevant materials is still required for simulating coupled flow–transport–reaction processes.

Despite these challenges, continued advancements in microfluidic fabrication, material engineering, and real-time monitoring techniques hold promise for developing more representative LOC models. Bridging the gap between laboratory experiments and reservoir conditions will require interdisciplinary efforts across materials science, microfabrication, and geochemistry to refine these platforms for subsurface applications.

6.2 Future outlook for microfluidic investigations on CCUS and UHS

Beyond structural and geochemical replication, understanding multiphase flow behavior in CCUS and UHS is challenging. While miscibility is preferred for EOR, achieving the minimum miscibility pressure may not always be feasible due to reservoir pressure constraints. In such cases, immiscible CO_2 injection remains a promising alternative, but its effectiveness is influenced by complex three-phase interactions (brine–oil–gas), wettability changes, and fluid displacement mechanisms, which vary with rock types, fluid compositions, and reservoir conditions. Further complexity arises in hybrid EOR methods, such as water-alternating-gas (WAG), foam, and polymer/surfactant flooding, which have demonstrated delayed CO_2 breakthrough and improved sweep efficiency. However, the underlying mechanisms governing these improvements remain insufficiently understood. Future research should focus on the screening and optimizing injection strategies using microfluidic platforms, which offer efficient and cost-effective tools for studying synergistic effects in CO_2-based EOR and CCUS applications.

Microfluidic studies on CO_2 foam-EOR have demonstrated promising and reproducible results in enhancing sweep efficiency, reducing viscous fingering, and preventing gravity override, offering significant improvements over CO_2 gas alone. However, optimizing CO_2 foam for EOR faces several challenges, particularly in stabilizing foam in the presence of crude oil. Such optimization processes can be accelerated using microfluidic chips under reservoir-relevant conditions, including pressure, temperature, brine salinity, rock mineralogy, wettability, petrophysical properties, and oil composition.

Emerging interests include the use of green, eco-friendly surfactants,[475] such as saponins, cellulose, and proteins, which have the potential to enhance foam stability while minimizing formation damage in EOR applications.[476–478] Another unresolved topic concerning foam-EOR is the evolution of foam rheology as it propagates through heterogeneous porous media in the presence of oil. This process is influenced by foam generation (snap-off, lamellae division, leave-behind, and pinch-off) and decay (coarsening, rupture, and capillary/gravity drainage) rates that directly affect foam velocity and texture, both of which are critical parameters for determining foam viscosity.[27,305,347,479]

The storage of hydrogen in underground reservoirs to balance energy demand has shown significant potential in alleviating dependence on fossil fuels.[411] The investigations in pore-scale level of UHS using microfluidics are relatively rare, compared to CCUS and EOR. Microfluidic experiments have highlighted many associated challenges, particularly in understanding fluid dynamics in subsurface environments.[414–417] Both biological and geological effects[411] and foam-assisted flow[422] have shown great influence on the viability of the UHS system; however, many aspects of these topics remain unresolved and are important for future

microfluidic research. Factors such as trapping mechanisms, gas connectivity, wettability, and the hysteresis effect of cyclic injection and withdrawal cycles unique to UHS influence the system capacity and efficiency, which also require further investigations.

The long-term stability of hydrogen in underground formations remains in question. Hydrogen loss can occur through many pathways, including dissolution into the liquid phase, microbial/mineral reactions due to its highly reactive nature, as well as leakage attributed to its small molecule size. Despite being rarely discussed in the literature, the encapsulation of hydrogen in foam has been shown to increase the storage efficiency[422] and could serve as a protective/sealing barrier to minimize hydrogen loss during storage. This promising approach requires future exploration using microfluidics.

In core flooding experiments, microscopic sealing imperfections in the core holder often lead to the escape of hydrogen gas, introducing experimental artifacts that compromise the accuracy of diffusion measurements.[480] Microfluidic chips with reliable bonding techniques can offer a more precise and controlled environment for studying hydrogen diffusion. Moreover, the study of bacteria using microfluidics can provide better insight into biological interactions with stored gas. In contrast to hydrogen consumption, exploring possible bacterial reactions that promote hydrogen generation, such as dark fermentation of wastewater, could be beneficial. Such experiments typically require extended periods (days) for bacterial growth in the microfluidic devices[429] and are time-consuming. The integration of machine learning algorithms may be leveraged to shorten these processes. For instance, intelligent microfluidics,[169] transfer learning from prototyped chips,[164] chip geometry design,[163] performance prediction/optimization,[167,168] and temporal evolution forecasting by transformer neural networks can further enhance experimental efficiency and accuracy.

Author contributions

Junyi Yang: conceptualization; writing – original draft; visualization. Nikoo Moradpour: conceptualization; writing – original draft; visualization. Lap Au-Yeung: conceptualization; writing – original draft; visualization. Peichun Amy Tsai: conceptualization; writing – review & editing; visualization; supervision; funding acquisition.

Conflicts of interest

There are no conflicts to declare.

Data availability

No primary research results, software or code have been included and no new data were generated or analyzed as part of this review.

Acknowledgements

We gratefully acknowledge the support from the Canada First Research Excellence Fund (CFREF), Future Energy System (FES T02-P05 CCUS projects) at the University of Alberta, and Canada Foundation for Innovation (CFI 34546). P. A. T. holds a Canada Research Chair (CRC) in Fluids and Interfaces and gratefully acknowledges funding from the Natural Sciences and Engineering Research Council of Canada (NSERC) and Alberta Innovates (AI), in particular the NSERC Canada Research Chairs Program (CRC 233147) and Discovery Grant (RGPIN-2020-05511). J. Y. acknowledges the support of the Graduate Student Scholarship program from Alberta Innovates (AI) and from the Future Energy System Legacy Builders Program (FES-LBP). We thank Dr. Amin Alinejad for his constructive suggestions.

Notes and references

1 NASA's Goddard Institute for Space Studies (GISS), Global Temperature GLOBAL LAND-OCEAN TEMPERATURE INDEX, https://climate.nasa.gov/vital-signs/global-temperature/?intent=121, Accessed: 2025-01-27.
2 S. S. Datta, I. Battiato, M. A. Fernø, R. Juanes, S. Parsa, V. Prigiobbe, E. Santanach-Carreras, W. Song, S. L. Biswal and D. Sinton, *Lab Chip*, 2023, **23**, 1358–1375.
3 D. Y. Leung, G. Caramanna and M. M. Maroto-Valer, *Renewable Sustainable Energy Rev.*, 2014, **39**, 426–443.
4 E. Adu, Y. Zhang and D. Liu, *Can. J. Chem. Eng.*, 2019, **97**, 1048–1076.
5 M. Bui, C. S. Adjiman, A. Bardow, E. J. Anthony, A. Boston, S. Brown, P. S. Fennell, S. Fuss, A. Galindo, L. A. Hackett, J. P. Hallett, H. J. Herzog, G. Jackson, J. Kemper, S. Krevor, G. C. Maitland, M. Matuszewski, I. S. Metcalfe, C. Petit, G. Puxty, J. Reimer, D. M. Reiner, E. S. Rubin, S. A. Scott, N. Shah, B. Smit, J. P. Trusler, P. Webley, J. Wilcox and N. Mac Dowell, *Energy Environ. Sci.*, 2018, **11**, 1062–1176.
6 I. Gomez Mendez, W. M. El-Sayed, A. H. Menefee and Z. T. Karpyn, *Energy Fuels*, 2024, **38**, 20015–20032.
7 V. A. Lifton, *Lab Chip*, 2016, **16**, 1777–1796.
8 A. Anbari, H. T. Chien, S. S. Datta, W. Deng, D. A. Weitz and J. Fan, *Small*, 2018, **14**, 1–15.
9 D. Sinton, *Lab Chip*, 2014, **14**, 3127–3134.
10 B. Bao, J. Riordon, F. Mostowfi and D. Sinton, *Lab Chip*, 2017, **17**, 2740–2759.
11 S. Gogoi and S. B. Gogoi, *J. Pet. Explor. Prod. Technol.*, 2019, **9**, 2263–2277.
12 A. Abedini, S. Ahitan, Z. Barikbin, V. Soni, J. Ratulowski and D. Sinton, *Energy Fuels*, 2022, **36**, 8578–8590.
13 D. Qin, Y. Xia, J. A. Rogers, R. J. Jackman, X.-M. Zhao and G. M. Whitesides, *Microsyst. Technol. Chem. Life Sci.*, Springer Verlag Berlin Heidelberg, 1998, pp. 1–20.
14 N. Convery and N. Gadegaard, *Micro Nano Eng.*, 2019, **2**, 76–91.

15 A. Chatenever, J. Calhoun and C. John, *JPT, J. Pet. Technol.*, 1952, **4**, 149–156.
16 R. Chuoke, P. van Meurs and C. van der Poel, *Trans. AIME*, 1959, **216**, 188–194.
17 J. Stokes, D. Weitz, J. P. Gollub, A. Dougherty, M. Robbins, P. Chaikin and H. Lindsay, *Phys. Rev. Lett.*, 1986, **57**, 1718.
18 R. Lenormand, E. Touboul and C. Zarcone, *J. Fluid Mech.*, 1988, **189**, 165–187.
19 S. Marre, A. Adamo, S. Basak, C. Aymonier and K. F. Jensen, *Ind. Eng. Chem. Res.*, 2010, **49**, 11310–11320.
20 S. Marre and K. F. Jensen, *Chem. Soc. Rev.*, 2010, **39**, 1183–1202.
21 W. Song and A. R. Kovscek, *Lab Chip*, 2015, **15**, 3314–3325.
22 Y. Q. Zhang, A. Sanati-Nezhad and S. H. Hejazi, *Lab Chip*, 2018, **18**, 285–295.
23 W. Wang, S. Chang and A. Gizzatov, *ACS Appl. Mater. Interfaces*, 2017, **9**, 29380–29386.
24 M. Nooraiepour, H. Fazeli, R. Miri and H. Hellevang, *Environ. Sci. Technol.*, 2018, **52**, 6050–6060.
25 J. Zhong, A. Abedini, L. Xu, Y. Xu, Z. Qi, F. Mostowfi and D. Sinton, *Nanoscale*, 2018, **10**, 21994–22002.
26 Y. Zhong, Q. Li, W. Gao, Y. Wen and Y. Zhang, *J. Rock Mech. Geotech. Eng.*, 2025, DOI: 10.1016/j.jrmge.2025.01.018, in press.
27 N. Moradpour, J. Yang and P. A. Tsai, *Curr. Opin. Colloid Interface Sci.*, 2024, 101845.
28 A. Kazan, *Microfluid. Nanofluid.*, 2022, **26**, 1–16.
29 J. Yang and P. A. Tsai, *Biomicrofluidics*, 2024, **18**, 051301.
30 G. M. Whitesides, *Nature*, 2006, **442**, 368–373.
31 E. K. Sackmann, A. L. Fulton and D. J. Beebe, *Nature*, 2014, **507**, 181–189.
32 S. Neethirajan, I. Kobayashi, M. Nakajima, D. Wu, S. Nandagopal and F. Lin, *Lab Chip*, 2011, **11**, 1574–1586.
33 K.-i. Ohno, K. Tachikawa and A. Manz, *J. Electrophor.*, 2008, **29**, 4443–4453.
34 V. A. Lifton, *Lab Chip*, 2016, **16**, 1777–1796.
35 S. Battat, D. A. Weitz and G. M. Whitesides, *Lab Chip*, 2022, **22**, 530–536.
36 J. Liu, Y. Zhang, M. Wei, X. He and B. Bai, *Energy Fuels*, 2022, **36**, 9904–9931.
37 P. N. Nge, C. I. Rogers and A. T. Woolley, *Chem. Rev.*, 2013, **113**, 2550–2583.
38 S. C. Terry, J. H. Herman and J. B. Angell, *IEEE Trans. Electron Devices*, 1979, **26**, 1880–1886.
39 A. de Mello, *Lab Chip*, 2002, **2**, 48N–54N.
40 E. Kim, Y. Xia and G. M. Whitesides, *Nature*, 1995, **376**, 581–584.
41 C. Marzolin, A. Terfort, J. Tien and G. M. Whitesides, *Thin Solid Films*, 1998, **315**, 9–12.
42 D. C. Duffy, J. C. McDonald, O. J. Schueller and G. M. Whitesides, *Anal. Chem.*, 1998, **70**, 4974–4984.
43 T. Trantidou, Y. Elani, E. Parsons and O. Ces, *Microsyst. Nanoeng.*, 2017, **3**, 1–9.
44 P. Occhetta, A. Mainardi, E. Votta, Q. Vallmajo-Martin, M. Ehrbar, I. Martin, A. Barbero and M. Rasponi, *Nat. Biomed. Eng.*, 2019, **3**, 545–557.
45 J. P. Esquivel, M. Castellarnau, T. Senn, B. Löchel, J. Samitier and N. Sabaté, *Lab Chip*, 2012, **12**, 74–79.
46 R. Singh, M. Sivaguru, G. A. Fried, B. W. Fouke, R. A. Sanford, M. Carrera and C. J. Werth, *J. Contam. Hydrol.*, 2017, **204**, 28–39.
47 P. Tabeling, *Introduction to microfluidics*, Oxford university press, 2023.
48 A. Waldbaur, H. Rapp, K. Länge and B. E. Rapp, *Anal. Methods*, 2011, **3**, 2681–2716.
49 J. Castillo-León and W. E. Svendsen, *Lab-on-a-Chip devices and micro-total analysis systems: a practical guide*, Springer, 2014.
50 J. C. McDonald, D. C. Duffy, J. R. Anderson, D. T. Chiu, H. Wu, O. J. Schueller and G. M. Whitesides, *J. Electrophor.*, 2000, **21**, 27–40.
51 N. Convery and N. Gadegaard, *Micro Nano Eng.*, 2019, **2**, 76–91.
52 E. Berthier, E. W. Young and D. Beebe, *Lab Chip*, 2012, **12**, 1224–1237.
53 P. Kim, K. W. Kwon, M. C. Park, S. H. Lee, S. M. Kim and K. Y. Suh, *BioChip*, 2008, **2**, 1–11.
54 S. S. Deshmukh and A. Goswami, *Mater. Today*, 2020, **26**, 405–414.
55 P. Mohanan, *Human Organs-on-a-Chip Technology*, Elsevier, 2024.
56 S. M. Scott and Z. Ali, *Micromachines*, 2021, **12**, 319.
57 Y. Xia and G. M. Whitesides, *Angew. Chem., Int. Ed.*, 1998, **37**, 550–575.
58 M. Wang, *Lithography*, BoD–Books on Demand, 2010.
59 C. A. Conn, K. Ma, G. J. Hirasaki and S. L. Biswal, *Lab Chip*, 2014, **14**, 3968–3977.
60 D. Qin, Y. Xia, A. J. Black and G. M. Whitesides, *J. Vac. Sci. Technol., B: Microelectron. Nanometer Struct.–Process., Meas., Phenom.*, 1998, **16**, 98–103.
61 S. N. Khonina, N. L. Kazanskiy and M. A. Butt, *Micromachines*, 2024, **15**, 1321.
62 K. Zhong, Y. Gao, F. Li, Z. Zhang and N. Luo, *Optik*, 2014, **125**, 2413–2416.
63 R. M. Guijt and M. C. Breadmore, *Lab Chip*, 2008, **8**, 1402–1404.
64 M. Villegas, Z. Cetinic, A. Shakeri and T. F. Didar, *Anal. Chim. Acta*, 2018, **1000**, 248–255.
65 G. C. Lisensky, D. J. Campbell, K. J. Beckman, C. E. Calderon, P. W. Doolan, R. M. Ottosen and A. B. Ellis, *J. Chem. Educ.*, 1999, **76**, 537.
66 P. R. Selvaganapathy, *Comprehensive Microsystems*, Elsevier, Oxford, 2008, pp. 75–105.
67 T. Bardelli, C. Marano and F. Briatico Vangosa, *J. Appl. Polym. Sci.*, 2021, **138**, 51013.
68 P. Seeharaj, P. Pasupong, E. Detsri and P. Damrongsak, *J. Mater. Sci.*, 2018, **53**, 4828–4839.
69 L. Li, B. Li, J. Dong and J. Zhang, *J. Mater. Chem. A*, 2016, **4**, 13677–13725.
70 J. C. McDonald and G. M. Whitesides, *Acc. Chem. Res.*, 2002, **35**, 491–499.

71 K. Raj M and S. Chakraborty, *J. Appl. Polym. Sci.*, 2020, **137**, 48958.
72 S. Bhattacharya, A. Datta, J. M. Berg and S. Gangopadhyay, *J. Microelectromech. Syst.*, 2005, **14**, 590–597.
73 E. Rubino and T. Ioppolo, *J. Polym. Sci., Part B: Polym. Phys.*, 2016, **54**, 747–751.
74 J. Zhou, A. V. Ellis and N. H. Voelcker, *J. Electrophor.*, 2010, **31**, 2–16.
75 J. Zhou, D. A. Khodakov, A. V. Ellis and N. H. Voelcker, *J. Electrophor.*, 2012, **33**, 89–104.
76 N. Verma, P. Prajapati, V. Singh and A. Pandya, *Prog. Mol. Biol. Transl. Sci.*, 2022, **186**, 1–14.
77 C. Rivet, H. Lee, A. Hirsch, S. Hamilton and H. Lu, *Chem. Eng. Sci.*, 2011, **66**, 1490–1507.
78 P. K. Rai, M. Islam and A. Gupta, *Sens. Actuators, A*, 2022, **347**, 113926.
79 E. Kjeang, N. Djilali and D. Sinton, *J. Power Sources*, 2009, **186**, 353–369.
80 K. Ma, R. Liontas, C. A. Conn, G. J. Hirasaki and S. L. Biswal, *Soft Matter*, 2012, **8**, 10669–10675.
81 S. Xiao, Y. Zeng, E. D. Vavra, P. He, M. Puerto, G. J. Hirasaki and S. L. Biswal, *Langmuir*, 2018, **34**, 739–749.
82 X. Pan, L. Sun, X. Huo, C. Feng and Z. Zhang, *Energies*, 2023, **16**, 7846.
83 A. Sell, H. Fadaei, M. Kim and D. Sinton, *Environ. Sci. Technol.*, 2013, **47**, 71–78.
84 T. H. M. Ho, J. Yang and P. A. Tsai, *Lab Chip*, 2021, **21**, 3942–3951.
85 Micronit, Enhanced Oil Recovery (EOR) chip - Physical Rock network, https://micronit.com/eor-chip-uncoated-physical-rock.html, Accessed: 2025-02-19.
86 uFluidix, Device Materials, https://www.ufluidix.com/device-materials/, Accessed: 2025-02-19.
87 C. Rein, M. Toner and D. Sevenler, *Sci. Rep.*, 2023, **13**, 1–9.
88 K. Michael, A. Golab, V. Shulakova, J. Ennis-King, G. Allinson, S. Sharma and T. Aiken, *Int. J. Greenhouse Gas Control*, 2010, **4**, 659–667.
89 S. Bachu, *Int. J. Greenhouse Gas Control*, 2016, **44**, 152–165.
90 J. Kobayashi, Y. Mori and S. Kobayashi, *Chem. Commun.*, 2005, 2567–2568.
91 F. Benito-Lopez, R. M. Tiggelaar, K. Salbut, J. Huskens, R. J. Egberink, D. N. Reinhoudt, H. J. Gardeniers and W. Verboom, *Lab Chip*, 2007, **7**, 1345–1351.
92 R. M. Tiggelaar, F. Benito-López, D. C. Hermes, H. Rathgen, R. J. Egberink, F. G. Mugele, D. N. Reinhoudt, A. van den Berg, W. Verboom and H. J. Gardeniers, *Chem. Eng. J.*, 2007, **131**, 163–170.
93 N. M. P. da Silva, J. J. Letourneau, F. Espitalier and L. Prat, *Chem. Eng. Technol.*, 2014, **37**, 1929–1937.
94 T. Gothsch, C. Schilcher, C. Richter, S. Beinert, A. Dietzel, S. Büttgenbach and A. Kwade, *Microfluid. Nanofluid.*, 2015, **18**, 121–130.
95 A. Martin, S. Teychené, S. Camy and J. Aubin, *Microfluid. Nanofluid.*, 2016, **20**, 1–8.
96 N. Qin, J. Z. Wen and C. L. Ren, *Phys. Rev. E*, 2017, **95**, 1–15.
97 R. F. Gerhardt, A. J. Peretzki, S. K. Piendl and D. Belder, *Anal. Chem.*, 2017, **89**, 13030–13037.
98 Z. B. Qi, L. Xu, Y. Xu, J. Zhong, A. Abedini, X. Cheng and D. Sinton, *Lab Chip*, 2018, **18**, 3872–3880.
99 T. H. M. Ho, D. Sameoto and P. A. Tsai, *Chem. Eng. Res. Des.*, 2021, **174**, 116–126.
100 J. Yang and P. A. Tsai, *Chem. Eng. Sci.*, 2024, **300**, 120543.
101 C. Matellan and A. E. Del Río Hernández, *Sci. Rep.*, 2018, **8**, 1–13.
102 E. Sollier, C. Murray, P. Maoddi and D. Di Carlo, *Lab Chip*, 2011, **11**, 3752–3765.
103 K. T. L. Trinh, D. A. Thai, W. R. Chae and N. Y. Lee, *ACS Omega*, 2020, **5**, 17396–17404.
104 R. Beaudry, Deep Reactive Ion Etching, *US Pat.*, 2009/0242512 A1, 2009.
105 D. I. Fomerantz, Anodic Bonding, *US Pat.*, 3397278, 1968.
106 G. Wallis and D. I. Fomerantz, *J. Appl. Phys.*, 1969, **40**, 3946–3949.
107 K. M. Knowles and A. T. Van Helvoort, *Int. Mater. Rev.*, 2006, **51**, 273–311.
108 G. A. Spierings, *J. Mater. Sci.*, 1993, **28**, 6261–6273.
109 J. A. Dziuban, *Bonding in Microsystem Technology*, Springer Dordrecht, 2006.
110 A. Mathur, S. S. Roy, M. Tweedie, S. Mukhopadhyay, S. K. Mitra and J. A. McLaughlin, *Curr. Appl. Phys.*, 2009, **9**, 1199–1202.
111 J. Peden and M. Husain, SPE Annual Technical Conference and Exhibition?, 1985, p. SPE-14307.
112 M. McKellar and N. Wardlaw, *J. Can. Pet. Technol.*, 1982, **21**, 39–41.
113 S.-W. Jeong, M. Y. Corapcioglu and S. E. Roosevelt, *Environ. Sci. Technol.*, 2000, **34**, 3456–3461.
114 N. C. Wardlaw and L. Yu, *Transp. Porous Media*, 1988, **3**, 17–34.
115 T. W. Willingham, C. J. Werth and A. J. Valocchi, *Environ. Sci. Technol.*, 2008, **42**, 3185–3193.
116 T. H. M. Ho and P. A. Tsai, *Lab Chip*, 2020, **20**, 3806–3814.
117 X. Zheng, N. Mahabadi, T. S. Yun and J. Jang, *J. Geophys. Res.: Solid Earth*, 2017, **122**, 1634–1647.
118 X. Pan, L. Sun, Q. Liu, X. Huo, F. Chen, Y. Wang, C. Feng, Z. Zhang and S. Ni, *Nanoscale*, 2025, **17**, 1524–1535.
119 B. Géraud, S. A. Jones, I. Cantat, B. Dollet and Y. Méheust, *Water Resour. Res.*, 2016, **52**, 773–790.
120 Y. Zhou, C. Yao, J. Zhu, H. Xu, Y. Song and J. Zhao, *Geoenergy Sci. Eng.*, 2025, 214118.
121 N. Moradpour and P. A. Tsai, *Lab Chip*, 2025, **25**(22), 5976–5992.
122 Q.-A. Da, C.-J. Yao, X. Zhang, X.-P. Wang, X.-H. Qu and G.-L. Lei, *Pet. Sci.*, 2022, **19**, 1745–1756.
123 Q. Lv, R. Zheng, T. Zhou, X. Guo, W. Wang, J. Li and Z. Liu, *Fuel*, 2022, **330**, 125533.
124 K. Xu, T. Liang, P. Zhu, P. Qi, J. Lu, C. Huh and M. Balhoff, *Lab Chip*, 2017, **17**, 640–646.
125 G.-y. Li, L.-t. Zhan, Y.-m. Chen, S. Feng, Z.-h. Zhang and X.-l. Du, *Can. Geotech. J.*, 2022, **60**, 902–916.
126 D. S. Park, S. Bou-Mikael, S. King, K. E. Thompson, C. S. Willson and D. E. Nikitopoulos, ASME International

Mechanical Engineering Congress and Exposition, 2012, pp. 709–715.
127 W. Yun, C. M. Ross, S. Roman and A. R. Kovscek, *Lab Chip*, 2017, **17**, 1462–1474.
128 C. L. Gaol, J. Wegner and L. Ganzer, *Lab Chip*, 2020, **20**, 2197–2208.
129 A. Gerami, P. Mostaghimi, R. T. Armstrong, A. Zamani and M. E. Warkiani, *Int. J. Coal Geol.*, 2016, **159**, 183–193.
130 L. Zuo, C. Zhang, R. W. Falta and S. M. Benson, *Adv. Water Resour.*, 2013, **53**, 188–197.
131 W. Wang, Y. Peng, Z. Chen, H. Liu, J. Fan and Y. Liu, *Energy Fuels*, 2022, **36**, 7402–7413.
132 S. Heidari, M. Ahmadi, F. Esmaeilzadeh and D. Mowla, *J. Pet. Explor. Prod. Technol.*, 2019, **9**, 2309–2317.
133 M. M. Almajid and A. R. Kovscek, *Adv. Colloid Interface Sci.*, 2016, **233**, 65–82.
134 M. L. Porter, J. Jiménez-Martínez, R. Martinez, Q. McCulloch, J. W. Carey and H. S. Viswanathan, *Lab Chip*, 2015, **15**, 4044–4053.
135 P. A. Godoy, A. Orujov, A. P. Gramatges and S. A. Aryana, *Lab Chip*, 2025, **25**, 3109–3122.
136 N. S. K. Gunda, B. Bera, N. K. Karadimitriou, S. K. Mitra and S. M. Hassanizadeh, *Lab Chip*, 2011, **11**, 3785–3792.
137 W. Lei, T. Liu, C. Xie, H. Yang, T. Wu and M. Wang, *Energy Sci. Eng.*, 2020, **8**, 986–998.
138 W. Song, T. W. de Haas, H. Fadaei and D. Sinton, *Lab Chip*, 2014, **14**, 4382–4390.
139 A. Gerami, R. T. Armstrong, B. Johnston, M. E. Warkiani, N. Mosavat and P. Mostaghimi, *Energy Fuels*, 2017, **31**, 10393–10403.
140 B. Yuan and D. A. Wood, *J. Pet. Sci. Eng.*, 2018, **167**, 287–299.
141 A. Jahanbakhsh, K. L. Wlodarczyk, D. P. Hand, R. R. Maier and M. M. Maroto-Valer, *Sensors*, 2020, **20**, 1–63.
142 Y. A. Alzahid, P. Mostaghimi, A. Gerami, A. Singh, K. Privat, T. Amirian and R. T. Armstrong, *Sci. Rep.*, 2018, **8**, 15518.
143 A. Anbari, H.-T. Chien, S. S. Datta, W. Deng, D. A. Weitz and J. Fan, *Small*, 2018, **14**, 1703575.
144 F. Rezaeiakmal and R. Parsaei, *J. Pet. Sci. Eng.*, 2021, **203**, 108583.
145 J. Upadhyay, D. S. Park, K. E. Thompson and D. E. Nikitopoulos, ASME International Mechanical Engineering Congress and Exposition, 2015, p. V07BT09A004.
146 A. T. Krummel, S. S. Datta, S. Münster and D. A. Weitz, *AIChE J.*, 2013, **59**, 1022–1029.
147 S. S. Datta, J.-B. Dupin and D. A. Weitz, *Phys. Fluids*, 2014, **26**, 062004.
148 Y. Zhang, J. Geng, J. Liu, B. Bai, X. He, M. Wei and W. Deng, *Langmuir*, 2021, **37**, 13353–13364.
149 L. Kong, S. Ishutov, F. Hasiuk and C. Xu, *SPE Reservoir Eval. Eng.*, 2021, **24**, 721–732.
150 D. Lee, M. Ruf, N. Karadimitriou, H. Steeb, M. Manousidaki, E. A. Varouchakis, S. Tzortzakis and A. Yiotis, *Sci. Rep.*, 2024, **14**, 9375.
151 S. S. Datta, H. Chiang, T. S. Ramakrishnan and D. A. Weitz, *Phys. Rev. Lett.*, 2013, **111**, 1–5.
152 J. Jansen, F. Melchels, D. Grijpma and J. Feijen, *Biomacromolecules*, 2009, **10**, 214–220.
153 A. Scanziani, K. Singh, H. Menke, B. Bijeljic and M. J. Blunt, *Appl. Energy*, 2020, **259**, 114136.
154 Y. Zhao, Y. Song, Y. Liu, L. Jiang and N. Zhu, *Pet. Sci.*, 2011, **13**, 183–193.
155 P. Nguyen, H. Fadaei and D. Sinton, *Energy Fuels*, 2014, **28**, 6221–6227.
156 D. Wildenschild and A. P. Sheppard, *Adv. Water Resour.*, 2013, **51**, 217–246.
157 M. Andrew, H. Menke, M. J. Blunt and B. Bijeljic, *Transp. Porous Media*, 2015, **110**, 1–24.
158 X. Deng, X. Zhou, S. Patil, R. Al-Abdrabalnabi, S. Khan, M. S. Aljawad, M. Mahmoud, M. Abdurrahman and M. S. Kamal, *Energy Fuels*, 2023, **37**, 16311–16332.
159 A. L. Herring, L. Andersson, D. L. Newell, J. W. Carey and D. Wildenschild, *Int. J. Greenhouse Gas Control*, 2014, **25**, 93–101.
160 M. Voltolini, T. H. Kwon and J. Ajo-Franklin, *Int. J. Greenhouse Gas Control*, 2017, **66**, 230–245.
161 Y. Tang, C. Hou, Y. He, Y. Wang, Y. Chen and Z. Rui, *Energy Technol.*, 2021, **9**, 1–21.
162 P. Zhou, H. He, H. Ma, S. Wang and S. Hu, *Micromachines*, 2022, **13**, 274.
163 M. Delpisheh, B. Ebrahimpour, A. Fattahi, M. Siavashi, H. Mir, H. Mashhadimoslem, M. A. Abdol, M. Ghorbani, J. Shokri and D. Niblett, *et al.*, *J. Mater. Chem. A*, 2024, **12**, 20717–20782.
164 D. McIntyre, A. Lashkaripour, P. Fordyce and D. Densmore, *Lab Chip*, 2022, **22**, 2925–2937.
165 J. Zheng, T. Cole, Y. Zhang, J. Kim and S.-Y. Tang, *Biosens. Bioelectron.*, 2021, **194**, 113666.
166 S. Srikanth, S. K. Dubey, A. Javed and S. Goel, *Sens. Actuators, A*, 2021, **332**, 113096.
167 G. Antonelli, J. Filippi, M. D'Orazio, G. Curci, P. Casti, A. Mencattini and E. Martinelli, *Biosens. Bioelectron.*, 2024, 116632.
168 F. Ahmadi, M. Simchi, J. M. Perry, S. Frenette, H. Benali, J.-P. Soucy, G. Massarweh and S. C. Shih, *Lab Chip*, 2023, **23**, 81–91.
169 E. A. Galan, H. Zhao, X. Wang, Q. Dai, W. T. Huck and S. Ma, *Matter*, 2020, **3**, 1893–1922.
170 A. Lashkaripour, C. Rodriguez, N. Mehdipour, R. Mardian, D. McIntyre, L. Ortiz, J. Campbell and D. Densmore, *Nat. Commun.*, 2021, **12**, 25.
171 H. Song, C. Liu, J. Lao, J. Wang, S. Du and M. Yu, *Geofluids*, 2021, **2021**, 1194186.
172 X. Qi, Y. Wei, S. Wang, Z. Wang and M. Zhou, *Processes*, 2024, **12**, 2306.
173 S. Liu, A. Zolfaghari, S. Sattarin, A. K. Dahaghi and S. Negahban, *J. Pet. Sci. Eng.*, 2019, **180**, 445–455.
174 A. Kasha, A. Sakhaee-Pour and I. Hussein, *SPE Reservoir Eval. Eng.*, 2022, **25**, 1–20.
175 R. Khosravi, M. Simjoo and M. Chahardowli, *Sci. Rep.*, 2024, **14**, 13213.

176 K. Manikonda, A. R. Hasan, C. E. Obi, R. Islam, A. K. Sleiti, M. W. Abdelrazeq and M. A. Rahman, Abu Dhabi International Petroleum Exhibition and Conference, 2021, p. D041S121R004.
177 D. Zhao, J. Hou, B. Wei, H. Liu, Q. Du, Y. Zhang and Z. Sun, *Phys. Fluids*, 2023, **35**, 083312.
178 A. Massimiani, F. Panini, S. L. Marasso, N. Vasile, M. Quaglio, C. Coti, D. Barbieri, F. Verga, C. F. Pirri and D. Viberti, *Micromachines*, 2023, **14**, 308.
179 N. Berghout, Putting CO2 to Use, creating value from emissions, International energy agency technical report, 2019.
180 Y. Cheraghi, S. Kord and V. Mashayekhizadeh, *Neural Comput. Appl.*, 2023, **35**, 17077–17094.
181 C. McGlade, G. Sondak and M. Han, Whatever happened to enhanced oil recovery?, International energy agency technical report, 2018.
182 M. M. A. Awan and F. U. D. Kirmani, *Pet. Res.*, 2025, **10**(1), 129–136.
183 G. C. Institute, GLOBAL STATUS OF CCS 2024, collaborating for a net-zero future, Global carbon capture and storage institute technical report, 2024.
184 S. Sayegh and D. Fisher, *J. Can. Pet. Technol.*, 2009, **48**, 30–36.
185 M. Robin, J. Behot and V. Sygouni, SPE Improved Oil Recovery Conference, 2012, p. SPE-154165.
186 X. Wang and Y. Gu, *Ind. Eng. Chem. Res.*, 2011, **50**, 2388–2399.
187 M. Cao and Y. Gu, *Fuel*, 2013, **109**, 157–166.
188 N. Moradpour, P. Pourafshary and D. Zivar, *J. Pet. Sci. Eng.*, 2021, **202**, 108562.
189 Z.-x. Liu, Y. Liang, Q. Wang, Y.-j. Guo, M. Gao, Z.-b. Wang and W.-l. Liu, *J. Pet. Sci. Eng.*, 2020, **193**, 107449.
190 S. Ghedan, SPE Reservoir Characterisation and Simulation Conference and Exhibition, 2009, p. SPE-125581.
191 N. Zhang, M. Wei and B. Bai, *Fuel*, 2018, **220**, 89–100.
192 F. Gozalpour, S. R. Ren and B. Tohidi, *Oil Gas Sci. Technol.*, 2005, **60**, 537–546.
193 M. Riazi, M. Sohrabi and M. Jamiolahmady, *Transp. Porous Media*, 2011, **86**, 73–86.
194 L. Wang, Y. He, Q. Wang, M. Liu and X. Jin, *Fuel*, 2020, **282**, 118689.
195 Z. Chen, L. Li, Y. Su, J. Liu, Y. Hao and X. Zhang, *Fuel*, 2024, **368**, 131595.
196 C. Qian, Z. Rui, Y. Liu, K. Zhou, K. Du, Y. Zhao, J. Zou, K. Song and X. Li, *J. Chem. Eng.*, 2025, **505**, 159135.
197 Z. Chen, Y. Zhou and H. Li, *Ind. Eng. Chem. Res.*, 2022, **61**, 10298–10318.
198 A. Sharbatian, A. Abedini, Z. Qi and D. Sinton, *Anal. Chem.*, 2018, **90**, 2461–2467.
199 B. Bao, J. Feng, J. Qiu and S. Zhao, *ACS Omega*, 2021, **6**, 943–953.
200 J. Shi, L. Tao, Y. Guo, X. He, Y. Li and B. Bao, *Fuel*, 2024, **362**, 130876.
201 X. Zhang, L. Li, Y. Su, Q. Da, J. Fu, R. Wang and F. Chen, *Appl. Energy*, 2023, **348**, 121518.
202 L. Tao, W. Liu, J. Shi, Y. Guo, W. Qin and B. Bao, *Chem. Eng. Sci.*, 2025, **302**, 120828.
203 P. Nguyen, D. Mohaddes, J. Riordon, H. Fadaei, P. Lele and D. Sinton, *Anal. Chem.*, 2015, **87**, 3160–3164.
204 F. Ungar, S. Ahitan, S. Worthing, A. Abedini, K. Uleberg and T. Yang, *J. Pet. Sci. Eng.*, 2022, **208**, 109415.
205 D. Pereponov, M. Tarkhov, D. B. Dorhjie, A. Rykov, I. Filippov, E. Zenova, V. Krutko, A. Cheremisin and E. Shilov, *Energies*, 2023, **16**, 4994.
206 H. Zou, A. C. Slim and A. Neild, *Anal. Chem.*, 2019, **91**, 13681–13687.
207 H. Zou, H. Kang, A. C. Slim and A. Neild, *Lab Chip*, 2020, **20**, 3582–3590.
208 X. Zhang, L. Li, Q. Da, Y. Su, S. Ma and Z. Zhu, *J. Environ. Chem. Eng.*, 2022, **10**, 109036.
209 X. Zhang, Y. Su, L. Li, Q. Da, Y. Hao, W. Wang, J. Liu, X. Gao, A. Zhao and K. Wang, *Energy*, 2022, **248**, 123649.
210 Y. Hao, Z. Li, Y. Su, C. Kong, H. Chen and Y. Meng, *Energy*, 2022, **254**, 124349.
211 S. Yu, L. Yiqiang, Q. Huan, C. Jinxin and T. Xuechen, *Energy Procedia*, 2025, **53**, 11507.
212 Y. Guo, F. Liu, J. Qiu, Z. Xu and B. Bao, *Energy*, 2022, **256**, 124524.
213 P. Nguyen, J. W. Carey, H. S. Viswanathan and M. Porter, *Appl. Energy*, 2018, **230**, 160–174.
214 R. Xu, R. Li, F. Huang and P. Jiang, *Sci. Bull.*, 2017, **62**, 795–803.
215 M. Zhang, B. Li, W. Lei, X. Zhao, W. Ding, X. Zhang, Y. Xin and Z. Li, *Fuel*, 2024, **371**, 132026.
216 F. Huang, R. Xu, P. Jiang, C. Wang, H. Wang and Z. Lun, *Phys. Fluids*, 2020, **32**, 092011.
217 Y. Guo, J. Shi, J. Qiu, Z. Xu and B. Bao, *Fuel*, 2023, **354**, 129344.
218 X. Zheng, N. Mahabadi, T. S. Yun and J. Jang, *J. Geophys. Res.: Solid Earth*, 2017, **122**, 1634–1647.
219 M. J. Shojaei, A. R. De Castro, Y. Méheust and N. Shokri, *J. Colloid Interface Sci.*, 2019, **552**, 464–475.
220 A. Gizzatov, S. Pierobon, Z. AlYousef, G. Jian, X. Fan, A. Abedini and A. I. Abdel-Fattah, *Sci. Rep.*, 2021, **11**, 3360.
221 X. Su and X.-a. Yue, *J. Pet. Sci. Eng.*, 2020, **195**, 107891.
222 M. G. Rezk, J. Foroozesh, D. Zivar and M. Mumtaz, *J. Nat. Gas Sci. Eng.*, 2019, **66**, 233–243.
223 Z. Song, Y. Li, Y. Song, B. Bai, J. Hou, K. Song, A. Jiang and S. Su, SPE Asia Pacific Oil and Gas Conference and Exhibition, 2020, p. D011S005R002.
224 Y. Sugai, T. Babadagli and K. Sasaki, *J. Pet. Explor. Prod. Technol.*, 2014, **4**, 105–112.
225 M. Seyyedattar, A. Ghamartale, S. Zendehboudi and S. Butt, *J. Mol. Liq.*, 2023, **379**, 121582.
226 A. Abedini and F. Torabi, *Ind. Eng. Chem. Res.*, 2013, **52**, 15211–15223.
227 I. Chatzis, A. Kantzas and F. A. Dullien, 63rd Annu. Tech. Conf. Exhib. Soc. Pet. Eng., Houston, TX, 1988, pp. 223–234.

228 S. Ayatollahi, F. Boukadi, M. Wadhahi, R. Maamari and A. Bemani, SPE Middle East Oil Gas Show Conf. MEOS, Proc., 2005, pp. 1119–1124.
229 M. Seyyedi and M. Sohrabi, *Ind. Eng. Chem. Res.*, 2018, **57**, 11617–11624.
230 P. E. Oren and W. Val Pinczewski, *SPE Form. Eval.*, 1994, **9**, 149–156.
231 C. Grattoni, M. P. Almada and R. Dawe, SPE Latin America and Caribbean Petroleum Engineering Conference, 1997, p. SPE-39032.
232 C. Esene, N. Rezaei, A. Aborig and S. Zendehboudi, *Fuel*, 2019, **237**, 1086–1107.
233 S. Mahdavi and L. A. James, *Fuel*, 2019, **257**, 115916.
234 T. Jamshidi, F. Zeng, P. Tontiwachwuthikul and F. Torabi, *Fuel*, 2019, **249**, 286–293.
235 M. Riazi, M. Sohrabi, C. Bernstone, M. Jamiolahmady and S. Ireland, *Chem. Eng. Res. Des.*, 2011, **89**, 1827–1840.
236 G.-T. Fu, Z.-G. Zheng, Y.-Q. Zhang, Y.-T. Dai, D.-C. Li, J. Zhan, C.-N. Gao and L.-W. Fan, *Energy Fuels*, 2024, **38**, 23433–23446.
237 H. Samara, M. Al-Eryani and P. Jaeger, *Fuel*, 2022, **323**, 124271.
238 S. Rudyk, P. Spirov, P. Samuel and S. J. Joshi, *Energy Fuels*, 2017, **31**, 6274–6283.
239 Y. Tang, C. Hou, Y. He, J. Tang, Y. Wang and J. Qin, *Transp. Porous Media*, 2023, **149**, 117–145.
240 C. Whitson and M. Brule, *Phase Behavior*, Society of Petroleum Engineers Inc., 1999, vol. 20.
241 B. Dindoruk, R. Johns and F. M. Orr, *SPE Reserv. Eval. Eng.*, 2021, **24**, 367–389.
242 W. F. Yellig and R. S. Metcalfe, *JPT, J. Pet. Technol.*, 1980, **32**, 160–168.
243 G. Song, Y. Meng, C. Zhang, Z. Zhao and Q. Yang, *ACS Omega*, 2024, **9**, 14747–14765.
244 D. N. Rao, *Fluid Phase Equilib.*, 1997, **139**, 311–324.
245 S. C. Ayirala and D. N. Rao, *SPE/DOE Symposium on Improved Oil Recovery*, April 2006, SPE-99606-MS.
246 R. L. Christiansen and H. K. Haines, *SPE Reservoir Eng.*, 1987, **2**, 523–527.
247 K. Zhang, N. Jia, F. Zeng, S. Li and L. Liu, *J. Pet. Sci. Eng.*, 2019, **183**, 106366.
248 Y. Gu, P. Hou and W. Luo, *J. Chem. Eng. Data*, 2013, **58**, 1361–1370.
249 X. Pan, L. Sun, F. Chen, X. Huo, Y. Wang, C. Feng, X. Zheng and Z. Zhang, *Energy Fuels*, 2024, **38**, 10904–10913.
250 W. Song, H. Fadaei and D. Sinton, *Environ. Sci. Technol.*, 2014, **48**, 3567–3574.
251 S. Molla, L. Magro and F. Mostowfi, *Lab Chip*, 2016, **16**, 3795–3803.
252 M. Seyyedi and M. Sohrabi, *Transp. Porous Media*, 2020, **134**, 331–349.
253 A. Zick, 61 st Annu. Tech. Conf. Exhib. Soc. Pet. Eng., 1986, p. 15493.
254 F. I. Stalkup, 62nd Annu. Tech. Conf. Exhib. Soc. Pet. Eng., 1987, p. 16715.
255 M. Sohrabi, A. Danesh, D. H. Tehrani and M. Jamiolahmady, *Transp. Porous Media*, 2008, **72**, 351–367.
256 A. Alinejad and H. Dehghanpour, *Fuel*, 2024, **359**, 130387.
257 A. Alinejad, J. Behseresht and H. Dehghanpour, *SPE J.*, 2025, **30**, 251–271.
258 F. Torabi, A. Qazvini Firouz, A. Kavousi and K. Asghari, *Fuel*, 2012, **93**, 443–453.
259 A. Abedini and F. Torabi, *Energy Fuels*, 2014, **28**, 774–784.
260 X. Zhou, Q. Yuan, X. Peng, F. Zeng and L. Zhang, *Fuel*, 2018, **215**, 813–824.
261 Q. Sun, Z. Li, J. Wang, S. Li, L. Jiang and C. Zhang, *RSC Adv.*, 2015, **5**, 67676–67689.
262 N. Lima, S. Parsa, S. Paciornik and M. S. Carvalho, *Sci. Rep.*, 2023, **13**, 21802.
263 X. Shen, L. Zhao, Y. Ding, B. Liu, H. Zeng, L. Zhong and X. Li, *J. Hazard. Mater.*, 2011, **186**, 1773–1780.
264 R. Aranda, H. Davarzani, S. Colombano, F. Laurent and H. Bertin, *Transp. Porous Media*, 2020, **134**, 231–247.
265 A. Karthick, B. Roy and P. Chattopadhyay, *J. Environ. Manage.*, 2019, **243**, 187–205.
266 J. Maire, E. Brunol and N. Fatin-Rouge, *Chemosphere*, 2018, **197**, 661–669.
267 W. R. Rossen, R. Farajzadeh, G. J. Hirasaki and M. Amirmoshiri, SPE Improved Oil Recovery Conference, 2022, p. D021S014R001.
268 J. A. Clark and E. E. Santiso, *Engineering*, 2018, **4**, 336–342.
269 W. Wanniarachchi, P. Ranjith, M. Perera, T. Rathnaweera, D. Zhang and C. Zhang, *Eng. Fract. Mech.*, 2018, **194**, 117–135.
270 S. Tong, R. Singh and K. K. Mohanty, *J. Nat. Gas Sci. Eng.*, 2018, **52**, 235–247.
271 S. Tong, M. Gu, R. Singh and K. K. Mohanty, *J. Pet. Sci. Eng.*, 2019, **182**, 106279.
272 S. H. Talebian, R. Masoudi, I. M. Tan and P. L. J. Zitha, *J. Pet. Sci. Eng.*, 2014, **120**, 202–215.
273 G. Jian, C. A. Fernandez, M. Puerto, R. Sarathi, A. Bonneville and S. L. Biswal, *J. Pet. Sci. Eng.*, 2021, **202**, 108447.
274 R. Phukan, S. B. Gogoi and P. Tiwari, *Colloids Surf., A*, 2020, **597**, 124799.
275 A. Shokrollahi, M. H. Ghazanfari and A. Badakhshan, *Can. J. Chem. Eng.*, 2014, **92**, 1975–1987.
276 W. Yun, S. Chang, D. A. Cogswell, S. L. Eichmann, A. Gizzatov, G. Thomas, N. Al-Hazza, A. Abdel-Fattah and W. Wang, *Sci. Rep.*, 2020, **10**, 782.
277 K. R. Chaturvedi and T. Sharma, *Chem. Eng. Sci.*, 2021, **235**, 116484.
278 K. Zhang, S. Li and L. Liu, *Fuel*, 2020, **267**, 117099.
279 N. Moradpour, R. Azadi and P. A. Tsai, *Colloids Surf., A*, 2025, **705**, 135533.
280 K. Osei-Bonsu, N. Shokri and P. Grassia, *J. Colloid Interface Sci.*, 2016, **462**, 288–296.
281 M. J. Shojaei, K. Osei-Bonsu, S. Richman, P. Grassia and N. Shokri, *Ind. Eng. Chem. Res.*, 2018, **58**, 1068–1074.

282 S. Alexander, A. R. Barron, N. Denkov, P. Grassia, S. Kiani, M. Sagisaka, M. J. Shojaei and N. Shokri, *Ind. Eng. Chem. Res.*, 2021, **61**, 372–381.
283 S. E. Taher, H. A. Abderrahmane and E. W. Al-Shalabi, *Fuel*, 2022, **320**, 123884.
284 D.-X. Du, A. N. Beni, R. Farajzadeh and P. L. Zitha, *Ind. Eng. Chem. Res.*, 2008, **47**, 6298–6306.
285 M. Simjoo, Y. Dong, A. Andrianov, M. Talanana and P. Zitha, *Ind. Eng. Chem. Res.*, 2013, **52**, 6221–6233.
286 D. Du, Y. Li, D. Zhang, X. Dong, F. Wang and K. Chao, *Exp. Therm. Fluid Sci.*, 2019, **103**, 247–261.
287 D. Wang, J. Fan and Z. Xue, *Water Resour. Res.*, 2022, **58**, e2021WR031874.
288 S. Li, Q. Wang, K. Zhang and Z. Li, *Fuel*, 2020, **263**, 116648.
289 G. Shi, K. Tang, F. Wang, Q. Luo, L. Bai, P. Sun and D. Zhu, *Energy Fuels*, 2020, **35**, 465–472.
290 P. Liu, X. Zhang, Y. Wu and X. Li, *J. Pet. Sci. Eng.*, 2017, **150**, 208–216.
291 N. Moradpour, M. Karimova, P. Pourafshary and D. Zivar, *ACS Omega*, 2020, **5**, 18155–18167.
292 E. Vavra, M. Puerto, S. L. Biswal and G. J. Hirasaki, *Sci. Rep.*, 2020, **10**, 12930.
293 A. Telmadarreie and J. J. Trivedi, *Transp. Porous Media*, 2016, **113**, 717–733.
294 N. Pal, X. Zhang, M. Ali, A. Mandal and H. Hoteit, *Fuel*, 2022, **315**, 122947.
295 W. Yu, X. Zhou and M. Y. Kanj, *Langmuir*, 2022, **38**, 2895–2905.
296 Z. Huang, M. Su, Q. Yang, Z. Li, S. Chen, Y. Li, X. Zhou, F. Li and Y. Song, *Nat. Commun.*, 2017, **7**, 1–9.
297 J. Zhao, F. Torabi and J. Yang, *Fuel*, 2021, **287**, 119443.
298 N. Yekeen, M. A. Manan, A. K. Idris, A. M. Samin and A. R. Risal, *J. Pet. Sci. Eng.*, 2017, **159**, 115–134.
299 Y. Wang, M. Puerto, C. Bai, K. Ma, K. Mateen, G. J. Hirasaki and S. L. Biswal, *Ind. Eng. Chem. Res.*, 2025, **64**, 2995–3003.
300 T. Muther, H. A. Qureshi, F. I. Syed, H. Aziz, A. Siyal, A. K. Dahaghi and S. Negahban, *J. Pet. Explor. Prod. Technol.*, 2022, **12**, 1463–1488.
301 R. Santos, W. Loh, A. Bannwart and O. Trevisan, *Braz. J. Chem. Eng.*, 2014, **31**, 571–590.
302 S. E. Quiñones-Cisneros, S. I. Andersen and J. Creek, *Energy Fuels*, 2005, **19**, 1314–1318.
303 A. Hinkle, E.-J. Shin, M. W. Liberatore, A. M. Herring and M. Batzle, *Fuel*, 2008, **87**, 3065–3070.
304 A. Kovscek, T. Patzek and C. Radke, *Chem. Eng. Sci.*, 1995, **50**, 3783–3799.
305 M. Lotfollahi, R. Farajzadeh, M. Delshad, A. Varavei and W. R. Rossen, SPE EOR Conference at Oil and Gas West Asia, 2016, p. D021S009R003.
306 Q. Xu and W. R. Rossen, *Colloids Surf., A*, 2003, **216**, 175–194.
307 H. Manikantan and T. M. Squires, *J. Fluid Mech.*, 2020, **892**, P1.
308 Y. Yu, B. F. García and S. Saraji, *J. Non-Newtonian Fluid Mech.*, 2020, **282**, 104311.
309 J. Tao, C. Dai, W. Kang, G. Zhao, Y. Liu, J. Fang, M. Gao and Q. You, *Energy Fuels*, 2017, **31**, 13416–13426.
310 R. Singh and K. K. Mohanty, *Fuel*, 2017, **197**, 58–69.
311 M. Wang, S. Yang, M. Li, S. Wang, P. Yu, Y. Zhang and H. Chen, *Energy Fuels*, 2021, **35**, 4296–4312.
312 M. Lv, Z. Liu, C. Ji, L. Jia and Y. Jiang, *Ind. Eng. Chem. Res.*, 2018, **57**, 15172–15180.
313 S. Jones, N. Getrouw and S. Vincent-Bonnieu, *Soft Matter*, 2018, **14**, 3490–3496.
314 B. Benali, T. L. Føyen, Z. P. Alcorn, M. Haugen, J. Gauteplass, A. R. Kovscek and M. A. Fernø, *Int. J. Greenhouse Gas Control*, 2022, **114**, 103607.
315 J. Gauteplass, K. Chaudhary, A. R. Kovscek and M. A. Fernø, *Colloids Surf., A*, 2015, **468**, 184–192.
316 D. Huh, T. Cochrane and F. Kovarik, *JPT, J. Pet. Technol.*, 1989, **41**, 872–879.
317 T. W. de Haas, B. Bao, H. Acosta Ramirez, A. Abedini and D. Sinton, *Energy Fuels*, 2021, **35**, 7866–7873.
318 G. Jian, A. Gizzatov, M. Kawelah, Z. AlYousef and A. I. Abdel-Fattah, *Appl. Energy*, 2021, **292**, 116815.
319 M. Issakhov, M. Shakeel, P. Pourafshary, S. Aidarova and A. Sharipova, *Pet. Res.*, 2022, **7**, 186–203.
320 Z. Wang, J. Sun, Y. Wang, H. Guo and S. A. Aryana, *J. Contam. Hydrol.*, 2021, **242**, 103853.
321 K. Osei-Bonsu, P. Grassia and N. Shokri, *Fuel*, 2017, **203**, 403–410.
322 Z. Xu, Z. Li, S. Cui, B. Li, D. Chen, Q. Zhang, L. Zheng and M. M. Husein, *J. Pet. Sci. Eng.*, 2022, **211**, 110170.
323 F. Guo and S. Aryana, *Fuel*, 2016, **186**, 430–442.
324 L. F. Lopes, J. M. Façanha, L. Maqueira, F. R. Ribeiro and A. Pérez-Gramatges, *J. Pet. Sci. Eng.*, 2021, **207**, 109141.
325 A. Telmadarreie, *J. Pet. Sci. Eng.*, 2017, **157**, 1170–1178.
326 Q. Gao, X. Xu, S. Liu, A. O. Mmbuji and Y. Wu, *Energy Fuels*, 2024, **38**, 3755–3768.
327 Z. Xu, B. Li, H. Zhao, L. He, Z. Liu, D. Chen, H. Yang and Z. Li, *ACS Omega*, 2020, **5**, 19092–19103.
328 A. Rahman, E. Shirif and F. Torabi, *Petroleum*, 2024, **10**, 696–704.
329 T. Lu, Z. Li and L. Du, *J. Cleaner Prod.*, 2024, **434**, 140055.
330 N. Denkov, S. Tcholakova and N. Politova-Brinkova, *Curr. Opin. Colloid Interface Sci.*, 2020, **50**, 101376.
331 N. Yekeen, M. A. Manan, A. K. Idris, E. Padmanabhan, R. Junin, A. M. Samin, A. O. Gbadamosi and I. Oguamah, *J. Pet. Sci. Eng.*, 2018, **164**, 43–74.
332 X.-C. Tang, Y.-Q. Li, Z.-Y. Liu and N. Zhang, *Pet. Sci.*, 2023, **20**, 2282–2304.
333 D. L. Weaire and S. Hutzler, *The physics of foams*, Oxford University Press, 1999.
334 B. Dollet and C. Raufaste, *C. R. Phys.*, 2014, **15**, 731–747.
335 S. Marze, R.-M. Guillermic and A. Saint-Jalmes, *Soft Matter*, 2009, **5**, 1937–1946.
336 S. Jones, N. Getrouw and S. Vincent-Bonnieu, *Soft Matter*, 2018, **14**, 3497–3503.
337 Z. AlYousef, A. Gizzatov, H. AlMatouq and G. Jian, *J. Pet. Explor. Prod. Technol.*, 2023, **13**, 1155–1162.
338 N. Nazari and A. R. Kovscek, *Lab Chip*, 2022, **22**, 3489–3498.

339 F. Friedmann and J. Jensen, SPE Western Regional Meeting, 1986, p. SPE-15087.
340 W. Yan, C. A. Miller and G. J. Hirasaki, *Colloids Surf., A*, 2006, **282**, 348–359.
341 S. Kahrobaei, S. Vincent-Bonnieu and R. Farajzadeh, *Sci. Rep.*, 2017, **282**, 348–359.
342 J. Alvarez, H. Rivas and W. Rossen, *SPE J.*, 2001, **6**, 325–333.
343 F. Guo and S. A. Aryana, *Energies*, 2019, **12**, 1390.
344 K. Chen, P. Liu, W. Wang, Y. Chen and B. Bate, *Energy Fuels*, 2023, **37**, 17263–17276.
345 W. Yang, J. W. Brownlow, D. L. Walker and J. Lu, *Water Resour. Res.*, 2021, **57**, e2020WR029522.
346 G. J. Hirasaki and J. Lawson, *Soc. Pet. Eng. J.*, 1985, **25**, 176–190.
347 A. R. Kovscek and C. J. Radke, *Fundamentals of foam transport in porous media*, Lawrence berkeley lab., ca (united states), technical report, 1993.
348 C. Zhang, M. Oostrom, T. W. Wietsma, J. W. Grate and M. G. Warner, *Energy Fuels*, 2011, **25**, 3493–3505.
349 M. J. Shojaei, K. Osei-Bonsu, P. Grassia and N. Shokri, *Ind. Eng. Chem. Res.*, 2018, **57**, 7275–7281.
350 Q. Sun, Z. Li, S. Li, L. Jiang, J. Wang and P. Wang, *Energy Fuels*, 2014, **28**, 2384–2394.
351 F. Guo, S. A. Aryana, Y. Wang, J. F. McLaughlin and K. Coddington, *Int. J. Greenhouse Gas Control*, 2019, **87**, 134–141.
352 F. Guo and S. A. Aryana, *J. Pet. Sci. Eng.*, 2018, **164**, 155–163.
353 D. Li, G. Xin and S. Ren, *ACS Omega*, 2022, **7**, 36503–36509.
354 A. Telmadarreie and J. J. Trivedi, *SPE J.*, 2016, **21**, 1655–1668.
355 M.-C. Ding, Q. Li, Y.-J. Yuan, Y.-F. Wang, N. Zhao and Y.-G. Han, *Pet. Sci.*, 2022, **19**, 1185–1197.
356 J. Casteel and N. Djabbarah, *SPE Reservoir Eng.*, 1988, **3**, 1186–1192.
357 R. F. Li, W. Yan, S. Liu, G. J. Hirasaki and C. A. Miller, *SPE J.*, 2010, **15**, 928–942.
358 M. Wang, L. Li, Y. Zhou, X. Peng, P. Yu, X. Wang and S. Yang, *Energy Fuels*, 2022, **36**, 4757–4769.
359 K. Fan, C. Guo, N. Liu, X. Liang, B. Lin and T. Liu, *Phys. Fluids*, 2025, **37**, 071301.
360 A. Muggeridge, A. Cockin, K. Webb, H. Frampton, I. Collins, T. Moulds and P. Salino, *Philos. Trans. R. Soc., A*, 2014, **372**, 20120320.
361 M. Fani, P. Pourafshary, P. Mostaghimi and N. Mosavat, *Fuel*, 2022, **315**, 123225.
362 D. Shaikhah, V. Loise, R. Angelico, M. Porto, P. Calandra, A. A. Abe, F. Testa, C. Bartucca, C. Oliviero Rossi and P. Caputo, *Molecules*, 2024, **29**, 301.
363 U. S. Behera, G. Kumar and J. S. Sangwai, *Energy Fuels*, 2022, **36**, 8115–8127.
364 D. Zhu, B. Li, L. Chen, C. Zhang, L. Zheng, W. Chen and Z. Li, *Fuel*, 2024, **362**, 130792.
365 L. P. Tuok, M. Elkady, A. Zkria, T. Yoshitake, S. A. Abdelkader, D. F. Seyam, A. El-Moneim, A. M. F. El-Bab and U. N. Eldemerdash, *Chem. Eng. J.*, 2024, **488**, 151011.
366 A. I. Pryazhnikov, M. I. Pryazhnikov, V. A. Zhigarev and A. V. Minakov, *J. Mol. Liq.*, 2025, **419**, 126773.
367 M. Saadat, P. A. Tsai, T.-H. Ho, G. Øye and M. Dudek, *ACS Omega*, 2020, **5**, 17521–17530.
368 M. Khashay, T. Ganat and E. Esmaeilnezhad, *Results Eng.*, 2025, 105380.
369 S. M. M. Bagheri, M. Nabipour, N. Esfandiari, B. Honarvar and A. Azdarpour, *J. Pet. Explor. Prod. Technol.*, 2025, **15**, 70.
370 B. Metz, O. Davidson, H. de Coninck, M. Loos and L. Meyer, IPCC Special Report on Carbon Dioxide Capture and Storage, 2005.
371 S. Bachu, D. Bonijoly, J. Bradshaw, R. Burruss, S. Holloway, N. P. Christensen and O. M. Mathiassen, *Int. J. Greenhouse Gas Control*, 2007, **1**, 430–443.
372 H. Yoon, K. N. Chojnicki and M. J. Martinez, *Environ. Sci. Technol.*, 2019, **53**, 14233–14242.
373 J. Tirapu-azpiroz, M. Esteves, A. Ferreira, R. Luis, R. Neumann, B. Ferreira, R. Giro, B. Wunsch and M. B. Steiner, *Proc. SPIE*, 2022, **11955**, 1–12.
374 J. Xu and M. T. Balhoff, *Lab Chip*, 2022, **22**, 4205–4223.
375 J. Xu, *PhD thesis*, The University of Texas at Austin, 2023.
376 O. Massarweh and A. S. Abushaikha, *Earth-Sci. Rev.*, 2024, **253**, 104793.
377 S. C. Cao, S. Dai and J. Jung, *Int. J. Greenhouse Gas Control*, 2016, **44**, 104–114.
378 R. Hu, J. Wan, Y. Kim and T. K. Tokunaga, *Water Resour. Res.*, 2017, **53**, 6377–6394.
379 Y. Song, C. Zhao, M. Chen, Y. Chi, Y. Zhang and J. Zhao, *Int. J. Greenhouse Gas Control*, 2020, **95**, 102958.
380 C. Chang, Q. Zhou, J. Guo and Q. Yu, *Int. J. Greenhouse Gas Control*, 2014, **28**, 328–342.
381 C. Chang, Q. Zhou, T. J. Kneafsey, M. Oostrom, T. W. Wietsma and Q. Yu, *Adv. Water Resour.*, 2016, **92**, 142–158.
382 C. Chang, Q. Zhou, M. Oostrom, T. J. Kneafsey and H. Mehta, *Adv. Water Resour.*, 2017, **100**, 14–25.
383 C. Chang, T. J. Kneafsey, Q. Zhou, M. Oostrom and Y. Ju, *Int. J. Greenhouse Gas Control*, 2019, **86**, 11–21.
384 N. Liu, C. Aymonier, C. Lecoutre, Y. Garrabos and S. Marre, *Chem. Phys. Lett.*, 2012, **551**, 139–143.
385 J. Yue, G. Chen, Q. Yuan, L. Luo and Y. Gonthier, *Chem. Eng. Sci.*, 2007, **62**, 2096–2108.
386 R. Sun and T. Cubaud, *Lab Chip*, 2011, **11**, 2924–2928.
387 J. Yue, E. V. Rebrov and J. C. Schouten, *Lab Chip*, 2014, **14**, 1632–1649.
388 N. Qin, J. Z. Wen, B. Chen and C. L. Ren, *Appl. Phys. Lett.*, 2018, **113**, 033703.
389 S. Yang, G. Kong, Z. Cao and Z. Wu, *Chem. Eng. J. Adv.*, 2023, **16**, 100518.
390 B. Zhao, C. W. MacMinn and R. Juanes, *Proc. Natl. Acad. Sci. U. S. A.*, 2016, **113**, 10251–10256.
391 M. Saadat, J. Yang, M. Dudek, G. Øye and P. A. Tsai, *J. Pet. Sci. Eng.*, 2021, **203**, 108647.
392 J. Yang, M. Saadat, I. Azizov, M. Dudek, G. Øye and P. A. Tsai, *Lab Chip*, 2022, **22**, 4974–4983.
393 S. Yang, H. Li, S. Suo and Z. Wu, *Adv. Water Resour.*, 2024, **191**, 104757.

394 M. Buchgraber, A. R. Kovscek and L. M. Castanier, *Transp. Porous Media*, 2012, **95**, 647–668.
395 Y. Li, G. Blois, F. Kazemifar and K. T. Christensen, *Water Resour. Res.*, 2019, **55**, 3758–3779.
396 A. A. Elryes, B. M. Negash, N. A. Md Akhir, F. Ali and R. T. Mim, *Energy Fuels*, 2024, **38**, 20196–20223.
397 Y. Li, F. Kazemifar, G. Blois and K. T. Christensen, *Water Resour. Res.*, 2017, **53**, 6178–6196.
398 P. Saffman and G. Taylor, *Proc. R. Soc. London, Ser. A*, 1958, **245**, 312–329.
399 S. Morais, N. Liu, A. Diouf, D. Bernard, C. Lecoutre, Y. Garrabos and S. Marre, *Lab Chip*, 2016, **16**, 3493–3502.
400 F. Kazemifar, G. Blois, D. C. Kyritsis and K. T. Christensen, *Adv. Water Resour.*, 2016, **95**, 352–368.
401 Y. Li, G. Blois, F. Kazemifar and K. T. Christensen, *Meas. Sci. Technol.*, 2021, **32**, 095208.
402 S. Berg, H. Ott, S. A. Klapp, A. Schwing, R. Neiteler, N. Brussee and A. Makurat, *Proc. Natl. Acad. Sci. U. S. A.*, 2013, **110**, 3755–3759.
403 M. Abolhasani, M. Singh, E. Kumacheva and A. Günther, *Lab Chip*, 2012, **12**, 1611–1618.
404 R. Miri and H. Hellevang, *Int. J. Greenhouse Gas Control*, 2016, **51**, 136–147.
405 M. Kim, A. Sell and D. Sinton, *Lab Chip*, 2013, **13**, 2508–2518.
406 R. Miri, R. van Noort, P. Aagaard and H. Hellevang, *Int. J. Greenhouse Gas Control*, 2015, **43**, 10–21.
407 D. He, P. Jiang and R. Xu, *Environ. Sci. Technol.*, 2019, **53**, 14744–14751.
408 L. Yan, R. Niftaliyev, D. Voskov and R. Farajzadeh, *J. Colloid Interface Sci.*, 2025, **678**, 419–430.
409 A. Rufai and J. Crawshaw, *ACS Earth Space Chem.*, 2018, **2**, 320–329.
410 K. M. Dąbrowski, M. Nooraiepour, M. Masoudi, M. Zając, S. Kuczyński, R. Smulski, J. Barbacki, H. Hellevang and S. Nagy, *Sci. Total Environ.*, 2025, **958**, 178110.
411 D. Zivar, S. Kumar and J. Foroozesh, *Int. J. Hydrogen Energy*, 2021, **46**, 23436–23462.
412 R. Tarkowski, *Renewable Sustainable Energy Rev.*, 2019, **105**, 86–94.
413 A. Alinejad, M. H. Molazem, A. Sharma and H. Dehghanpour, *Int. J. Hydrogen Energy*, 2024, **52**, 787–803.
414 M. Lysyy, G. Ersland and M. Fernø, *Adv. Water Resour.*, 2022, **163**, 104167.
415 M. Lysyy, N. Liu, C. M. Solstad, M. A. Fernø and G. Ersland, *Int. J. Hydrogen Energy*, 2023, **48**, 31294–31304.
416 M. Lysyy, N. Liu, D. Landa-Marbán, G. Ersland and M. Fernø, *J. Energy Storage*, 2024, **87**, 111439.
417 M. Bahrami, H. Mahani, D. Zivar and S. Ayatollahi, *J. Energy Storage*, 2024, **98**, 112959.
418 J. Gao, D. Kong, Y. Peng, Y. Zhou, Y. Liu and W. Zhu, *Energy*, 2023, **283**, 129007.
419 J. Roof, *Soc. Pet. Eng. J.*, 1970, **10**, 85–90.
420 E. M. Thaysen, I. B. Butler, A. Hassanpouryouzband, D. Freitas, F. Alvarez-Borges, S. Krevor, N. Heinemann, R. Atwood and K. Edlmann, *Int. J. Hydrogen Energy*, 2023, **48**, 3091–3106.
421 H. Song, J. Lao, L. Zhang, C. Xie and Y. Wang, *Appl. Energy*, 2023, **337**, 120901.
422 T. Lu, Z. Li and L. Du, *J. Chem. Eng.*, 2024, **481**, 148575.
423 F. E. Viveros, O. E. Medina, I. Moncayo-Riascos, M. Lysyy, P. N. Benjumea, F. B. Cortés and C. A. Franco, *J. Energy Storage*, 2024, **98**, 113110.
424 O. E. Medina, J. F. Gallego, I. Moncayo-Riascos, M. Lysyy, P. N. Benjumea, F. B. Cortés and C. A. Franco, *Int. J. Hydrogen Energy*, 2024, **60**, 959–975.
425 T. Huang, G. J. Moridis and T. A. Blasingame, *Int. J. Hydrogen Energy*, 2024, **88**, 289–312.
426 A. Lider, V. Kudiiarov, N. Kurdyumov, J. Lyu, M. Koptsev, N. Travitzky and D. Hotza, *Int. J. Hydrogen Energy*, 2023, **48**, 28390–28411.
427 W. van Rooijen, L. Hashemi, M. Boon, R. Farajzadeh and H. Hajibeygi, *Adv. Water Resour.*, 2022, **164**, 104221.
428 M. Boon, I. Buntic, K. Ahmed, N. Dopffel, C. Peters and H. Hajibeygi, *Sci. Rep.*, 2024, **14**, 8248.
429 N. Liu, A. R. Kovscek, M. A. Fernø and N. Dopffel, *Front. Energy Res.*, 2023, **11**, 1124621.
430 R. Song, M. Wu, J. Liu and C. Yang, *Energy*, 2024, **306**, 132534.
431 N. Liu, T. Skauge, D. Landa-Marbán, B. Hovland, B. Thorbjørnsen, F. A. Radu, B. F. Vik, T. Baumann and G. Bødtker, *J. Ind. Microbiol. Biotechnol.*, 2019, **46**, 855–868.
432 S. P. Gregory, M. J. Barnett, L. P. Field and A. E. Milodowski, *Microorganisms*, 2019, **7**, 53.
433 S. Dahiya, S. Chatterjee, O. Sarkar and S. V. Mohan, *Bioresour. Technol.*, 2021, **321**, 124354.
434 T. Lu, Z. Li and L. Du, *J. Cleaner Prod.*, 2024, **472**, 143494.
435 Y. Chen, X. Zhang and Z. Wu, in *Flexible Substrates*, John Wiley & Sons, Ltd, 2024, ch. 3, pp. 77–122.
436 H. Fallahi, J. Zhang, H.-P. Phan and N.-T. Nguyen, *Micromachines*, 2019, **10**, 830.
437 C. M. B. Ho, S. H. Ng, K. H. H. Li and Y. J. Yoon, *Lab Chip*, 2015, **15**, 3627–3637.
438 A. A. Yazdi, A. Popma, W. Wong, T. Nguyen, Y. Pan and J. Xu, *Microfluid. Nanofluid.*, 2016, **20**, 1–18.
439 H. Gong, A. T. Woolley and G. P. Nordin, *Lab Chip*, 2018, **18**, 639–647.
440 M. J. Männel, L. Selzer, R. Bernhardt and J. Thiele, *Adv. Mater. Technol.*, 2019, **4**, 1–10.
441 B. Carnero, Y. Radziunas-Salinas, B. K. Rodiño-Janeiro, S. V. Ballesta and M. T. Flores-Arias, *Lab Chip*, 2024, **24**, 2669–2682.
442 N. Vaisblat, N. B. Harris, K. Ayranci, R. Chalaturnyk, M. Power, C. Twemlow and N. Minion, *Mar. Pet. Geol.*, 2022, **136**, 105431.
443 K. Karimi, A. Fardoost, N. Mhatre, J. Rajan, D. Boisvert and M. Javanmard, *Micromachines*, 2024, **15**, 1274.
444 A.-I. Bunea, N. del Castillo Iniesta, A. Droumpali, A. E. Wetzel, E. Engay and R. Taboryski, *Micro*, 2021, pp. 164–180.
445 A. Nur'aini and I. Oh, *ACS Omega*, 2022, **7**, 16665–16669.

446 C. Xi, D. L. Marks, D. S. Parikh, L. Raskin and S. A. Boppart, *Proc. Natl. Acad. Sci. U. S. A.*, 2004, **101**, 7516–7521.
447 International Organization for Standardization, Microfluidic devices–Interoperability requirements for dimensions, connections and initial device classification, https://www.iso.org/standard/74157.html, ISO Standard No. 22916:2022.
448 D. R. Reyes and H. van Heeren, *J. Res. Natl. Inst. Stand. Technol.*, 2019, **124**, 1–22.
449 Royal Society of Chemistry, Chips and Tips, https://blogs.rsc.org/chipsandtips/, Accessed: 2025-07-30.
450 Texas Advanced Computing Center, Digital Porous Media Portal, https://digitalporousmedia.org/, Accessed: 2025-07-30.
451 J. E. Santos, B. Chang, A. Gigliotti, Y. Yin, W. Song, M. Prodanović, Q. Kang, N. Lubbers and H. Viswanathan, *Sci. Data*, 2022, **9**, 1–14.
452 M. Prodanović, M. Esteva, J. McClure, B. C. Chang, J. E. Santos, A. Radhakrishnan, A. Singh and H. Khan, E3S Web Conf., 2023, p. 01010.
453 J. McClure, S. Berg and R. Armstrong, *Phys. Fluids*, 2021, **33**, 083323.
454 Y. Xiao, Z. You, Y. He, Z. Du, J. Zheng and L. Wang, *Geoenergy Sci. Eng.*, 2025, **246**, 213606.
455 R. Hilfer, *Phys. Rev. E*, 2020, **102**, 053103.
456 X. Jin, C. Chao, K. Edlmann and X. Fan, *J. Hydrol.*, 2022, **606**, 127411.
457 R. Armstrong, A. Georgiadis, H. Ott, D. Klemin and S. Berg, *Geophys. Res. Lett.*, 2014, **41**, 55–60.
458 Y. Wang, R. Song, J. Liu, M. Cui and P. Ranjith, *J. Contam. Hydrol.*, 2019, **225**, 103499.
459 H. Guo, K. Song and R. Hilfer, *Transp. Porous Media*, 2022, **144**, 3–31.
460 M. Leverett, *Transactions of the AIME*, 1941, **142**, 152–169.
461 J. Kozeny, *Sitzungsberichte der Akademie der Wissenschaften in Wien*, 1927, **136**, 271.
462 P. Carman, *Transactions of the Institution of Chemical Engineers London*, 1937, **15**, 150–156.
463 A. Gringarten, D. Bourdet, P. Landel and V. Kniazeff, *SPE Annual Technical Conference and Exhibition*, September, 1979, SPE-8205-MS.
464 T. Hiller, J. Ardevol-Murison, A. Muggeridge, M. Schröter and M. Brinkmann, *SPE J.*, 2019, **24**, 200–214.
465 V. Joekar-Niasar and S. Hassanizadeh, *Crit. Rev. Environ. Sci. Technol.*, 2012, **42**, 1895–1976.
466 C. Pan, M. Hilpert and C. Miller, *Water Resour. Res.*, 2004, **40**, W01501.
467 M. Hassanizadeh and W. Gray, *Adv. Water Resour.*, 1979, **2**, 131–144.
468 M. Blunt, M. Jackson, M. Piri and P. Valvatne, *Adv. Water Resour.*, 2002, **25**, 1069–1089.
469 M. Jackson, P. Valvatne and M. Blunt, *J. Pet. Sci. Eng.*, 2003, **39**, 231–246.
470 M. Blunt, B. Bijeljic, H. Dong, O. Gharbi, S. Iglauer, P. Mostaghimi, A. Paluszny and C. Pentland, *Adv. Water Resour.*, 2013, **51**, 197–216.
471 I. Battiato, P. Ferrero V, D. O'Malley, C. Miller, P. Takhar, F. Valdes-Parada and B. Wood, *Transp. Porous Media*, 2019, **130**, 5–76.
472 O. Izgec, B. Demiral, H. Bertin and S. Akin, *Transp. Porous Media*, 2008, **72**, 1–24.
473 Q. Xie, W. Wang, Y. Su, H. Wang, Z. Zhang and W. Yan, *J. Nat. Gas Sci. Eng.*, 2023, **114**, 204978.
474 A. Gbadamosi, R. Junin, M. Manan, A. Agi and A. Yusuff, *Int. Nano Lett.*, 2019, **9**, 171–202.
475 N. A. Kamaludin, N. N. S. Suhaidi and N. Ismail, *Mater. Today*, 2023, **107**, 243–248.
476 Q. Lv, T. Zhou, Y. Luan, R. Zheng, X. Guo, X. Wang and A. Hemmati-Sarapardeh, *J. Cleaner Prod.*, 2023, **406**, 136980.
477 P. Wei, K. Guo and Y. Xie, *J. Pet. Sci. Eng.*, 2020, **195**, 107597.
478 B. N. Tackie-Otoo, M. A. A. Mohammed, N. Yekeen and B. M. Negash, *J. Pet. Sci. Eng.*, 2020, **187**, 106828.
479 R. Liontas, K. Ma, G. J. Hirasaki and S. L. Biswal, *Soft Matter*, 2013, **9**, 10971–10984.
480 A. Fatah, A. Al-Yaseri, S. Alshammari and A. S. Al-Qasim, *Energy Fuels*, 2024, **38**, 20951–20966.

